New structural and functional insights into late maturation of the large ribosomal subunit in *Escherichia coli*

Dissertation zur Erlangung des

akademischen Grades eines

Doktors der Naturwissenschaften

(Dr.rer.nat)

vorgelegt von

Schmidt, Sabine

an der

Mathematisch-Naturwissenschaftliche Sektion

Fachbereich Biologie

Konstanz, 2020

Tag der mündlichen Prüfung: 26.06.2020
1. Referentin: Prof. Dr. Elke Deuerling
2. Referent: Prof. Dr. Jörg Hartig
3. Referent: Prof. (apl.) Dr. Aswin Mangerich

Es ist was es ist.
- Unbekannt -

I. Summary

For more than six decades, the ribosome has been subject of intensive research, addressing predominantly its essential function in protein synthesis. However, considerably less is known about how ribosomes assemble from their individual components and how ribosome assembly is coordinated and facilitated by enzymatic assembly factors *in vivo*. Recent advances in both fluorescence microscopy and cryogenic electron microscopy (cryo-EM) now offer tools to address the mechanistic details of this multilayered process. This work focusses on late processes during the assembly of the large 50S subunit of *Escherichia coli* (*E. coli*) and provides a systematic, functional analysis of the late acting assembly factors DbpA, EngA, EngB, RlmE and ObgE.

An RNA-antisense-based study was employed to systematically characterize the consequences of assembly factor depletion. It was found that the absence of each of the five investigated factors caused mild to severe growth perturbation at different temperatures and an accumulation of pre-50S or 50S particles, emphasizing the central role of these five assembly factors in correct 50S maturation. Moreover, a super-resolution fluorescence microscopic technique based on 3D-SIM was established and revealed that assembly defective cells exhibit a specific morphological phenotype resulting in a considerable reorganization of ribosomal particles, reminiscent of cells treated with translation inhibitors.

This detailed phenotypic and morphological characterization was complemented by an approach utilizing engineered *E. coli* strains harboring assembly factors fused with epitope tags enabling immunodetection or purification of bona fide ribosomal precursors for subsequent structural analyses. As proof of concept, the

Summary

E. coli strain harboring StrepII-tagged GTPase ObgE was used to isolate and structurally analyze native pre-50S•ObgE-StrepII complexes by cryo-EM to elaborate ObgE´s contribution to final pre-50S assembly. The data suggest a gatekeeper function for ObgE by sensing critical conformational changes within the large subunit´s active site region that ultimately trigger GTP hydrolysis and ObgE dissociation. In addition, this study provides ten phenotypically validated strains (five knock-down and five knock-in strains, respectively) as toolbox for further structural and morphological analyses of late 50S assembly.

II. Zusammenfassung

Seit mehr als sechs Jahrzehnten ist das Ribosom Gegenstand intensiver Forschung, wobei vor allem seine essentielle Funktion bei der Proteinbiosynthese im Vordergrund steht. Vergleichsweise wenig ist allerdings über die Assemblierung des Ribosoms und die zusätzlichen enzymatischen Faktoren bekannt, die diesen Prozess *in vivo* koordinieren und erleichtern. Jüngste Entwicklungen in der Fluoreszenzmikroskopie und der Kryo-Elektronenmikroskopie (Kryo-EM) bieten nun jedoch die Möglichkeit, mechanistische Einzelheiten dieses vielschichtigen Prozesses zu untersuchen. Die vorliegende Arbeit beschäftigt sich mit der Assemblierung der großen 50S Untereinheit des Modellorganismus *Escherichia coli* und bietet eine systematische, funktionelle Analyse der spät im Prozess agierenden Assemblierungsfaktoren DbpA, EngA, EngB, RlmE and ObgE.

Hierfür wurde zunächst eine auf RNA-Antisense basierende Studie durchgeführt, um die Folgen einer Abwesenheit der verschiedenen Assemblierungsfaktoren systematisch zu untersuchen. Die Analyse zeigte, dass eine Verminderung derer zellulären Mengen sowohl bakterielle Wachstumsdefekte als auch eine Anhäufung von prä-50S- oder 50S Partikeln verursacht und verdeutlicht damit ihre zentrale Rolle während der Assemblierung der 50S Untereinheit. Darüber hinaus ergaben hochauflösende fluoreszenzmikroskopische Analysen, dass betroffene Zellen einen spezifischen morphologischen Phänotyp aufweisen, der sich in einer Umverteilung ribosomaler Partikel äußert. Ähnliche Auswirkungen wurden zuvor an Zellen beobachtet, die mit Translationsinhibitoren behandelt wurden.

Diese detaillierte phänotypische und morphologische Analyse wurde durch die strukturelle Charakterisierung von nativen ribosomalen prä-50S Partikeln ergänzt. Zu diesem Zweck wurden mithilfe chromosomaler Knock-in Techniken modifi-

zierte *E. coli* Stämme hergestellt, deren Assemblierungsfaktoren eine Epitopmarkierung tragen. Diese ermöglichen nachfolgend sowohl eine Immunodetektion der Faktoren als auch die Reinigung von nativen ribosomalen Vorläufern für Strukturanalysen. Als Konzeptnachweis wurde der *E. coli*-Stamm mit der StrepII-markierten GTPase ObgE zur Isolierung von nativen prä-50S•ObgE-Komplexen genutzt. Diese wurden anschließend mittels Kryo-EM strukturell untersucht, um die Rolle von ObgE während der Reifung der 50S Untereinheit zu verstehen. Die Daten weisen darauf hin, dass ObgE während der Reifung der 50S Untereinheit wichtige Konformationsänderungen innerhalb des funktionellen Zentrums der großen Untereinheit erfasst, die letztendlich seine GTP-Hydrolyse und somit seine Dissoziation auslösen. Entsprechend liegt eine Wächterfunktion nahe, die den korrekten Ablauf der Assemblierung kontrolliert. Darüber hinaus bietet diese Studie zehn phänotypisch validierte Stämme (fünf Knock-Down und fünf Knock-In Stämme), die als Grundlage für weitere strukturelle und morphologische Analysen der späten Assemblierung der 50S Untereinheit genutzt werden können.

Table of contents

Table of contents

Table of contents

1. Introduction

The discovery of the macromolecular particles nowadays known as ribosomes dates back to the 1940s, when Albert Claude was the first to succeed in isolating phospholipid RNA-containing granules (so-called microsomes) from the cytoplasm of animal cells[1]. During the next decade a number of laboratories described the isolation of smaller, more compact RNA-containing particles of homogenous size with sedimentation coefficients ranging from 30S (**S**vedberg[*2]) to 100S, which were defined as *ribonucleoproteins*[3]. By 1955, George E. Palade studied such particles in cells fixed *in situ* and examined them in thin sections by electron microscopy. He observed that they were highly abundant, could be found freely distributed throughout the cytoplasm and specifically attached to the ER membrane, indicating that microsomes were fragments of the ER with ribonucleoprotein particles attached[4].

In parallel, Littlefield et al. provided evidence that these particles are involved in protein synthesis[5]. Various studies of isolated ribonucleoprotein particles from yeast[6], plants[7], animals[8] and bacteria[9] followed within the next years, culminating in a symposium in 1958 where the crucial role of these ribonucleoprotein complexes in protein synthesis was discussed and their final name was determined[10]. Since then, these essential, macromolecular machineries responsible for protein synthesis are referred to as *ribosomes* and numerous laboratories contributed to the elucidation of their function, dissecting the fundamental steps of translation in-

[*] The Svedberg (**S**) unit describes the sedimentation coefficient of a particle in solution/suspension under a centrifugal field and is defined as the ratio of the speed of a substance in a centrifugal field to its acceleration in comparable units (given in 10^{-13}s). In biology, it typically refers to the rate at which particles (*e.g.* ribosomes) migrate to the bottom of a centrifuge tube under the g-force of a centrifuge.[2]

cluding initiation, elongation and termination/recycling. In parallel, extensive effort has been dedicated to the elucidation of the ribosomes' structure. Especially the advances in x-ray crystallography leveraged the breakthrough in the year 2000, when the laboratories of Ada E. Yonath[11], Thomas A. Steitz[12] and Venkatraman Ramakrishnan[13] provided first atomic-resolution structures of the large and the small bacterial ribosomal subunits. Hence, their efforts were awarded with the Nobel Prize in Chemistry in 2009[14].

1.1 The bacterial ribosome

Even though different in detail, the general design of ribosomes and their principal *modus operandi* is conserved amongst archaea, bacteria and eukarya. In each domain of life, they are composed of two unequal subunits, which universally consist of ribosomal RNA (rRNA) and ribosomal proteins (r-proteins). When Palade studied ribosomes of pancreatic cells, it became evident that they are particularly abundant in cell types that need to synthesize a substantial amount of proteins[15]. Hence, it is not surprising that ribosomes occupy as much as 40 % of total dry cell mass, corresponding to approximately 70,000 ribosomes per cell in exponentially growing *Escherichia coli* (*E. coli*) cultures[16,17].

In bacteria, the functional 70S ribosome is formed by a small 30S subunit and a large 50S subunit. The large 50S subunit harbors two rRNA molecules and 33 different r-proteins and the small 30S subunit contains one rRNA and 21 r-proteins[18].

1.1.1 Structure and function of the 50S subunit

The main function of the large ribosomal subunit is the catalysis of peptide bond formation during protein synthesis[19]. To this end, the 23S and 5S rRNA together with 33 different r-proteins form a complex 3D structure that harbors the essential

catalytic center at its core. The 23S rRNA is a major component of this center, as the catalytic properties reside within one of its distinct domains[20].

The traditional depiction[21] of the secondary structure of the 23S rRNA shows a subdivision into six different domains[22,23] (**Figure 1**).

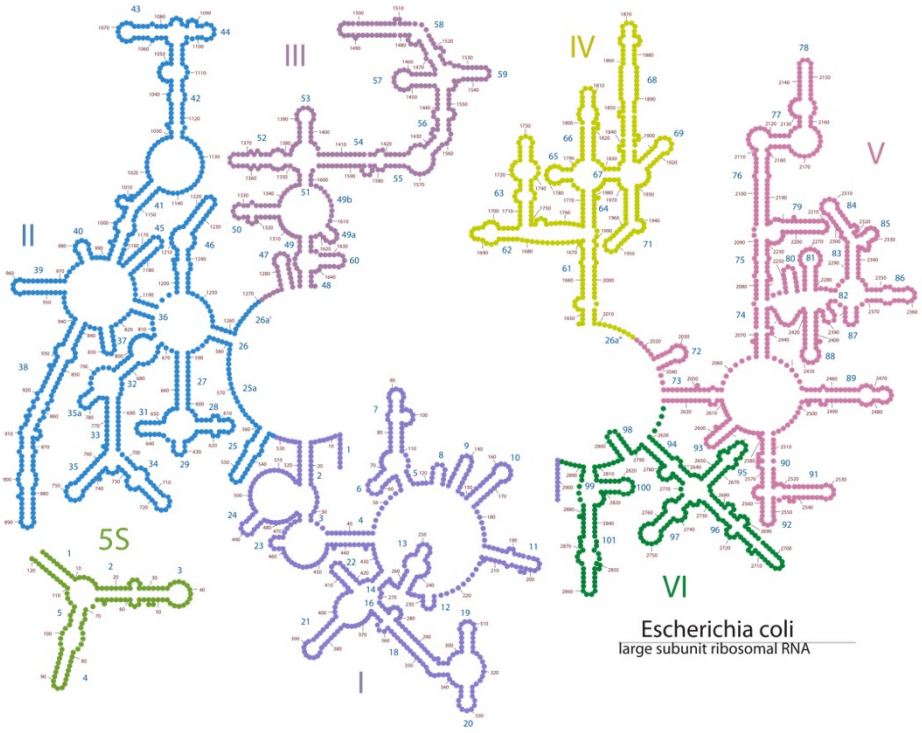

Figure 1: Traditional presentation of *E. coli* 23S and 5S rRNA secondary structure. Figure republished with minor changes by permission from Oxford University Press - Journals, from Petrov et al., 2013[24]. doi: 10.1093/nar/gkt513., permission conveyed through Copyright Clearance Center, Inc.

Recent advances in cryogenic electron microscopy (cryo-EM), especially the use of direct-electron detectors (DED) and single-particle methods in combination with *in silico* sorting of particles (**1.4**) allows near-atomic resolution of macromolecular complexes. This data complements secondary structure modeling and is nowadays the predominant method to analyze the tertiary structure of ribosomes[25].

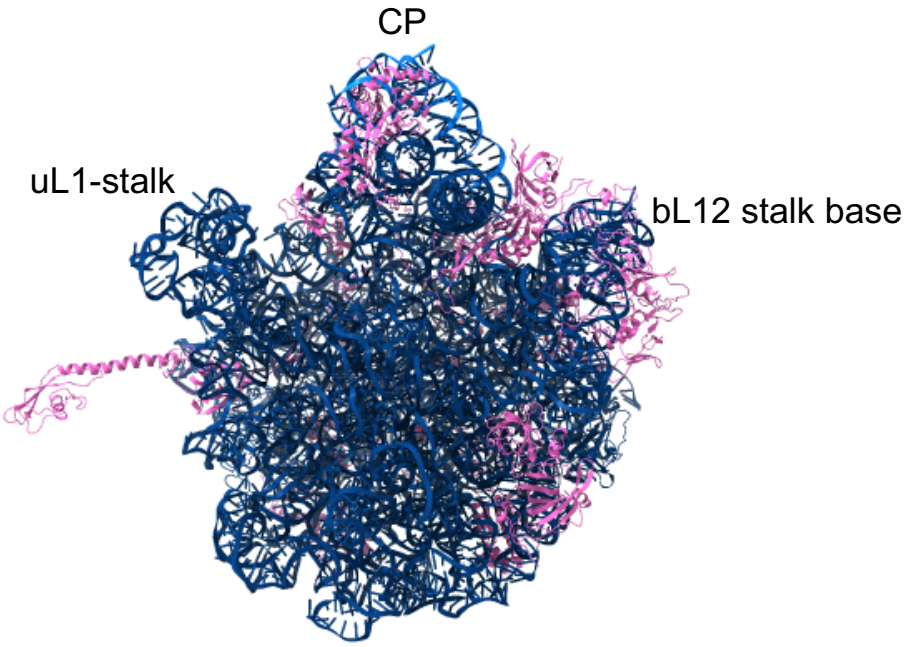

Figure 2: 3D structure of the 50S subunit. 23S rRNA (dark blue) and 5S rRNA (light blue). Ribosomal proteins are depicted as pink colored ribbons. CP (central protuberance), uL1-stalk and bL12-stalk base are indicated. The figure is based on PDB file 4V9D and was generated with UCSF ChimeraX.

The 3D structure of the 50S subunit resembles a hemisphere with three prominent features extending beyond its surface[26,27] (**Figure 2**). One of them is the central protuberance (CP), which is mainly formed by the 5S rRNA and nine ribosomal proteins (uL5, uL16, uL18, bL25, bL27, uL30, bL31, bL33 and bL35)[28,29]. The uL1 stalk and the bL12 stalk form the other two protrusions and remind of two arms extending beyond the body on both sides when viewed from the subunit (SU) interface[30,31].

Due to their conformational flexibility the stalks are difficult or even impossible to resolve by x-ray crystallography or cryo-EM, but analyses like single-molecule FRET or solution-state NMR spectroscopy allow to follow their real-time dynamics[32-34]. The uL1 stalk is composed of the uL1 protein and helices 76, 77 and 78 of

domain V of the 23S rRNA[35] and it has been shown to modulate tRNA translocation and dissociation[33,36-39]. The bL12-stalk consists of protein uL10 and multiple copies of bL12 and serves as an interaction platform for translational GTPases (trGTPases)[40-42].

Further important functional sites of the 50S subunit include the peptidyl transferase center (PTC) and the whole functional core, the GTPase-associated center (GAC), the sarcin-ricin-loop (SRL) and the polypeptide exit tunnel. The PTC is presumably the most important functional area of the 50S subunit, as it is the site of peptide bond formation and peptide release[43-45]. In *E. coli*, it is formed by parts of domain V of the 23S rRNA[46]. In a strict sense, the term PTC essentially only refers to the central loop of domain V that harbors all catalytically relevant rRNA residues (**Figure 3**).

Although several proteins interact with domain V, the catalytic center is comprised exclusively of rRNA[12,47,48]. Thus, the ribosome is also referred to as ribozyme[49].

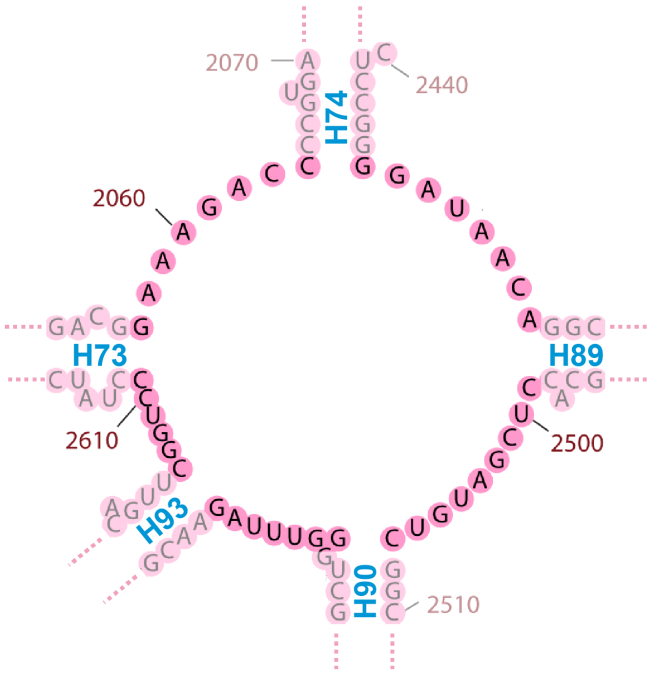

Figure 3: 2D diagram of the 23S RNA at the PTC. Central loop of domain V within the 23S rRNA is depicted. Positions of helices originating from the central loop are indicated.

Figure republished with minor changes by permission from Oxford University Press - Journals, from Petrov et al., 2013[24]. doi: 10.1093/nar/gkt513., permission conveyed through Copyright Clearance Center, Inc.

The rRNA helices directly protruding from the central loop (H73, H74, H89, H90-92, H93) and more distant ones (H42-44, H95), constitute an interacting network in the 3D-structure. This whole region in addition includes the r-proteins uL6, uL16 and bL36 and has been referred to as functional core[50] (**Figure 4**).

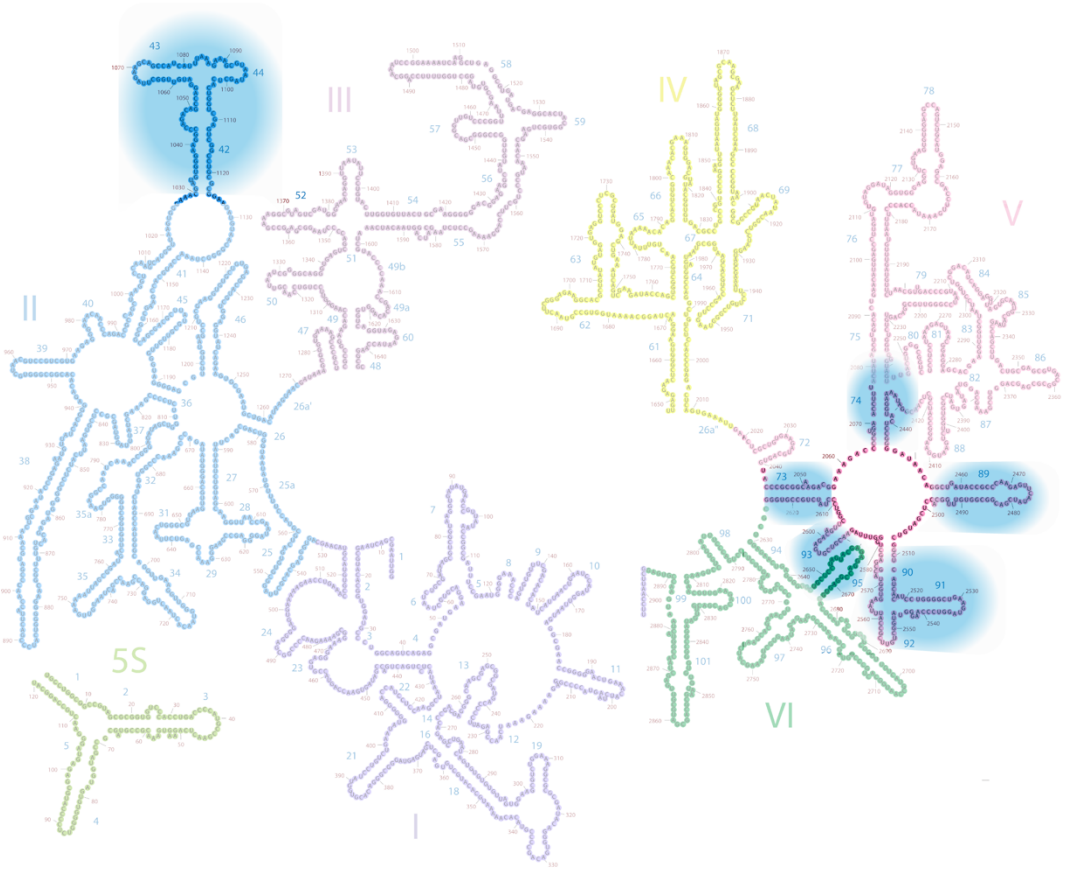

Figure 4: Functional core interaction sites of the 23S rRNA. *E. coli* 23S and 5S rRNA secondary structures are shown. Helices interacting with the functional core are highlighted in light blue. Figure republished with minor changes by permission from Oxford University Press - Journals, from Petrov et al., 2013[24]. doi: 10.1093/nar/gkt513., permission conveyed through Copyright Clearance Center, Inc.

As the binding site for trGTPases, the GTPase-associated center is involved in GTPase-related events and includes helices 42-44 of the 23S rRNA, as well as protein uL11, uL10 and at least one bL12 protein[51,52]. The sarcin-ricin-loop (SRL) is the second site for elongation factor (EF) binding and is located within domain VI of the 23S rRNA[50,52].

The polypeptide exit tunnel is located near the PTC and, with a length of 100 Å and a diameter of 25 Å, spans the whole subunit[12]. It is formed by domains I to V of the 23S rRNA and the tunnel-lining proteins uL4 and uL22, which form a constriction[49]. Rather than being a passive element of the 50S subunit, it was shown to participate in co-translational protein folding[53-57], regulation of elongation[57,58], stalling[53], discrimination against certain sequences[59] and the binding of antimicrobial agents[11,57,60,61].

1.1.2 Structure and function of the 30S subunit

Although significantly smaller than the large ribosomal subunit (~1.45 MDa), the 30S subunit is a macromolecular complex of a considerable size of 0.85 MDa[11], comprising one rRNA (16S rRNA) and 21 r-proteins (S1-21).

During the 1980s, the first secondary structure models of the 16S rRNA from *E. coli* were established[62-64]. According to these, the secondary structure is subdivided into four domains, including the 5‘ domain, the central domain, the 3‘ domain and the 3‘ minor domain (**Figure 5**). In contrast to the secondary structures of the 23S rRNA, these elements reflect the 3D structure of the subunit almost perfectly.

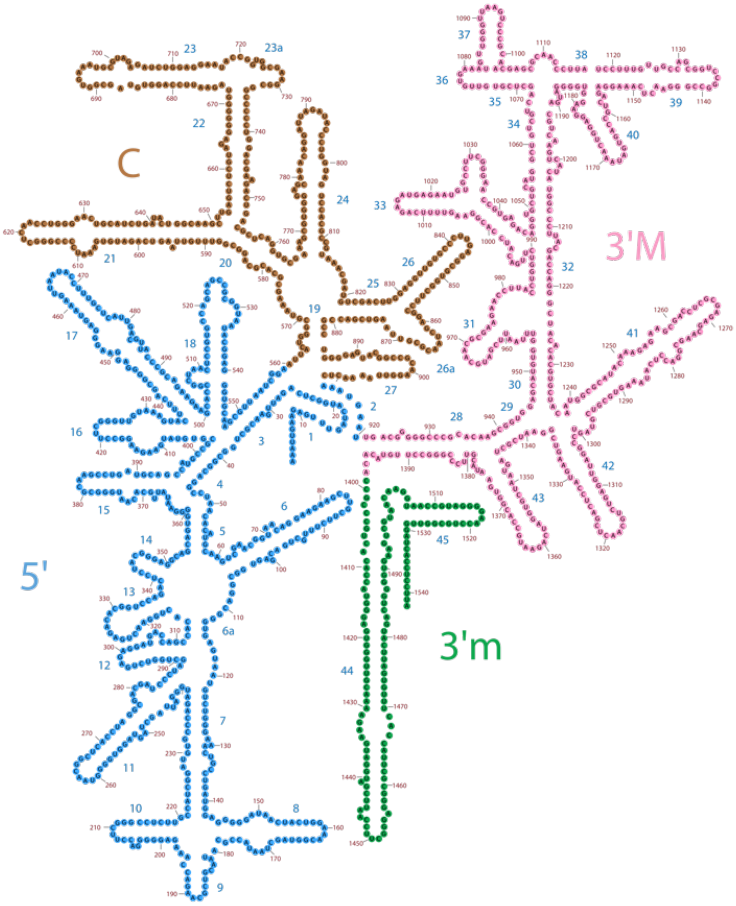

Figure 5: *E. coli* 16S rRNA secondary structure. The secondary structure comprises 4 domains: central domain (C; dark yellow), 5′ domain (5′; blue), 3′ domain (3′M, pink) and 3′ minor domain (3′m; green). This figure is licensed under CC BY 3.0.

The tertiary structure of the small subunit forms a body (5′ domain) with a platform (central region of the 16S rRNA), a head region (3′ end of the 16S rRNA) and the interface, which is defined by the 3′ minor domain that runs along the body (**Figure 6)**.[13,65]

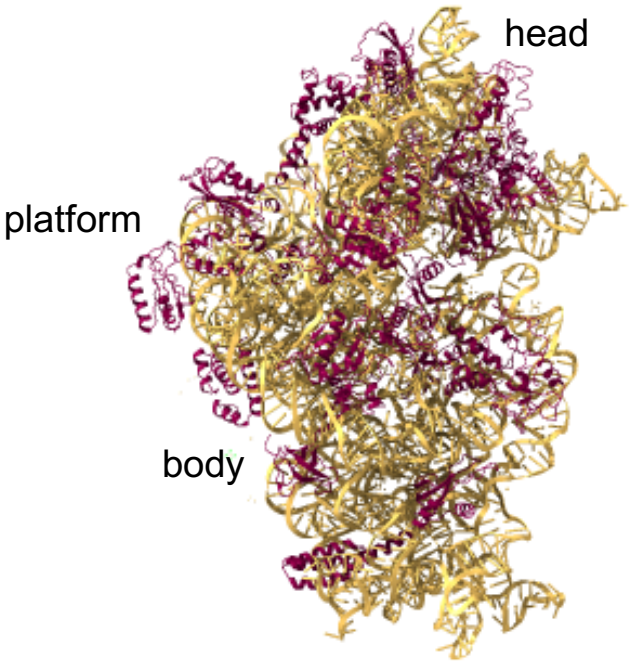

Figure 6: Tertiary structure of the 30S subunit. The small 30S subunit is composed of the 16S rRNA, indicated in yellow and ribosomal proteins that are represented as red colored ribbons. Body, platform and head region are indicated. The figure is based on PDB file 4V9D and was generated with UCSF ChimeraX.

During translation, the 30S subunit likewise contributes to the completion of specific processes, including mRNA association and decoding, as well as modulating mRNA and tRNA translocation[66]. Generally, it contributes significantly to translation fidelity by controlling codon-anticodon interactions[67]. These interactions are mainly regulated by the anti-Shine-Dalgarno sequence, which is located at the 3‘ end of the 16S rRNA[68]. This region pairs with the corresponding Shine-Dalgarno sequence on the mRNA and thereby facilitates the correct positioning of the 30S P-site at the start codon of the transcript[69-71]. However, not only the 16S rRNA, but also various ribosomal proteins of the small subunit are reported to participate in the processes mentioned above, as for example uS12, which is involved in decoding[72], uS3, uS4 and uS5, which form the mRNA entry pore and are assumed to exert

helicase activity on the mRNA during translation[73] or uS12 and uS13, which mediate translocation of the mRNA/tRNA complex[74].

1.2 Ribosome assembly

1.2.1 Key steps and spatial organization of ribosome assembly

The terms ribosome assembly or ribosome biogenesis both refer to all of the numerous processes that lead the formation of functional subunits. Independent of the organism, they include the synthesis of pre-ribosomal rRNA (pre-rRNA) and r-proteins, rRNA processing, modification and folding, r-protein modification and their association with the respective rRNA strands. Due to the complexity of this series of events, ribosome assembly is facilitated by so-called ribosome biogenesis or assembly factors that coordinate and mediate distinct steps during assembly (**Figure 7**).[16,75]

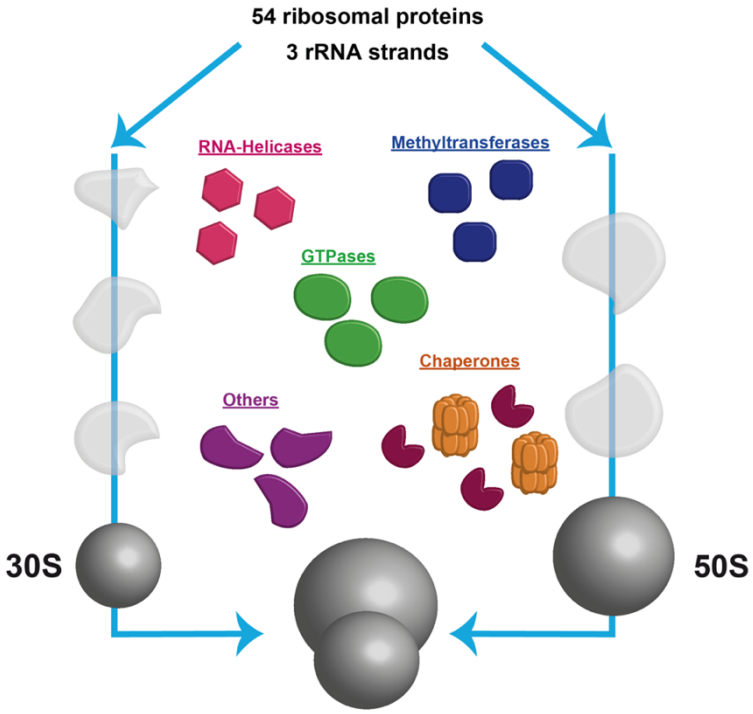

Figure 7: Scheme of bacterial ribosome assembly. Subunits are assembled from 54 ribosomal proteins and precursor rRNA containing 5S, 23S and 16s rRNA. Various different assembly factors (RNA-Helicases, methyltransferases etc.) assist the assembly pathway.

In eukaryotes, this process is not only temporally, but also spatially organized. While pre-rRNA synthesis, processing and first folding steps occur explicitly in the nucleolus (with exception of the 5S rRNA, which is transcribed in the nucleoplasm), r-protein association only happens in the nucleoplasm and later in the cytoplasm[76-78]. Thus, not only processing, modification and folding, but also the transport of pre-ribosomal particles from the nucleolus through the nucleoplasm and across nuclear pore complexes into the cytoplasm has to be coordinated precisely.

Although bacteria don't exhibit such specific subcellular compartmentalization via intracellular organelles, ribosome assembly and translation were found to be spatially organized. In prokaryotic cells such as *E. coli*, the so-called nucleoid region qualifies as the equivalent to the eukaryotic nucleolus[79]. The nucleoid describes the location of the bacterial chromosome within the cell and is usually found at the cell center in mono-nucleoid cells. Super-resolution microscopic techniques, electron cryotomography, as well as kinetic modeling indicate that 70S ribosomes mostly localize to the cell poles where they engage in translation[79-81]. Only approximately 10-15 % are found within the nucleoid region and in general, these studies indicate strong ribosome-nucleoid segregation[82,83]. The 10-15 % of particles are thus hypothesized to represent mainly free ribosomal subunits or 70S ribosomes which engage in co-transcriptional translation or subunit precursors that are being assembled[84].

1.2.2 Post-transcriptional processing and modification of rRNA and r-proteins

In bacteria, rRNA is encoded within operons (gene clusters) and is thus synthesized as a single polycistronic precursor[85,86]. In *E. coli* there are seven *rrn* operons (*rrnA-H*)[87], encoding a single copy of the 5S, 16S and 23S rRNA, respectively and one or more tRNAs in the spacer regions and the 3' proximal region[85].

As the pre-rRNA is being transcribed, formation of local secondary structures, binding of ribosomal proteins, chemical modification and processing already run in parallel[88]. Processing is completed by various RNases, starting with processing by RNase III. In normal growing *E. coli*, the earliest rRNA precursor that can be isolated is a 27S rRNA[89].

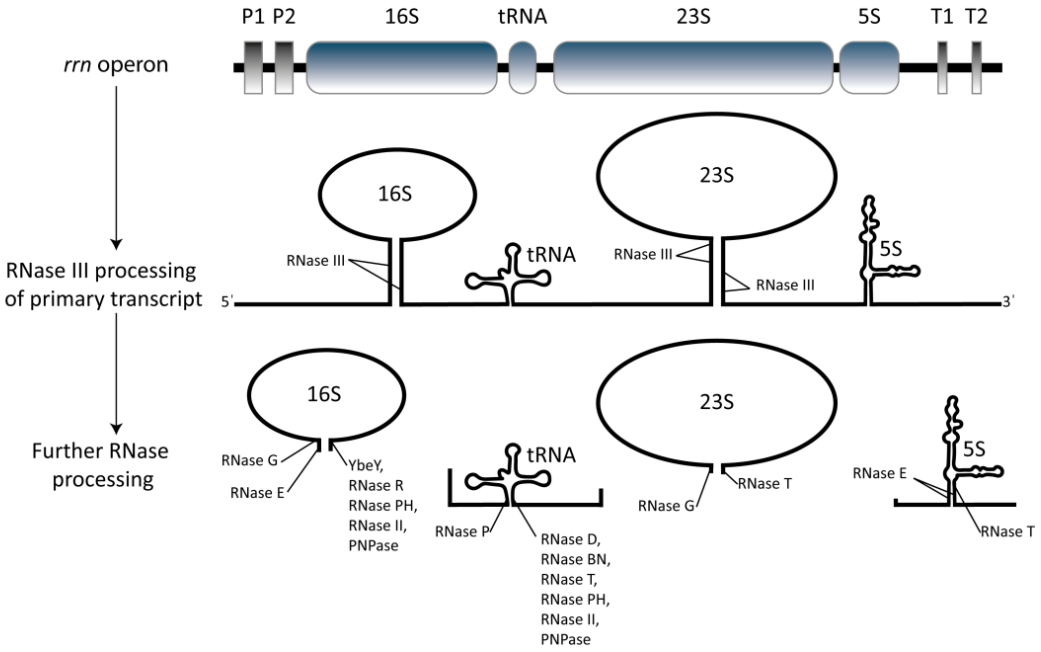

Figure 8: Schematic overview of rRNA processing in *E. coli*. The polycistronic primary transcript encoding 16S, 23S and 5S rRNA, as well as one or more tRNA's is processed into the pre-16S (17S), pre-23S (25S), pre-tRNA and pre-5S by RNase III. Cleavage sites are recognized by formation of helical stem loops. Final rRNA and tRNA processing is carried out by a range of ribonucleases as indicated. This figure was adapted from Bennison et al., 2019[90] and is licensed under CC BY 4.0.

Processing of this large precursor transcript is facilitated by the formation of local hairpin structures comprising 16S and 23S rRNA sequences, whose double-helical stems are recognized and cleaved by RNase III[91-93], yielding the 25S, 17S and 9S rRNA and tRNA precursors (**Figure 8**). 25S rRNA processing further includes the activity of RNase III for trimming of both ends[91,94] and exonuclease RNase T at the

3‘ end[95]. Final processing of the 5‘ end is completed by a yet unknown endonuclease[96]. Maturation of 16S rRNA on the other hand does not depend on RNase III, but additional RNases, including RNase E[97,98] and RNase G[98], which were shown to be involved in the maturation of the 5‘ end. It is furthermore hypothesized that the highly conserved endonuclease YbeY[99], as well as RNase II, RNase R, PNPase and RNase PH might be the involved in the final maturation of the 3‘ end[99,100]. After removal of the tRNA sequences by RNase P, the 9S precursor is generated and afterwards processed by RNase E at both ends[97,101]. Thereafter, RNase T completes final trimming at the 3‘ end[102]. Again, another unknown RNase is involved in the final processing of the 5‘ end[103]. Completion of these steps finally yields in the formation of 23S, 5S and 16S rRNA sequences (**Figure 8**).

Apart from the complex processing events, rRNA additionally undergoes various post-transcriptional modifications, which take place at a single nucleotide level. They include methylation of bases, ribose methylation and pseudouridinylation. A comprehensive overview of all known modifications of the 16S and 23S rRNA can be found in the RNA modification database hosted by The RNA Institute, with the initial version being published in 1994 by Limbach and colleagues[104]. According to current understanding, the 16S and 23S rRNA in *E. coli* are modified at 11 and 25 residues, respectively[22,104-108]. The 5S rRNA, like most 5 and 5.8S rRNAs remains unmodified. Most of the modifications are found within functional centers, like the PTC or the decoding center or on highly conserved nucleotides[105,109]. In general, most of these modifications were found to be important for modulating interactions with binding partners, for ribosome assembly or can contribute to translation and translation fidelity[67,110,111].

The single-copy genes encoding ribosomal proteins are equally organized in operons, which in many cases also include genes encoding non-ribosomal proteins. These additional genes encode for translation factors (EF-Ts, EF-G or EF-Tu), RNA

polymerase subunits, components of the replication complex (DNA primase or primosomal replication protein N), tRNA and rRNA modifying and processing enzymes (RNase P or ribosome maturation factor rimM), membrane proteins (YhbE) and others[112]. After translation, they similarly undergo various chemical modifications, including methylation (uS11[113], uL3[114,115], uL11, bL12[116], uL16[117] and bL33[118]), acetylation (uS5[119], bS18[120] and bL12[121,122]), methylthiolation (uS12[123]) and even the addition (bS6[124]) or partial removal of amino acid residues (bL31[125]).
As protein synthesis is initiated by formylmethionine in prokaryotes[126], removal of this residue is the most common post-translational modification[127]. After deformylation, the N-terminal methionine is processed by the only methionine aminopeptidase MAP (MAP1)[128].

Again, these modifications in general modulate protein-protein or protein-RNA interactions and can thus affect translation and ribosome assembly. Moreover, several ribosomal proteins were reported to fulfil extra-ribosomal functions, *e.g.* acting as autogenous regulators by controlling the expression of their own operon[129].

1.2.3 Ribosome assembly *in vitro and in vivo*

In the 1960s and 1970s, detailed insight into the assembly process was provided by *in vitro* reconstitution experiments of both 30S and 50S subunits from purified components. Traub and Nomura[130] were the first to accomplish the reconstitution of functional small subunits using natural 16S rRNA and a mixture of r-proteins extracted from purified 30S subunits (CP30). During the following years, several laboratories repeated these reconstitution experiments with individually purified[131] or recombinant r-proteins[132] and likewise achieved the *in vitro* reconstitution.

These first studies revealed that the binding of ribosomal proteins follows a strict order, in which the association of primary proteins (directly binding to rRNA strands) is indispensable for the integration of the following secondary and tertiary

proteins. Based on this hierarchic association, *in vitro* ribosome assembly maps[130,133,134] were generated, depicting the exact order and dependencies of protein binding (**Figure 9,** left). This was the first time that the events during assembly were given a specific timeline, allowing a separation into early and late stages.

In 1982, Röhl and Nierhaus[133] and Herold and Nierhaus[134] succeeded in reconstituting fully functional 50S subunits and established a corresponding map for the large ribosomal subunit (**Figure 9,** right).

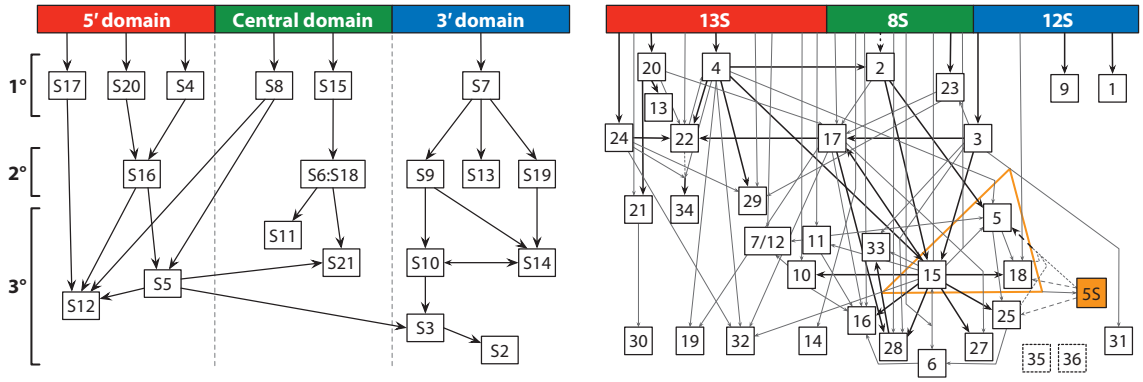

Figure 9: *In vitro* assembly maps of the 30S and 50S subunit. (A) The 16S rRNA with its 3 general domains: 5' domain: red, central domain: green, 3' domain: blue. The 23S rRNA is divided into its main fragments. 5S rRNA is depicted in orange. Ribosomal proteins are categorized as primary (1°), secondary (2°) or tertiary (3°) proteins, according to their binding order. Dashed lines emphasize the binding region of the ribosomal proteins. Arrows indicate binding dependencies. The orange triangle encloses proteins that are essential for integration of 5S rRNA. Figure republished by permission from Annual Review of Biochemistry, from Shajani et al., 2011. doi: 10.1146/annurev-biochem-062608-160432., permission conveyed through Copyright Clearance Center, Inc.

Hence, today, *in vitro* assembly is comparatively well understood and it builds the basis for the elucidation of how assembly proceeds *in vivo*. Yet, the differences in efficiency and time-kinetics between *in vitro* and *in vivo* production of ribosomes are immense (assembly is >10 times faster in cells[135,136]) and also the conditions dif-

fer greatly. While *in vitro* assembly depends on harsh, non-physiological conditions like high salt concentrations and high temperatures and still requires hours to be accomplished (**Figure 10**), the assembly of a functional ribosome *in vivo* happens within about just 2 minutes in wild-type bacteria at 37 °C[135].

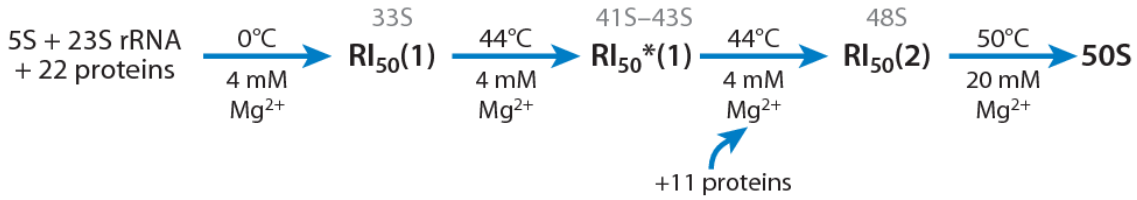

Figure 10: *In vitro* reconstitution protocol. Steps of conventional *in vitro* reconstitution for the 50S subunit. RI = ribosomal intermediates. Asterisks denote species that differ from previous species by conformational change. Figure republished by permission from Annual Review of Biochemistry, from Shajani et al., 2011. doi: 10.1146/annurev-biochem-062608-160432., permission conveyed through Copyright Clearance Center, Inc.

Thus, it is indispensable to investigate how subunit formation actually proceeds in the living organism. However, the high efficiency of assembly *in vivo* inevitably results in an extremely low abundance of available ribosomal intermediates (less than 5 % of total ribosomes[137]) that could provide such information. Thus, current knowledge of *in vivo* assembly has been mainly obtained by the analyses of precursor particles accumulating in mutant strains or cells treated with ribosome-targeting antibiotics[138-142]. There is one study describing the analyses of native, low-abundant intermediates by pulse-chase and quantitative mass spectrometry (qMS)[143], but overall, information on precursors as they are built in unperturbed strains is scarce[75,135,143].

The limited information that is available indicates that *in vitro* binding dependencies match well with the *in vivo* data, but nevertheless, they do not fully correspond[75,135,143]. Recent studies suggest that assembly *in vivo* even proceeds via multiple pathways running in parallel, giving rise to the formation of precursor

particles with similar sedimentation coefficients, but with differences in protein composition[142,144].

Especially very little is known about how 50S formation proceeds *in vivo*. This is not surprising, as a comparison of the two *in vitro* assembly maps already indicates that the assembly of the large ribosomal subunit is much more complex (more components and even more complex binding dependencies). Due to this complexity, particularly the large subunit relies greatly on the assistance by additional factors. *In vivo* assembly in general is facilitated by these so-called biogenesis or assembly factors, which significantly support and accelerate 30S and 50S formation[145].

1.2.4 Assembly factors

Overall, assembly factors represent a diverse set of proteins that facilitate the maturation of ribosomal subunits. They include the rRNA processing, as well as rRNA and r-protein modifying enzymes mentioned above, but also RNA helicases, GTPases, chaperones and various others[75,146]. While more than 200 assembly factors have been proven to be involved in ribosome assembly in yeast *Saccharomyces cerevisiae* and even more in mammalian ribosome assembly, comparatively few have been identified in bacteria [147-149]. Indeed, evidence suggests that there are a lot more factors, which have to be identified yet. Moreover, in many cases, details concerning their mechanisms of action and especially the time point of their involvement are largely unknown. Since also many of the factors are proposed to have multiple cellular functions, it is even more difficult to identify their role in correct ribosome assembly[150]. Yet, they are known to assist numerous steps from early to late stages and are generally thought to help avoiding and subverting kinetic traps *in vivo*, which are, at least partially, overcome by thermal energy *in vitro*[75,144,145,151-153].

1.2.4.1 Assembly factors assisting late 50S maturation

Recently, particular interest has been directed towards assembly factors that assist the maturation of functional centers and especially the PTC in eukaryotes[154,155], as it forms one of the most critical areas of the ribosome. However, a thorough understanding of how the PTC and other functional regions are assembled in prokaryotes and which factors are involved, is still missing. Several analyses, however, revealed that they form very late during *in vitro*[156] and *in vivo*[157-160] assembly. Nevertheless, the exact mechanisms remain unclear.

A small subset of assembly factors is supposed to be involved in the maturation of the PTC in prokaryotes and although neither their concrete functions nor their mechanisms of action have been elucidated, a direct contribution of these factors to the maturation of the PTC and adjacent RNA moieties is highly probable[161-169]. This small subset includes the RNA helicase DbpA, the GTPases EngA, EngB, ObgE, and the methyltransferase RlmE.

1.2.4.1.1 DEAD-box helicase DbpA

RNA molecules are known to easily form non-native, but very stable competing secondary structures and the rearrangement between these states was found to happen very slowly at physiological temperatures[170-172]. The formation of kinetically trapped non-native rRNA structures is thought to at least partially account for the slow assembly process *in vitro*, while such misfolding is assumed to prevented or limited and proper folding is supported by RNA modulating factors *in vivo*[75,151,173-175]. DbpA is one of four RNA helicases, which are proposed to fulfill such functions during ribosome assembly in *E. coli*.

All of these four RNA helicases belong to the DEAD-box family, which is involved in numerous cellular processes, including transcription, pre-mRNA splicing, RNA-decay, RNA transport, translation initiation and several others[176,177].

DEAD-box proteins contain nine amino acid motifs within a core domain (**Figure 11**) that are highly conserved from bacteria to humans[178,179]. While three of the motifs, namely motif I and II (Walker motif A and B) and the Q-motif, are involved in ATP binding and hydrolysis, motifs Ia, Ib, III, IV and V are most likely involved in RNA binding or are required for intermolecular rearrangements necessary for remodeling activity[180]. The flanking C- and N-terminal extensions are variable and thought to account for substrate specificity.

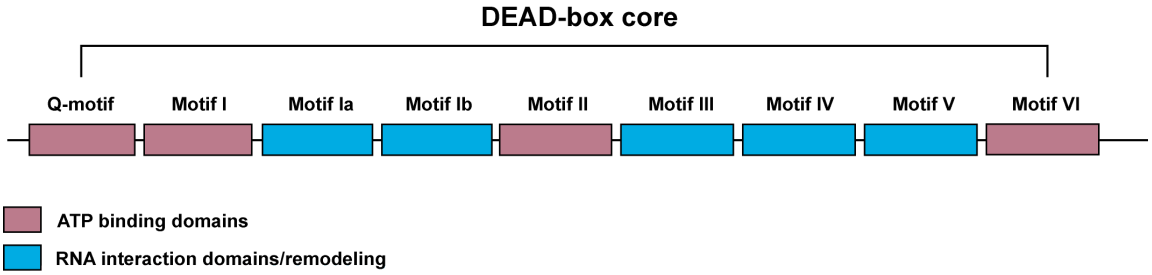

Figure 11: The conserved motifs of DEAD-box proteins. Schematic presentation of the conserved motifs in DEAD-box core. Additionally, DEAD-box proteins contain a non-conserved amino-terminal domain and carboxyl-terminal domains of variable length.

However, such sequence specificity has only been demonstrated for DbpA, which requires hairpin 92 of the 23S rRNA (located within the functional core) for ATPase and helicase activity *in vitro*[181-185]. The specific targets of the other three RNA helicases involved in assembly (CsdA, RhlE and SrmB) are still unknown.

Although DbpA was shown to be non-essential under various conditions, overexpression of the active side mutant R331A (impaired in ATPase and helicase activity) was found to cause a slow growth phenotype and an accumulation of 45S particles containing immature 23S rRNA and lacking a subset of late ribosomal proteins[164,166,186-188]. In contrast to fully mature 50S subunits or 70S ribosomes, however, these precursors were found to stimulate the ATPase of DbpA. The assumption is, that the binding site of DbpA is only accessible during 50S maturation, while it is buried in completely maturated particles.[12,189,190]

Taken together, these observations indicate that DbpA acts as a ribosome assembly factor during the late maturation of pre-50S particles in the region of the PTC.

1.2.4.1.2 GTPases ObgE, EngB and EngA

A number of GTPases also contribute to correct RNA folding and at least seven of them are known to be involved in prokaryotic ribosome assembly[90,146,191]. All of those seven GTPases belong to the TRAFAC (*translation factor-related*) class within the P-loop GTPases, which are typically involved in translation, signal transduction, cell motility and intracellular transport[192]. In general, they are characterized by a highly conserved GTPase domain, that consists of four to five motifs (**Figure 12**).

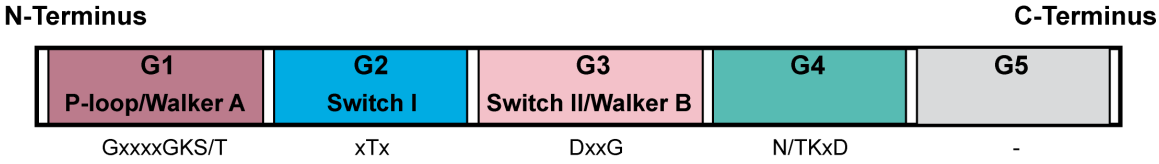

Figure 12: Domain-structure of GTPase domain. The general domain structure of the highly conserved GTPase domain is shown. Consensus sequences are indicated.

The P-loop GTPases are named according to a conserved sequence motif, the "P-loop" (phosphate-binding loop). The P-loop is also known as Walker A motif and contributes to phosphate binding in many ATP or GTP utilizing proteins by binding and recognizing the α- or β-phosphate. It is a glycin-rich loop with the consensus sequence GxxxxGK(T/S)[193-195]. Apart from the Walker A motif, the highly conserved GTPase-domain (G-domain) consists of the G2 and G3 motifs, also known as switch I and switch II, respectively, which mediate hydrolysis of GTP to GDP[196]. As their name suggests, these two motifs are central to the switching mechanism that allows GTPases in general to "switch" a signal transduction chain on and off or in particular to regulate distinct maturation steps during assembly[191]. The G4 motif comprises four hydrophobic amino acids followed by (N/T)(K/Q)XD and confers the specificity towards guanine rings while discriminating against ATP[197].

The G5 motif is not universally conserved among the TRAFAC GTPases, but it was shown to interact with the guanine base via hydrogen bonds[191].

In contrast to the RNA helicases involved in assembly, most of the GTPases are essential in *E. coli* and mutants of these all lead to reduced levels of 70S ribosomes[146]. While their precise functions during assembly are still unknown, they are hypothesized to participate in the following processes:

- mediate the recruitment and binding of r-proteins and other assembly factors[146]
- act as a checkpoint of accurate assembly by preventing progression of the process (further r-protein binding etc.) until correct formation of a GTPase binding site[146,191]
- control the rate of ribosome production by direct sensing of GTP levels under stress conditions[90,146,191]

The three GTPases that are thought to assist the maturation of the PTC are ObgE (CgtA or YhbZ), EngA (YphC, YfgK or Der) and EngB (YsxC or YihA).

ObgE is conserved from bacteria to humans and although it has been the subject of numerous studies, its main function in the cell is still under debate. It is linked to various cellular processes, like chromosome segregation[198,199], stress activation[200], persistence[201], cell division[198,202], sporulation[203,204] or the stringent response[200,205]. However, several studies also clearly demonstrate a fundamental role of ObgE during the assembly process of the large ribosomal subunit[206-210].

Co-migration with free 50S or 30S subunits has been observed in *Caulobacter crescentus*[211] and *E. coli*[161,207] and the yeast homolog Nog1 was found to be required for 60S assembly[212]. Strong evidence was moreover demonstrated by Jiang et al.[208] who extensively studied the phenotype of strains expressing a temperature-sensitive

mutant of the ObgE protein in *E. coli*. They found that these cells are impaired in ribosome assembly and accumulate free ribosomal subunits as well as 50S particles that harbor reduced amounts of late assembly proteins uL16, bL33 and bL34. Furthermore, a structure of recombinant ObgE in the presence of GMP-PNP bound to purified 50S subunits published by Feng et al.[169] demonstrated that ObgE binds to the intersubunit face of the 50S subunit in the area of the GTPase-associated center with its N-terminal domain protruding into the PTC.

EngB is a typical TRAFAC GTPase, containing one G-domain, as well as an extra β-strand at the N-terminus. It is essential in *E. coli*[213], *B. subtilis*[214,215] and *S. aureus*[216], and its depletion in *B. subtilis* causes an accumulation of 50S precursors migrating at 44.5S, lacking proteins uL16, bL27 and bL36[162]. Cryo-EM analyses of particles isolated from EngB depleted cells in *B. subtilis* furthermore revealed that especially the central protuberance, the GTPase-associated center and key RNA helices within the A- P- and E-site exhibited an immature conformation. Thus, EngB similarly seems to be involved in the maturation of functionally important areas of the 50S subunit[159]. Morphologically, its depletion leads to cell elongation in *E. coli* and *B. subtilis*[213,214].

The same abnormal morphology was observed in **EngA** depleted cells[214,217]. In contrast to the other GTPases involved in 50S assembly, the EngA protein contains two consecutive G-domains at the N-terminus, which are connected by an acidic linker, followed by a C-terminal KH-domain[218,219]. In general, it is highly conserved in gram-positive and gram-negative bacteria and accordingly, it was shown to be essential in *E. coli* and *B. subtilis* and various other bacterial species[214,217,220,221]. Due to its interaction with 70S ribosomes and ribosomal subunits *in vitro*[222], co-purification with ribosomal proteins[223,224], co-fractionation with 50S subunits and 70S ribosomes[217,222,223] and the accumulation of 30S and 50S subunits or precursors and a decrease of 70S ribosome levels in cells depleted of EngA[217,225], it was proposed to

be involved in ribosome assembly. Structural analyses by Zhang et al.[167] described that recombinant EngA associates with purified 50S subunits at the PTC and thereby induces conformational changes that result in the formation of an immature state, reversing maturation.

Similar to the precursors found in EngB depleted cells, precursors found in cells depleted of EngA migrate at 45S, lack late assembly proteins uL16, bL27 and bL36 and exhibit a non-native conformation of the of the CP, the GTPase-associated center and the functional core in *B. subtilis*[159]. Particles accumulating in *E. coli* are presumably different, as they were shown to migrate at 50S, exhibit a higher sensitivity to reduced Mg^{2+} concentration in comparison to wild-type 50S and show a decreased occupancy of bL9 and uL18[226].

Although numerous assembly factors have been discovered over the last few decades and although there is a lot of information on how these potentially contribute to a specific step, the course of the assembly pathway as a whole and the spatial dynamics of assembly in prokaryotes remain unknown. In this regard it would be especially important to define conditions that require the presence of a specific factor and give time stamps to the underlying events that happen in living cells. Hence, further studies that complement the current knowledge mainly obtained from structural analysis of precursors accumulating in depletion strains are necessary to put each of their roles into context. Nowadays, especially the opportunities presented by novel methods like super-resolution fluorescence microscopy (**1.3.3**) and the steady improvement of cryo-EM techniques should be seized to elucidate ribosome assembly *in vivo*.

1.3 Fluorescent proteins and fluorescence microscopy

The discovery of aequorin from *Aequorea victoria* (*A. victoria*) by Osamu Shimomura in the early 1960s marked the starting point of the incredible efforts

that have been made to investigate the functions and features of photoproteins[227]. Shimomura and colleagues caught approximately 50,000 jellyfish to isolate sufficient amounts of pure aequorin for the structural characterization of its chromophore[228]. During these studies, they found that an additional protein, the *green fluorescent protein* GFP, was the actual source of the characteristic green biolominiscence[227,229-231].

Several years later, during the 1990s, Martin Chalfie recognized the potential of GFP to be used as a fluorescent marker to monitor gene expression and protein localization and conducted first groundbreaking experiments in *Caenorhabditis elegans*, the results of which were published in *Science* in 1994[232]. In the same year, Roger Tsien and colleagues were the first to mutagenize GFP and found that they could generate fluorophores with altered spectra, as for example variants emitting blue light[233]. With this, they provided the basis for the design of the plethora of fluorescent proteins that are used today to address many questions in microbiology.

This revolutionary work by Osamu Chimomura, Roger Y. Tsien and Martin Chalfie was awarded with the Nobel Prize for Chemistry in 2008[234].

1.3.1 Green fluorescent proteins

A further breakthrough was achieved in 1966, when the crystal structure of *A. victoria* GFP was solved by two independent groups [235,236]. GFP is a 26.9 kDa protein of 238 amino acids and its tertiary structure was found to form a β-barrel that consists of eleven antiparallel strands, enclosing a central α-helix that harbors the chromophore group (**Figure 13)**.

Figure 13: Ribbon diagram of GFP and stick representation of the chromophore. The figure is based on PDB file 1EMA and was generated with pymol.

The autocatalytic mechanism that forms the green chromophore in GFP includes the cyclization of the three amino acid residues Ser65, Tyr66 and Gly67 of the peptide by the nucleophilic attack of the amide nitrogen of Gly67 on the carbonyl carbon of Ser65. The formation is completed with the dehydration of the carbonyl oxygen of Ser65 and the oxidation of the Cα-Cβ bond of Tyr66. These dehydration and oxidation reactions induce the formation of a conjugated π-electron system that allows the excitation and emission within the visible range.[233,237-239]

Since their discovery, numerous mutant forms of GFP have been generated, ranging from variants that differ in their maturation time, photostability, sensitivity or brightness and excitation/emission spectra, resulting in blue, cyan or yellow fluorescent proteins[240].

1.3.2 Red fluorescent proteins

In 1999, the discovery of the GFP homologue DsRed from the coral *Discosoma*[241] finally opened the door for the application of fluorescent proteins that emit light in the orange to red region of the spectrum. These variants are especially valuable, as they are excited with longer wavelength light, which decreases the risk of photochemical damage for the cells or tissues examined dramatically[242].

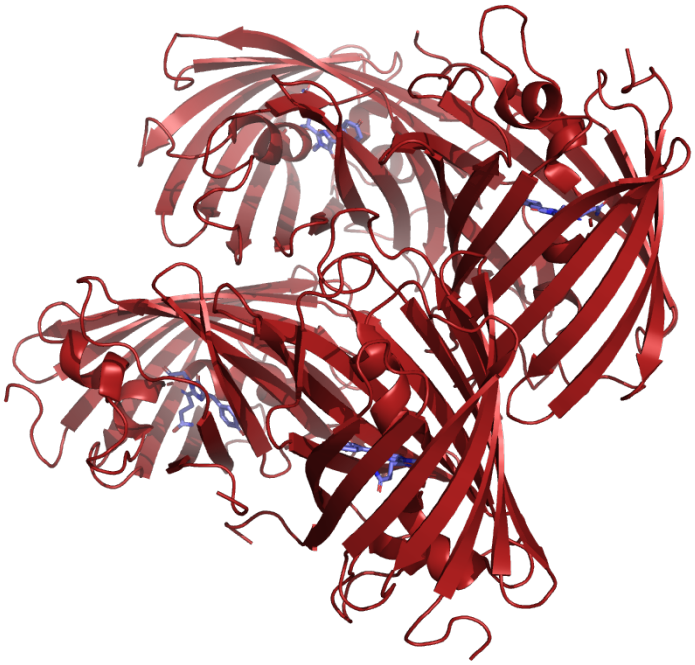

Figure 14: Ribbon diagram of DsRed tetramer and stick representation of the chromophores. The figure is based on PDB file 1G7K and was generated with pymol.

DsRed forms a stable tetramer with monomers that are similar to GFP – they form an 11-stranded β-barrel structure with an α-helix spanning through their interior, bearing the chromophore (**Figure 14**). The critical difference, however, presents in an extended conjugated π-system that shifts the excitation and emission spectrum to longer wavelengths. DsRed chromophore formation has long been hypothesized to proceed via a GFP-like intermediate state, followed by a second oxidation reaction of the Cα-N bond between the backbone nitrogen and the α-Carbon of

Gln66[243]. More recent models suggest maturation via a blue-emitting intermediate or in general, a branched pathway[244,245].

Similar to GFP, DsRed has also been used as basis for further mutational studies, resulting in the generation of monomeric variants that range from orange to far-red[246].

After years of engineering, the color spectrum of fluorescent proteins thus now spans the visible spectrum from blue to far-red with differences in brightness, photostability or maturation times, and also includes fluorescent proteins with special characteristics, like photoactivatable, photoconvertible and photoswitchable proteins or even the so-called fluorescent timers that change their emission wavelength over time[240].

1.3.3 Fluorescence microscopy

With the discovery of GFP and its potential to be used as biological marker, fluorescence microscopy has become a standard tool in biological research, allowing the visualization of protein interactions, dynamics and mobility. For a long time, especially confocal fluorescence microscopy was the method of choice, as it had overcome several limitations of conventional wide-field epifluorescence microscopy[247]. While the whole specimen is exposed to a light source in wide-field fluorescence microscopy, the use of point illumination and a pinhole allows elimination of out-of-focus signal, resulting in higher axial and lateral resolution[248].

It was long thought that the diffraction barrier[249] defined the limits of resolution in light microscopy, which is 200 nm in the lateral direction and 500 nm in the axial direction when imaging with visible light and a common oil immersion objective (numerical aperture = 1.4)[250,251]. The use of a laser scanning confocal microscope

was calculated to maximally add an improvement of resolution of ~ 30 % and thus, many sub-cellular structures and processes continued to remain elusive[247].

This resolution limit was overcome with the development of the so-called "*super-resolution*" techniques which allow resolutions as high as ~ 20-30 nm in the lateral and 30-50 nm in the axial direction[251,252]. With these techniques, a whole new level of quantitative and qualitative information can be obtained, including the determination of protein copy numbers[82,253], spatial distribution and co-localization studies with ~30 nm accuracy[82,254-257] and the determination of diffusion coefficients on sub-second time-scales[82,254].

Commonly used super-resolution techniques include "*structured-illumination microscopy*" (SIM), "*stochastic optical reconstruction microscopy*" (STORM), "*stimulated emission depletion*" (STED) microscopy and "*fluorescence photoactivation localization microscopy*" (fPALM). In 2014, Eric Betzig, Stefan W. Hell and William E. Moerner were awarded with the Nobel Prize for their contribution to "the development of super-resolved fluorescence microscopy"[250].

Consequently, several groups already used PALM and STED techniques to quantitively analyze the distribution of ribosomes in bacterial cells[83,255].

1.3.3.1 Structured Illumination Microscopy (SIM)

When introduced in 2000, SIM was one of the first super-resolution methods[258]. In SIM, sinusoidal patterned light is used to illuminate the sample. The illumination pattern and the structures of the specimen superimpose and interfere with each other and this way cause the formation of a new pattern, the so-called Moiré fringes (**Figure 15**). This resulting Moiré pattern "encodes" the actual high spatial frequency pattern of the original structures as a lower spatial frequency pattern that can be detected by the objective. For SIM, several images are recorded using

different illumination patterns (different phases and orientations). This way, additional image information is obtained and high-resolution images can be reconstructed. Using this method, resolutions of ~100 nm in the lateral and ~250 nm in the axial direction are possible.[247,258,259]

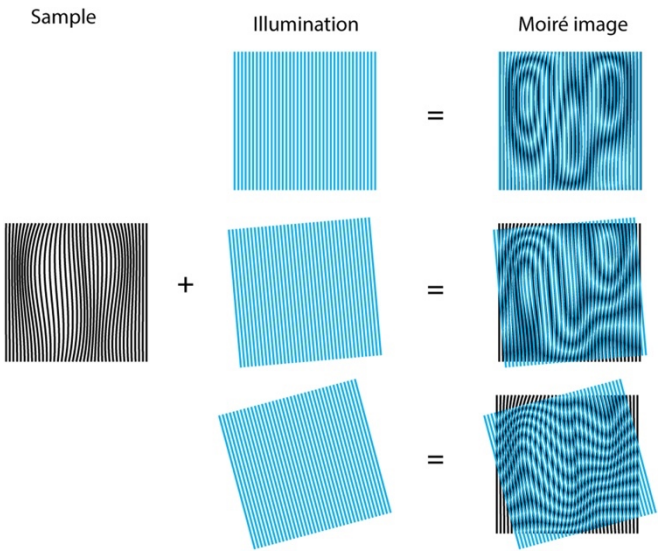

Figure 15: Principle behind SIM. A pattern of lower spatial frequency (Moiré fringes) is generated by interference of high frequency excitation pattern and sample structure. 3D-SIM acquisition is performed by laterally displacing the illumination pattern (five different phases) in three orientations (angles).[247] Figure republished by permission from Methods and Applications in Fluorescence, from Vangindertael et al., 2018. doi: 10.1088/2050-6120/aaae0c., permission conveyed through Copyright Clearance Center, Inc.

The advantage of SIM over the other super-resolution techniques is, that it is the least limited by dye/fluorescent protein or probe choice and thus is the most suited for multicolor imaging. Additionally, it provides the best time resolution with 1-2 images per second[247], which is a great advantage for live cell imaging. Thus, SIM is highly suitable to study the spatial organization and dynamics of single molecules or cellular structures and thus is another technique that should be considered for high-resolution fluorescence imaging of ribosomes.

1.4 Cryogenic electron microscopy (Cryo-EM)

The resolution achieved by imaging via light microscopy can be easily surpassed by electron microscopy (EM), which uses an electron beam instead of visible light to generate an image. Hence, it is not surprising that EM is the predominant method to study ribosomes in atomic detail[25].

In EM, an electron gun produces an electron beam, which is focused onto the sample. Several different possibilities exist of how these electrons can interact with matter (**Figure 16**), almost all of which can be exploited to obtain information about the specimen.

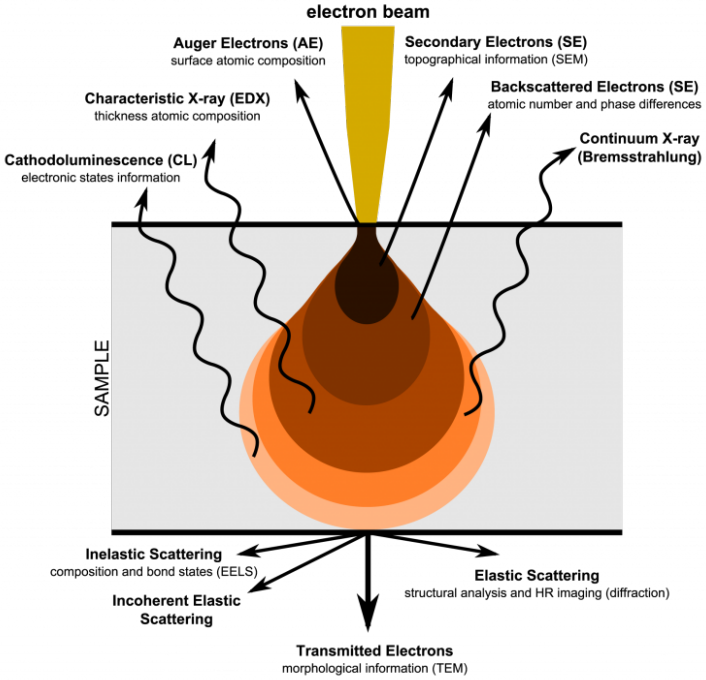

Figure 16: Schematic overview of electron-matter interactions. This illustration is licensed under CC BY 4.0.

In transmission electron microscopy (TEM), mainly elastically scattered electrons (only marginal loss of energy of incident primary electrons) and unscattered, transmitted electrons contribute to image formation. Thus, the specimen needs to be

very thin, or "electron-transparent" to allow electron penetration. An image-recording system then converts the electron image into some form perceptible to the human eye.[260]

Very early in the history of electron microscopy it was noticed that imaging of biological specimen is extremely challenging, as it is easily destroyed by intense high-energy electron beams. Moreover, biological material has extremely low contrast since it is mainly composed of elements with low electron density and additionally, beam induced particle movement complicates the analysis. The harsh high vacuum environment itself, that is necessary for the unimpeded travel of the electron beam, constitutes a further problem of the imaging of biological samples.[261,262]

The first successful approach to overcome these problems was the use of negatively stained biological material[263,264]. In this case, the specimen is embedded in a thin film of heavy metal salt (*e.g.* uranyl acetate, ammonium molybdate) that scatters electrons more strongly and thus provides better contrast[265].

Later, it was found that cooling of the specimen protects biological material[266] and today, a cryofixation method called plunge freezing is used to rapidly cool samples (*e.g.* a blotted thin film of liquid containing suspensions of macromolecules) by "plunging" them into a cryogenic liquid (*e.g.* ethane) to avoid the formation of ice crystals which diffract electrons strongly. Dubochet and colleagues developed this technique that allows the preservation of biological material within a thin layer of so-called amorphous ice. This sample preparation technique in combination with transmission electron microscopy in the 1980s marked the beginning of "Cryo-EM".[267,268]

In 1981, Joachim Frank described a novel computational method of image processing and analysis to obtain high-resolution data using TEM under low-dose

conditions. Briefly, randomly oriented particles (*e.g.* ribosomal particles) within a sample are irradiated with a low-dose electron beam, yielding multiple 2D projections of the specimen (micrographs). Similarly oriented particles are sorted into classes allowing the computer added calculation of a three-dimensional density map[269-272]. Such density maps often depict the structural average of a heterogeneous particle population (*e.g.* translating ribosomes in different stages of their duty cycle). To visualize this structural heterogeneity, special computer routines were developed to separate conformationally different sub states, a procedure termed multiparticle refinement[273].

All of these progresses contributed to the growth in the number of high-resolution structures within the last few years, but especially the development of direct electron detectors drove the "resolution revolution"[274,275]. In 2017, the work of Jacques Dubochet, Richard Henderson and Joachim Frank was awarded with the Nobel Prize "*for developing cryo-electron microscopy for the high-resolution structure determination of biomolecules in solution*"[276].

The advances in electron microscopy have always been closely linked to ribosome research. Starting with the seminal analyses in 1955, when Palade was the first to image "microsomes" directly in cells via electron microscopy to the numerous recent studies that employ single-particle cryo-EM to obtain high-resolution structures of ribosomal particles in complex with antibiotics to capture specific states during translation[277] and of course studies that capture the distinct structural features and composition of assembly intermediates to study ribosome assembly *ex vivo*. Moreover, recent developments in cryo-electron tomography allow the 3D visualization of biological samples at sub-nanometer resolution within their surrounding cellular context[278] and hence provide a powerful tool for structural analyses of ribosomes *in situ*[279-281].

2. Objectives

Six decades of research have provided important biochemical and biophysical insights on ribosome assembly, which is the process of generating ribosomal subunits. However, only with the advent of new technologies in both fluorescence microscopy and cryo-EM, the ribosome field is now equipped with tools to address the mechanistic details of this multilayered process.

Even though a fundamental cellular process, most of our current understanding of how ribosomes assemble is derived from *in vitro* experiments. While the artificial assembly of ribosomal subunits *in vitro* requires high thermal energy (up to 50 °C) to overcome energetic barriers, ribosome assembly *in vivo* employs enzymatic assembly factors to facilitate the process, which is classically divided in early, intermediate and late stages. This work focusses on late assembly of the large 50S subunit of *E. coli* and shall provide a systematic, functional analysis of the late acting assembly factors DbpA, EngA, EngB, RlmE and ObgE by the following experimental strategies:

1. Systematic analysis of assembly factors acting late in 50S maturation

- Depletion of the factors and phenotypic analysis of the corresponding knock down strains (*i.e.* growth at different temperatures).
- Biochemical and biophysical analysis of ribosomal subunit precursors accumulating in the absence of the assembly factors, using sucrose gradient centrifugation analyses.
- Analysis of cellular ribosome distribution upon assembly factor depletion, using strains with fluorescently labeled ribosomes in combination with super-resolution fluorescence microscopy (3D-SIM).

2. Isolation and purification of bona fide 50S precursors

- Generation of *E. coli* strains harboring assembly factors fused with affinity tags, applying knock-in methods and subsequent phenotypic characterization.
- Use of generated *E. coli* strain harboring StrepII-tagged ObgE to isolate the factor in complex with its bona fide precursor as a proof of principle approach.
- Utilize the isolated pre-50S•ObgE-StrepII complex for structural analysis (cryo-EM) to understand how ObgE contributes to the final maturation of the 50S subunit´s active site (*i.e.* the functional core).

3. Results

3.1 Systematic knock-down of assembly factors acting late on 50S maturation

The central reactions catalyzed by the ribosome (peptidyl transfer reaction and peptidyl hydrolysis) happen at the subunit interface of the 50S SU, which mainly consists of rRNA[49]. In a strict sense, the catalytic center that catalyzes these reactions, the peptidyl transferase center (PTC), is solely formed by the central loop of domain V (**1.1.1**, **Figure 3**) of the 23S rRNA[46]. However, adjacent helices and r-proteins make up a closely interacting network referred to as the "functional core" (**1.1.1, Figure 4**). This highly important functional region constitutes the tRNA binding sites and was found to form very late during the assembly process[156,157,159,160], indicating that the 50S SU obtains its catalytic capacity during these last steps.

In *E. coli*, there is a subset of five assembly factors that is associated with the maturation of the functional core, including the RNA helicase DbpA, the GTPases EngA, EngB, ObgE, and the methyltransferase RlmE[161-169] (**Figure 17**). A substantial amount of this information is derived from structural and biochemical analyses of ribosomal precursor particles accumulating in the absence of these individual factors. An overview of studies indicating their involvement in late 50S assembly is given in **table A1** (**Appendix**). Yet, a comprehensive analysis of late 50S assembly is still lacking. As most of these studies focus on the role of only a single, individual factor, using both different conditions and *E. coli* strain backgrounds, it is difficult to put these results into context. Moreover, an adequate phenotypic characterization of strains lacking the individual factors is usually missing, altogether limiting the mechanistic understanding of late 50S assembly.

As a first prerequisite for a systematic analysis of late 50S maturation, the five late-acting assembly factors (**Figure 17A**) were depleted in an otherwise identical genetic background to allow a proper comparison of their phenotypes.

A

Factor	Genomic organization	MW	Function	Position
ObgE (e)	*obgE* *yhbE* *rpmA* *rplU*	ObgE: 43.29 kD	GTPase	close to A-site
EngA (e)	*engA* *bamB*	EngA: 55.04 kD	GTPase	close to E-site
EngB (e)	*engB*	EngB: 23.56 kD	GTPase	?
RlmE	*ftsH* *rlmE*	RlmE: 23.34 kD	Methyltransferase	interacts with H92
DbpA	*ydnA* *dbpA*	DbpA: 49.20 kD	RNA helicase	interacts with H92

B

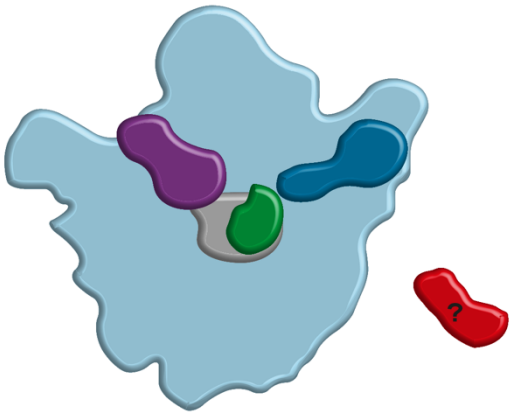

Figure 17: Overview of factors presumably involved in the maturation of the functional core. A) Depicted are the names, the genomic organization (operon), the molecular weight (MW), the functions and the approximate position at pre-50S/50S particles in *E. coli*. Colored arrows represent assembly factor genes. Grey arrows represent genes in the same operon. (e) indicates that the factor is essential. **B)** Approximate localization of the respective factors at 50S/pre-50S particles as described in literature[157,163,167,169,226,282] depicted as cartoon. Light blue area: pre-50S/50S SU; violet area: EngA; grey area: DbpA; green area: RlmE; blue area: ObgE. Position of EngB (red area) at the SU is unclear.

As three of the assembly factors (the GTPases EngA, EngB and ObgE) are essential and since traditional knock-out techniques in general bear a high risk of developing suppressor mutations, an inducible RNA-antisense strategy as described by Nakashima et al.[283,284] was chosen to allow a controlled depletion of each of the factors. This strategy provides an improved gene silencing tool for *E. coli*, as it makes use of antisense RNAs (asRNAs) that contain paired termini (PT), wherein flanking inverted repeats with high GC content create the paired double-stranded RNA. These PT were shown to provide enhanced stability[284] and thus allow to overcome the generally low silencing efficacy in *E. coli*. Moreover, simultaneous gene silencing of multiple genes is possible, allowing an investigation of functional relationships[283]. Moreover, this technique has already been successfully used to achieve depletion of ObgE in order to investigate its role in *E. coli* persistence[285], while the consequences on ribosome assembly have not been addressed.

Thus, IPTG-inducible expression vectors were generated, expressing PTasRNAs against *dbpA*, *obgE*, *engA*, *engB* or *rlmE* which hybridize with the ribosomal binding site and/or the 5' region of the target mRNA (**Figure 18**). This hybridization causes an inhibition of translation of the mRNA and thus a depletion of the respective assembly factor[283,284].

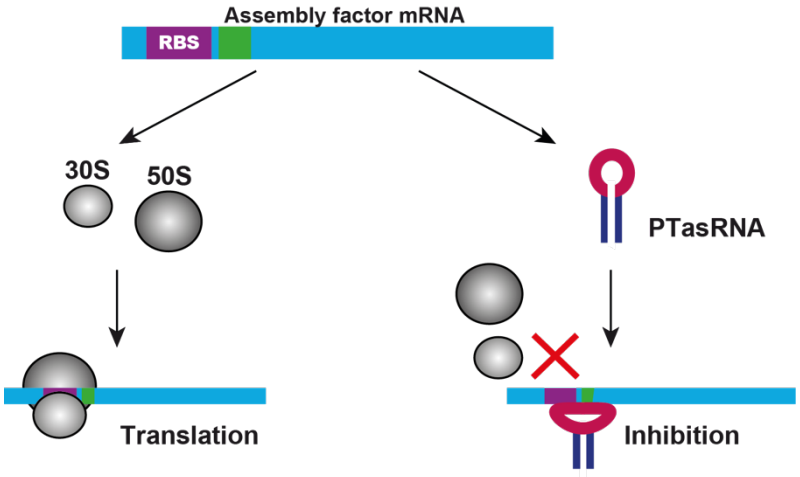

Figure 18: Principle of gene silencing using PTasRNAs as described by Nakashima et al.[284] Recognition of assembly factor mRNA by ribosomes and hence translation is prevented by hybridization of PTasRNA with RBS and/or 5′ region of target mRNA, resulting in a depletion of the respective assembly factor.

The strength of this strategy is that the same principal technique is applied to deplete each of the factors, using both identical strain backgrounds and growth conditions to compare the associated phenotypes.

3.1.1 Depletion of late assembly factors severely hampers cell growth

To obtain a first insight into the effects of late assembly factor depletion on overall cell fitness, growth of the knock-down strains was tested and compared to the wild-type strain at different temperatures (**Figure 19**). The strain background MG1655 was used for the analyses, as it belongs to the most extensively characterized wild-type laboratory *E. coli* K12 strains and has only few genetic manipulations from the archetypal *E. coli* K-12 strain[286].

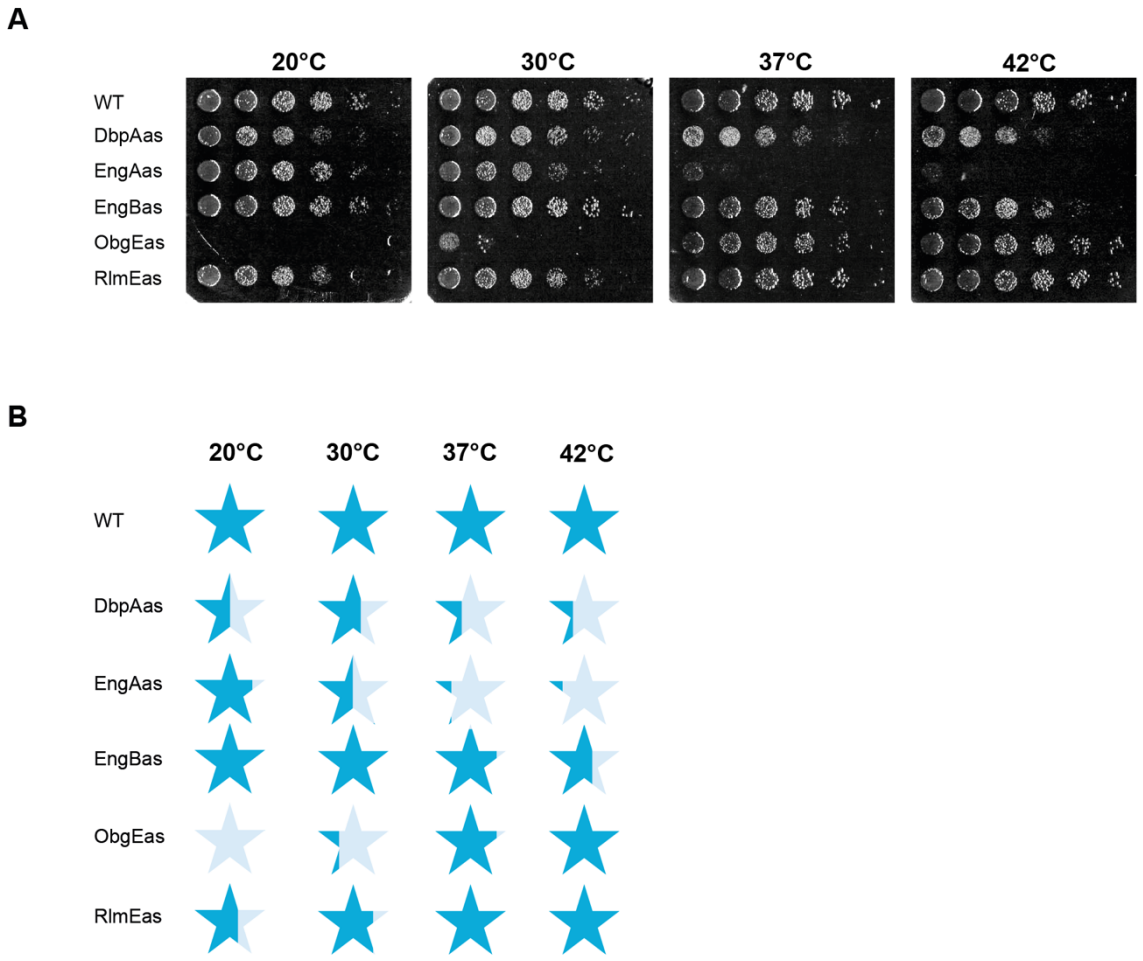

Figure 19: Cell growth at different temperatures upon assembly factor depletion. A) Growth comparison on solid medium: Cells of the indicated strains were spotted onto LB agar plates (supplemented with IPTG to induce assembly factor depletion) in a serial dilution and incubated at the given temperatures. **B**) Illustration of differences in growth behavior upon depletion of the respective assembly factors; non-quantitative. WT = MG1655. DbpAas, EngAas, etc. indicates the depleted assembly factor. Growth behavior

at given condition for each strain relative to wild-type strain MG1655 is depicted as colored star. Fully colored stars indicate growth behavior similar to the wild-type strain. Nuances in the severity of growth defects are illustrated by varying degrees of incompletely colored stars.

Upon IPTG induction, a significantly different growth pattern for each of the depletion strains could be observed. While a reduction of EngA levels was found to be specifically perturbing at higher temperatures and ObgE depletion caused severe growth defects below 37 °C, a depletion of the helicase DbpA caused a strong reduction of cell growth at all temperatures tested. In general, the effects of EngB and RlmE depletion were only minor, but revealed a sensitivity towards higher or lower temperatures, respectively.

Control experiments in the absence of IPTG were included and growth of all these transformants was indistinguishable from the wild-type strain, suggesting that side effects due to promoter leakiness can be excluded (**Figure A1,** Appendix).

Similar growth analyses were conducted with PTasRNAs expressed from different antisense vector backbones (pHN1009, pHN1257 and pHN687) that differ in their origin of replication (ORI). Due to the different ORIs, the copy number of the plasmids and thus the silencing efficacy can vary. The strongest effects on growth were observed upon expression from the backbone pHN1009, but the general trend was similar for all the different vector backgrounds (**Figure A2**, Appendix).

3.1.2 Free 50S subunits and slower migrating pre-50S particles accumulate in assembly factor depletion strains

An important indicator for ribosome assembly defects is the accumulation of ribosomal precursor particles. Thus, the ribosomal composition of all of the knockdown strains was determined by ribosome profile analysis. To visualize the nature of the potential precursor particles more precisely and to allow a distinction between earlier and later intermediates, the assembly factors were depleted in the background of the reporter strain **MGrg***. This reporter strain comprises one fluorescently labeled early assembly r-protein in each subunit[†], allowing the monitoring of assembly landscapes in ribosome profile analyses when combined with a fluorometric readout of the sucrose gradient fractions (**Figure 20A**)**.** The analyses were conducted at 25 °C as ribosome assembly in general is more susceptible at lower growth temperatures. For EngA and EngB depletion strains, absorption profiles were additionally recorded at 42 °C as they exhibited impaired growth at higher temperatures.

[†] The strain MGrg* was designed as an equivalent of the reporter strain MCrg* published by Nikolay et al., 2014[293] in *E. coli* MG1655 background.

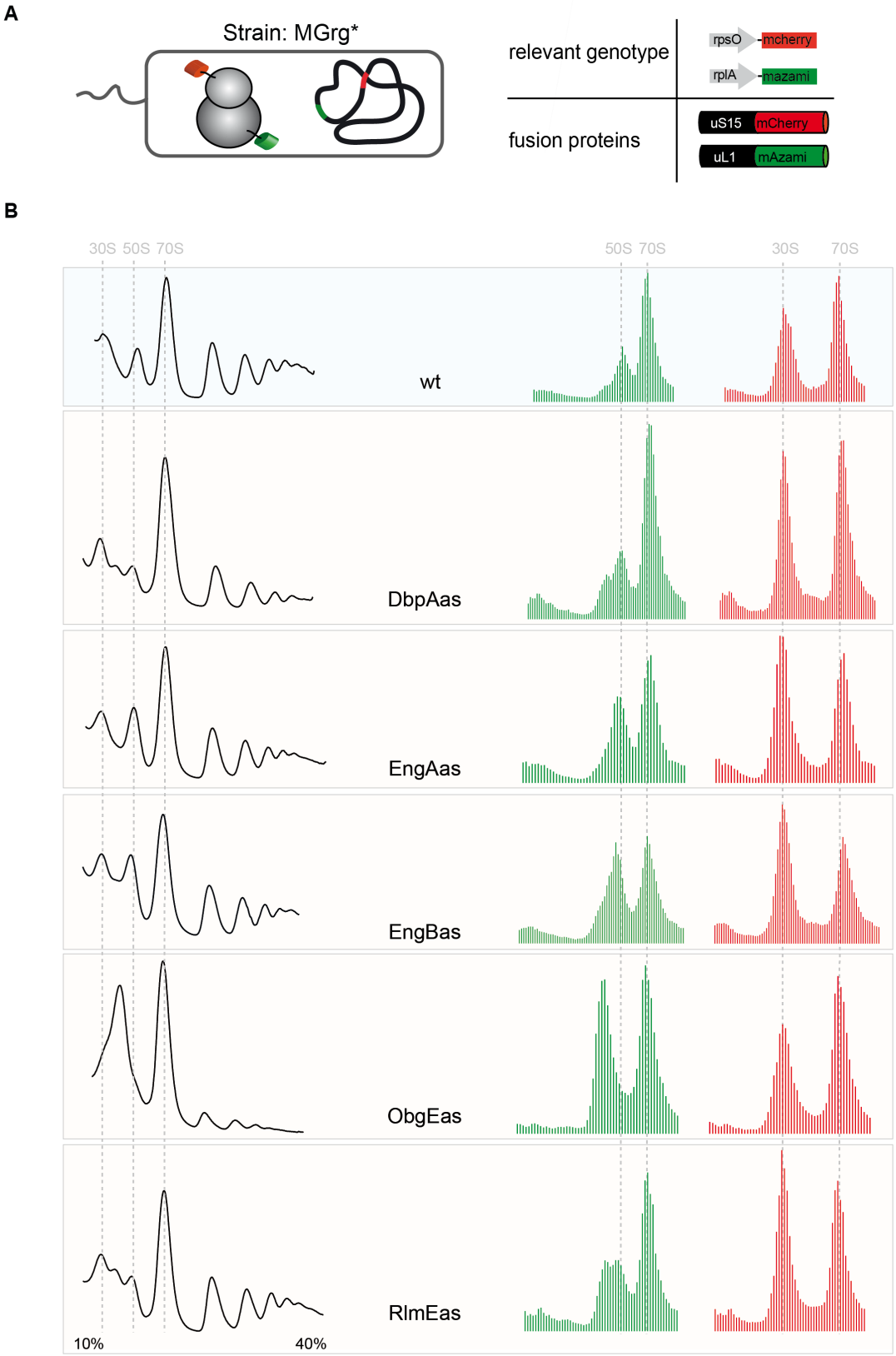

Figure 20: Strains depleted for late 50S assembly factors accumulate pre-50S and 50S particles. A) Schematic drawing of the reporter strain MGrg* harboring fluorescently la-

beled ribosomes. An early assembly protein of the small ribosomal SU (uS15) was endogenously labeled with mCherry and an early assembly protein of the large ribosomal SU (uL1) was labeled with mAzami green. **B)** Sucrose density gradient (10-40 %) centrifugation profiles from cells derived from MGrg* or MGrg* depleted for the assembly factors are indicated. Cells were cultured in LB medium at 25 °C in the presence or absence of IPTG until they reached an OD ~ 0.5 or for a maximum of 4 hours. Cleared lysates were subjected to sucrose gradient centrifugation and analyzed via A_{254} detection and fractionated. Sucrose gradient fractions were analyzed for mAzami- and mCherry-specific fluorescence. The fluorescence intensities were normalized to the 70S peak and are depicted in bar charts. Red bars represent mCherry-specific fluorescence; green bars represent mAzami-specific fluorescence. Dashed lines indicate the sedimentation behavior of mature 30S and 50S subunits and 70S ribosomes.

In all of the cases, the expression of the factor-specific PTasRNAs led to alterations of the ribosomal profile pattern when compared with the control strain MGrg* (**Figure 20B**). The strains expressing antisense constructs against DbpA and RlmE resulted in additional A_{254} signals for particles migrating slightly slower than a mature 50S subunit. The fluorometric analysis of the corresponding sucrose fractions revealed that these particles represent incomplete 50S precursors, as the peak of green fluorescence was asymmetrical and exhibited a shoulder in the area of the additional absorption signal. In the strain depleted for EngA the ratio of 50S and 30S subunits to 70S ribosomes was altered, as evident from the absorption profile and the fluorometric readout, indicating reduced 70S formation. Cultivation of EngA-depleted cells at 42 °C did exacerbate this effect, leading to a considerable accumulation of free, possibly defective 50S subunits (**Figure 21**).

Figure 21: Absorption profiles of cells cultivated at 42 °C depleted for EngA or EngB. Cells were cultured in LB medium at 42 °C in the presence or absence of IPTG until they reached an OD ~ 0.5 or for a maximum of 4 hours. Cleared lysates were subjected to sucrose gradient centrifugation and analyzed via A_{254} detection and fractionated. Sucrose gradient fractions were analyzed for mAzami- and mCherry-specific fluorescence. The fluorescence intensities were normalized to the 70S peak and are depicted in bar charts. Red bars represent mCherry-specific fluorescence; green bars represent mAzami-specific fluorescence. Dashed lines indicate the sedimentation behavior of mature 30S and 50S subunits and 70S ribosomes.

A similar alteration of the subunit to 70S ratio was observed in the strain expressing the antisense construct against EngB at 25 °C. Moreover, an increased A_{254} signal was observed in the region of particles migrating between mature 30S and 50S subunits. Additionally, the peak of green fluorescence was asymmetrical with a steep shoulder, indicating the presence of pre-50S particles. Ribosome profile analysis of EngB-depleted cells cultivated at 42 °C could not resolve enhanced pre-50S

accumulation (**Figure 21**). The strongest effect on ribosomal composition was found upon the depletion of ObgE, leading to a pronounced accumulation of green fluorescent particles migrating between mature 30S and 50S subunits, indicating the presence of significant amounts of incompletely assembled large subunits. Moreover, ObgE depletion additionally caused a severe reduction of polysomes. A second ObgE-specific PTasRNA variant targeting a different region within the ObgE mRNA (ObgEas_2; validated and published by Verstraeten et al., 2015[285]) was tested to corroborate the findings and indeed yielded a comparable ribosome profile with similar accumulation of immature 50S particles (**Figure A3,** Appendix).

Importantly, when cells were cultured in the absence of IPTG and PTasRNA expression was not induced, the absorption profiles were wildtype-like (**Figure A4**, Appendix). Slight discrepancies in the fluorometric readout can be explained by leakiness of the Ptrc-promoter, causing a low basal expression of PTasRNA.

Taken together, the depletion of each of the five assembly factors using the PTasRNA knock-down strategy provoked detectable defects in the assembly of the large ribosomal subunit and caused a considerable accumulation of pre-50S and/or free 50S or 30S particles in all cases. Moreover, all of the pre-50S particles were found to migrate only slightly slower than mature 50S subunits, indicating that they represent intermediates at late stages of 50S formation. In conclusion, these findings suggest that the assembly factors investigated indeed act late during 50S assembly.

It is now possible to isolate these pre-50S and 50S particles, which are all produced within the same *E. coli* background using the same gene silencing strategy, for further structural and functional analyses.

3.1.3 Assembly defects affect the spatial distribution of ribosomal particles

Although bacteria lack intracellular organelles, the cytoplasm of most prokaryotes exhibits some form of spatial organization. In *E. coli*, the nucleoid region containing chromosomal DNA is typically found in the cell center of mono-nucleoid cells, while ribosomal particles avoid the space near the axis of the cell and occupy the cell poles and the space near the cell wall[83]. Overall, previous analyses indicate that approximately 85-90 % of ribosomal particles are found at cell poles where they engage in translation[79-82] and only ~10-15 % localize within the nucleoid region, indicating strong ribosome-nucleoid segregation[82,83]. It is hypothesized that the 10-15 % of particles represent free ribosomal subunits or 70S ribosomes which engage in co-transcriptional translation or subunit precursors that are being assembled[82,287].

Interestingly, treatment of *E. coli* cells with different classes of antibiotics was found to cause severe redistribution of ribosomal particles. While translation inhibitors like chloramphenicol or tetracycline induced axial nucleoid contraction and a stronger DNA-ribosome segregation, the transcription inhibitor rifampicin led to nucleoid expansion and a uniform distribution of ribosomal particles[82,288]. Hence, it is conceivable that a stress situation caused by the absence of assembly factors, could also lead to a reorganization of ribosomal particles as well.

Previous fluorescence microscopic studies of r-proteins fused to fluorescent proteins allows analyzing the distribution of ribosomal particles within cells[82,288,289]. To investigate potential morphological changes upon assembly factor depletion, the distribution of ribosomal particles was thus followed by imaging of fluorescently-labeled uL1 and uS15 (using the reporter strain MGrg*) via 3D-SIM. DNA was stained with DAPI to visualize the nucleoid region.

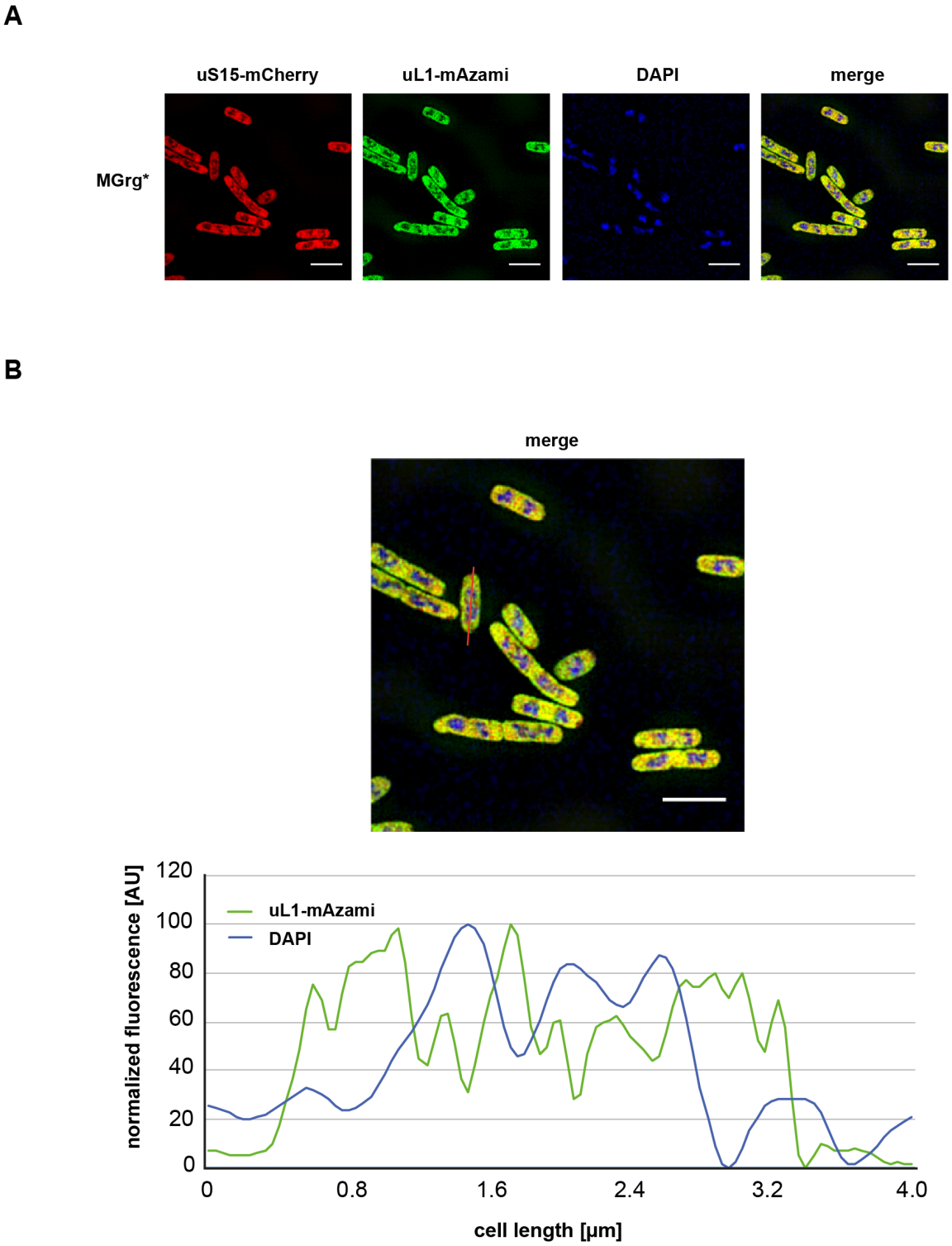

Figure 22: Distribution of ribosomal particles and DNA in unperturbed *E. coli* cells imaged by 3D-SIM. Fluorescence microscopic images of *E. coli* cells expressing uL1-mAzami and uS15-mCherry. Cells were grown at 37 °C in LB medium to OD_{600} = 0.5. DNA was stained with DAPI and cells were subjected to fluorescence microscopic analyses by 3D-SIM. Distribution of ribosomal subunits (green: uL1-mAzami-specific fluorescence; red:

uS15-mCherry-specific fluorescence) and chromosomal DNA (blue: DAPI staining) is depicted. An overlay was created (merge). Representative images are shown. **B)** Relative axial intensity distributions (y-axis) for a representative cell in the green and the blue channel were generated along a straight line (x-axis) through the longitudinal axis of the cells (red line in the magnification). Scale bar = 3 μm.

In general, the unperturbed reporter strain showed normal cell morphology and the expected fluorescence distribution of ribosomal particles (**Figure 22A**). The fluorescence signal indeed mainly spared the nucleoid regions (**Figure 22A,** merge) and concentrated to the cell poles, forming two "ribosome-rich regions". Generally, cells of varying length were visualized and as previously reported[289], mid-length cells and longer cells (>3.0μm tip-to-tip) exhibited a segregation of DNA into two major nucleoid lobes, resulting in the formation of a third ribosome-rich region in the cell center. This anti-correlation of ribosomal and nucleoid distribution was corroborated by the evaluation of axial fluorescence intensity profiles of uL1-mAzami and DAPI fluorescence (**Figure 22B**).

To assess whether defective ribosome assembly caused a reorganization of ribosomal particles, cells depleted of ObgE were imaged, since they exhibited the most severe defects as indicated by growth and ribosome profile analyses.

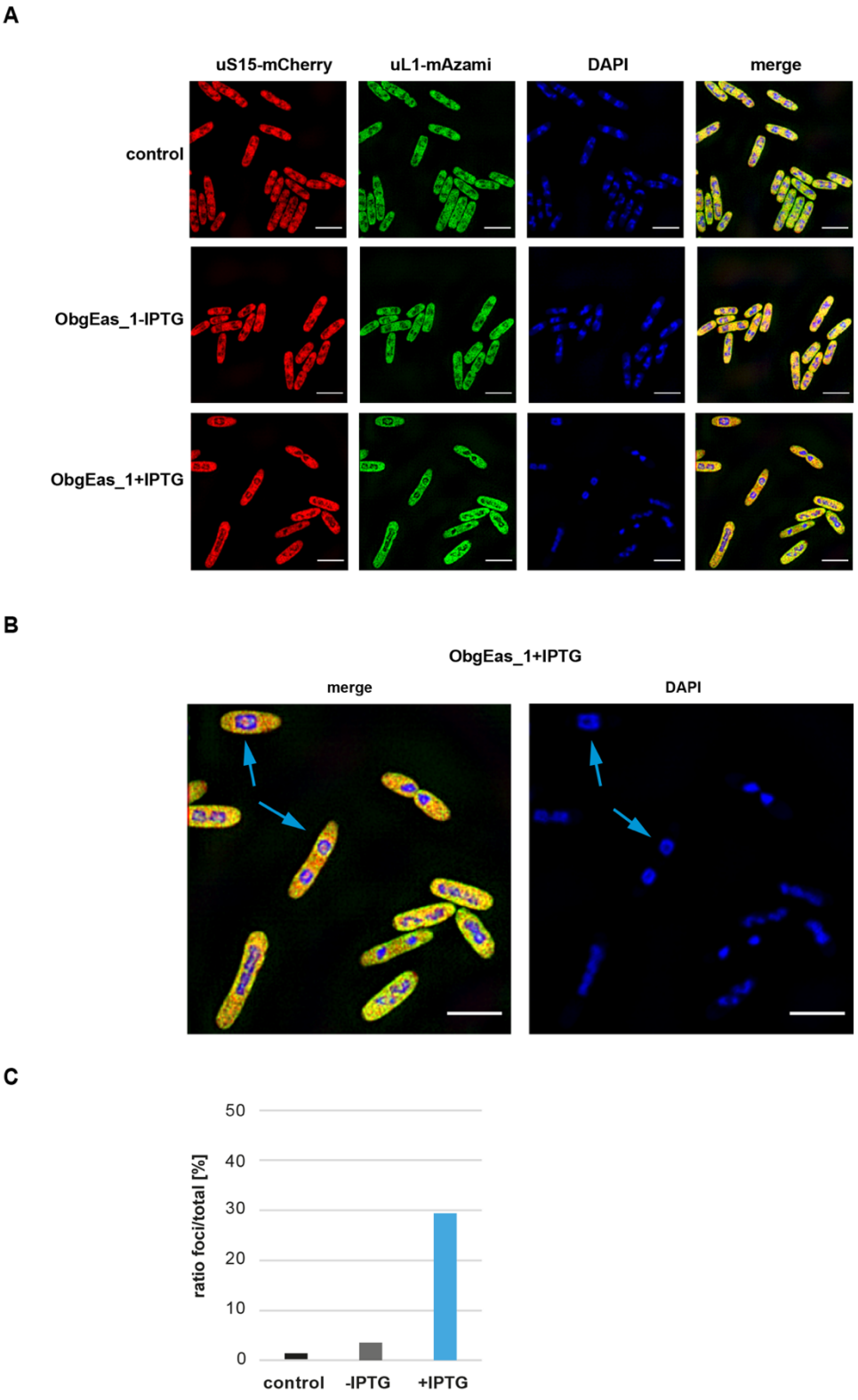

Figure 23: ObgE depletion causes a severe redistribution of ribosomal particles. A) Fluorescence microscopic images of *E. coli* strain MGrg* harboring ObgE-specific PTasRNA encoding plasmids were cultured in the presence or absence of IPTG and were compared

to the unperturbed strain MGrg*. Cells were grown at 37 °C in LB medium and PTasRNA expression against ObgE was induced at OD_{600} = 0.15 with 1 mM IPTG. Cells were harvested at OD_{600} = 0.5, fixed and DNA was stained with DAPI for subsequent microscopic analysis by 3D-SIM. Distribution of ribosomal subunits (green: uL1-mAzami-specific fluorescence; red: uS15-mCherry-specific fluorescence) and chromosomal DNA (blue: DAPI staining) is depicted. An overlay was created (merge). Representative images are shown. B) Magnification of ObgE depleted cells. Merge and DAPI stain are shown. Arrows highlight foci formation. Scale bar = 3 μm. **C)** Quantification of foci formation. The ratio of cells harboring foci relative to total cell count was determined. A number of ~200 cells was examined.

Depletion of ObgE caused cell elongation and even stronger ribosome-nucleoid segregation than observed in unperturbed cells. The ribosomal particles strictly localized to the poles and the peripheral regions (**Figure 23A** and **B** and **Figure A5**). Additionally, approximately 30 % of the cells exhibited compact, circular foci of green and red fluorescence within the "toroidal-shaped" nucleoid region (**Figure 23B**). Importantly, such morphological changes were not observed in the absence of IPTG when PTasRNA expression was not induced (**Figure 23A and C**).

This redistribution is reminiscent of cells treated with translation inhibitors, such as chloramphenicol[288,289]. It has been described that long-time exposure of cells to chloramphenicol induces continuous axial nucleoid contraction and a stronger DNA-ribosome segregation and hence results in a similar phenotype as observed in cells depleted of the late assembly factor ObgE. As aberrant translation is known to result in defective ribosome assembly[290,291], it is conceivable that cells treated with translation inhibitors share the same aberrant morphology.

To assess whether these morphological changes could be a general phenotype of assembly perturbation, the ribosomal protein uL3 was depleted and the distribution of ribosomal particles was analyzed. We previously showed that the absence

causes large subunit assembly defects, resulting in reduced 70S ribosomes and polysomes and a severe accumulation of pre-50S particles[290,292,293] (**Figure 24**).

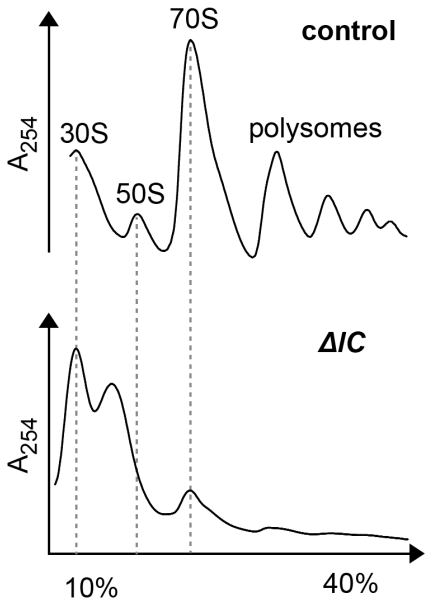

Figure 24: Absorption profiles of cells depleted for ribosomal protein uL3. Depicted are the absorption profiles of wild-type cells MC4100 (control) and cells depleted of uL3 (*ΔlC*). Figure adapted from Nikolay et al. with minor changes by permission from Oxford University Press. doi: 0.1186/s12867-015-0031-y., permission conveyed through Copyright Clearance Center, Inc.

In case the distinct distribution pattern observed in ObgE depleted cells should represent a common pattern for assembly defective cells, a similar distribution should be observed in cells depleted of uL3. For this purpose, the strain MCrg**ΔlC* was imaged[293]. This strain similarly expresses fluorescently-labeled uL1-mAzami and uS15-mCherry, but the gene *rplC* encoding the early essential ribosomal protein uL3 was replaced by a kanamycin resistance cassette. Additionally, the strain harbors a plasmid containing a wild-type copy of *rplC* under control of an IPTG inducible promoter. Withdrawal of IPTG thus results in severe assembly defects of the large ribosomal subunit.

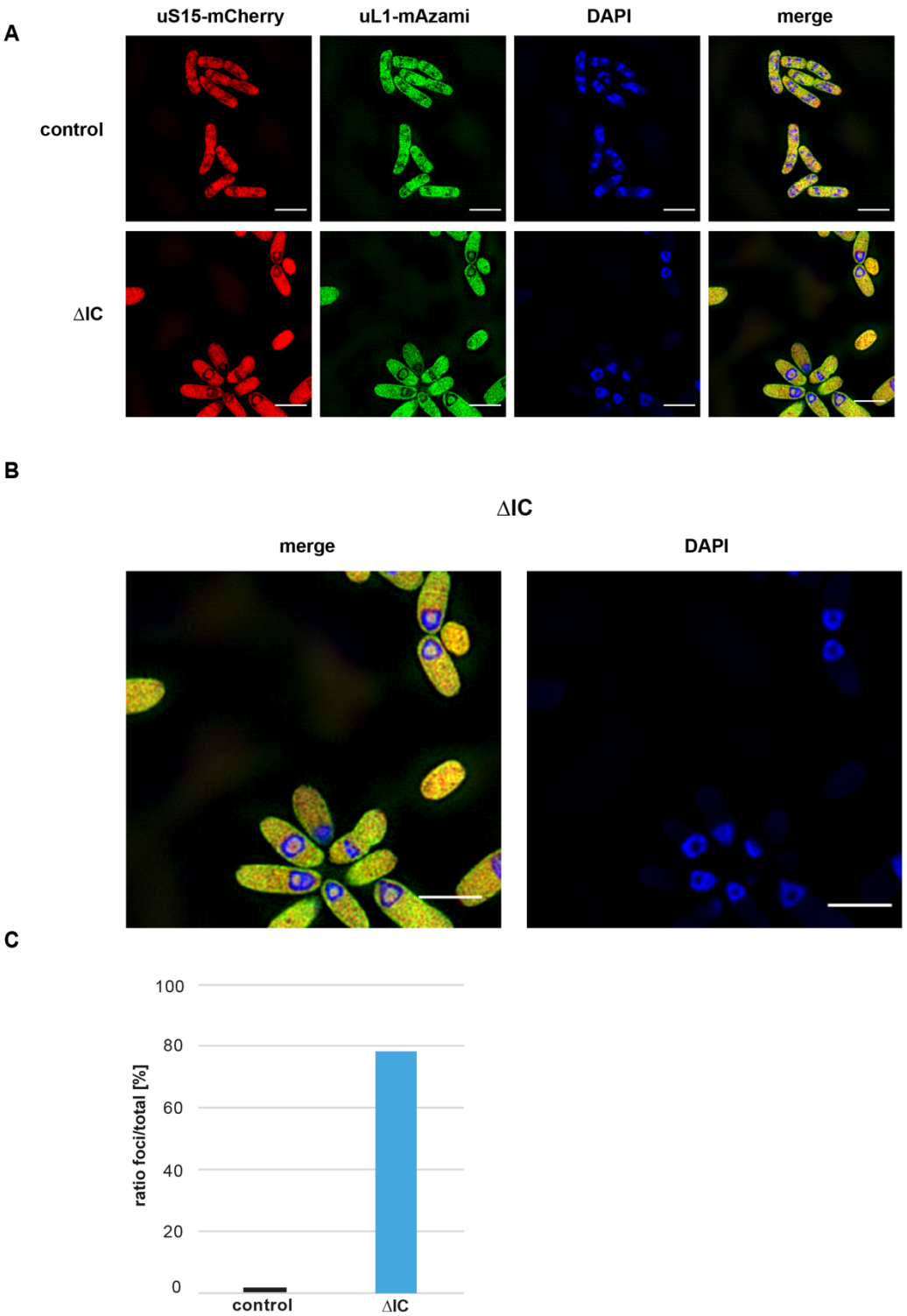

Figure 25: uL3 deletion causes strong ribosome-nucleoid segregation and ribosomal foci formation. A) Fluorescence microscopic images of strains MCrg* and MCrg**ΔlC*. Cells were grown at 37 °C in LB medium in the absence of IPTG to OD_{600} = 0.3-0.5, cells were

fixed, DNA was stained with DAPI and ribosomal particle distribution was analyzed by 3D-SIM. Distribution of large ribosomal subunits (green: uL1-mAzami-specific fluorescence) and chromosomal DNA (blue: DAPI staining) is depicted. An overlay was created (merge). Representative images are shown. Scale bar = 3 μm. **B)** Magnification of microscopic images showing DAPI signal and merge from *ΔlC* strain to illustrate ribosome-nucleoid segregtion. **C)** Quantification of foci formation. The ratio of cells harboring foci relative to total cell count was determined. A number of ~200 cells was examined.

Similar to the morphological phenotype of ObgE depleted cells, the depletion of uL3 caused cell elongation and a severe redistribution of ribosomal particles (**Figure 25A**). However, ribosome-nucleoid segregation and foci formation was even stronger than in ObgE depleted cells with the chromosomal DNA forming a distinct toroidal shape enclosing the ribosomal foci in the cell center. Approximately 80 % of these cells exhibited such foci formation (**Figure 25C**).

We previously designed and validated a reporter strain harboring dual fluorescently labeled 50S subunits that allows the discrimination of fully and incompletely assembles subunits by labeling one early (uL1) and one late (bL19) assembly protein[290‡]. While the fluorescence signal of the early assembly protein uL1 was shown to represent both fully and incompletely assembled subunits upon uL3 depletion, the fluorescence of the late assembly protein bL19 only represents fully assembled subunits.

Interestingly, fluorescence-microscopic analyses revealed an equal distribution of the uL1 and bL19 fluorescence signal (**Figure 26A and B**), indicating that precursors and subunits show an equal distribution pattern.

‡ Nikolay, R., **Schmidt, S.,** Schloemer, R., Deuerling, E. & Nierhaus, K. H. Ribosome Assembly as Antimicrobial Target. Antibiotics (Basel) 5, doi:10.3390/antibiotics5020018 (2016).[290]

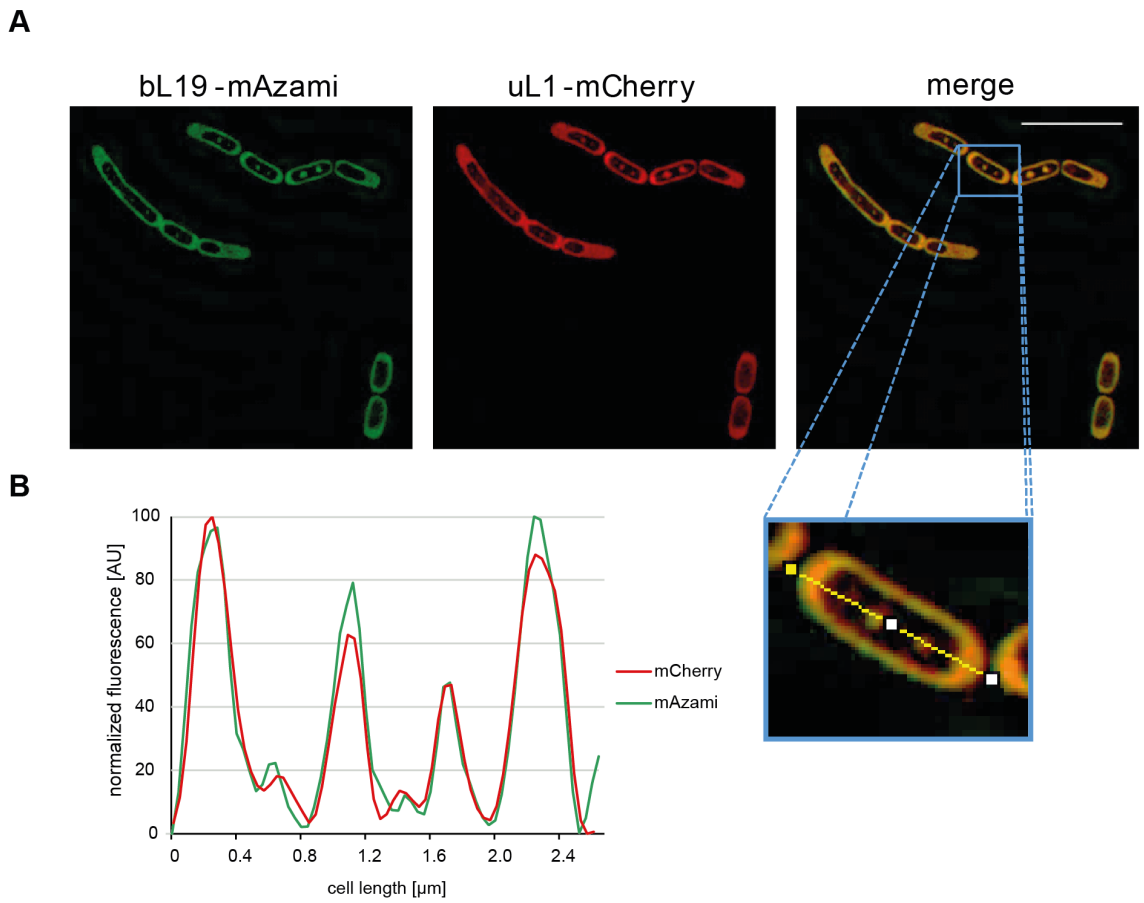

Figure 26: Super-resolution fluorescence microscopic images and fluorescence intensity profiles of strain expressing bL19-mAzami and uL1-mCherry depleted of ribosomal protein uL3. A) Cells were grown at 37 °C in M9 minimal medium to OD600 = 0.2- 0.4. Cells were subjected to super-resolution fluorescence microscopic analyses. Distribution of ribosomal subunits is shown (green: bL19 -mAzami-specific fluorescence emission; red: uL2 - mCherry-specific fluorescence emission). An overlay was created (merge). Representative images are shown. Scale bar = 5 µm. **B)** Relative axial intensity distributions (y-axis) for a representative cell in the red and the green channel along a straight line (x-axis) through the longitudinal axis of the cells (yellow line in the magnification).§

§ The microscopic analyses to assess the distribution of bL19 and uL1 upon uL3 depletion were conducted within the scope of the following work and are adapted from: **Schmidt, Sabine** (2016). Fluorescence-based analysis of ribosome assembly in *Escherichia coli*. Master's thesis. University of Konstanz.

In summary, the analyses suggest that there is a common morphological phenotype of assembly defective cells, resulting in the formation of ribosomal foci within a toroidal-shaped nucleoid

3.2 High-throughput screening for *in vivo* detection of subunit assembly defects in *E. coli*

The RNA-antisense approach revealed important information on the phenotypes of assembly defective cells. Especially the application of fluorescently labeled reporter strains proved to be a highly beneficial tool to confirm defective ribosomal subunit assembly. This knowledge can now be used to identify further factors that are involved in subunit formation. Literature already provides several potential or validated assembly factors that can be used to study further key steps besides functional core formation, but their number is inherently limited and additional tools are required. There is a lot of experimental data of drugs interacting with the ribosome (*e.g.* NMR or crystallographic data) that provided detailed information on the different steps of protein synthesis [294,295]. Similarly, it has been hypothesized that chemical probes could benefit the investigation of ribosome assembly[296,297]. However, despite universal efforts[296,297], until today no direct inhibitor of ribosome subunit assembly in bacteria and only a few for eukarya have been described[297].

To address this issue, we developed a screening setup that allows the detection of subunit assembly defects *in vivo* in a high-throughput compatible format to identify substances that specifically interfere with ribosome assembly[292**]. The strain MGrg used for the analyses harbors ribosomes with two labeled late assembly proteins (one in the large and one in the small ribosomal subunit). As selective inhibition of the assembly of one ribosomal subunit is supposed to cause an imbalance of the amount of 30S to 50S subunits in cells, assembly defects are detectable by

---

Nikolay, R. Schloemer, R., **Schmidt, S., Mueller, S., Heubach, A. and Deuerling, E. Validation of a fluorescence-based screening concept to identify ribosome assembly defects in Escherichia coli. Nucleic Acids Res 42, e100, doi:10.1093/nar/gku381 (2014).[292]

monitoring the relative amounts of subunits *in vivo* over time. Hence, significant changes in the fluorescence ratio compared to the unperturbed reporter strain indicate defects in subunit assembly[292]. In a high-throughput pre-screening (in collaboration with the Screening Unit of the Leibniz-Forschungsinstitut für Molekulare Pharmakologie (FMP) in Berlin) for inhibitors of bacterial growth, 307 small molecule inhibitors (out of ~30 000 compound library available at the FMP Screening Unit) were identified to significantly reduce the growth rate of *E. coli* MG1655. A secondary screening was conducted (in collaboration with Silke Müller, Screening Facility of the University of Konstanz) using the fluorescent reporter strain to identify substances from the pool of 307 growth inhibitors that would additionally cause an alteration of the fluorescence ratio indicating ribosomal assembly defects. Compounds exhibiting both a strong growth perturbation and alteration of the ratio were supposed to be validated further by ribosome profile analysis and fluorescence microscopy. As these results are very premature and need substantial further evaluation the data are given in the appendix only (**Figure A8**, Appendix).

3.3 Systematic analysis of affinity-tagged assembly factors acting late in 50S maturation

3.3.1 Generation of genetically modified strains harboring affinity tagged ribosome assembly factors.

The gene silencing study confirmed that the five assembly factors DbpA, EngA, EngB, ObgE and RlmE act late during 50S formation in *E. coli* and provided a comprehensive insight into consequences of aberrant late 50S assembly. Yet, it is necessary to isolate assembly factors attached to their native substrate, presumably pre-50S particles, to obtain detailed information on their binding site and mechanism of action. Thus, the second approach focused on the isolation and structural investigation of bona fide intermediates of late 50S assembly (**Figure 27**). For this

purpose, *E. coli* strains expressing endogenously StrepII-tagged assembly factors were generated to affinity-purify native pre-50S particles for subsequent structural analyses. The StrepII-tag was chosen, as the small peptide (8 amino acids) has been described to allow the purification of complexes under mild, physiological conditions with high yields[298].

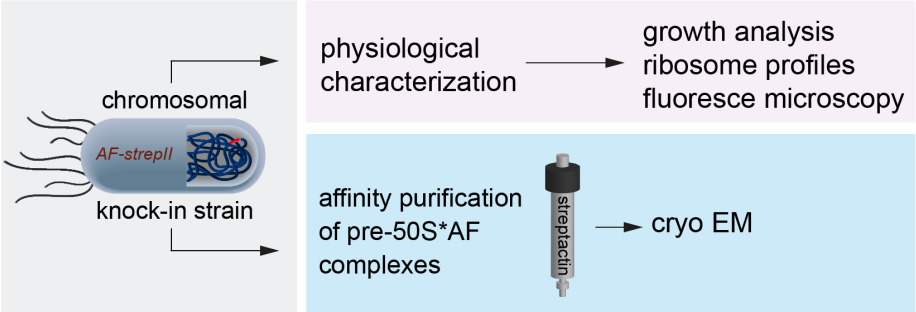

Figure 27: **Schematic overview of the workflow upon generation of knock-in strains expressing endogenously StrepII-tagged assembly factors.** *E. coli* strains expressing endogenously StrepII-tagged assembly factor (AF) were generated for subsequent affinity-purification and structural analyses of native pre-50S•assembly factor complexes via cryo-EM. Strains were physiologically characterized to guarantee unperturbed assembly.

3.3.2 Physiological and biochemical validation of strains harboring affinity tagged ribosome assembly factors

To test whether tagging of the assembly factors would interfere with their regular function, both growth and the ribosomal composition of the engineered strains was analyzed in detail.

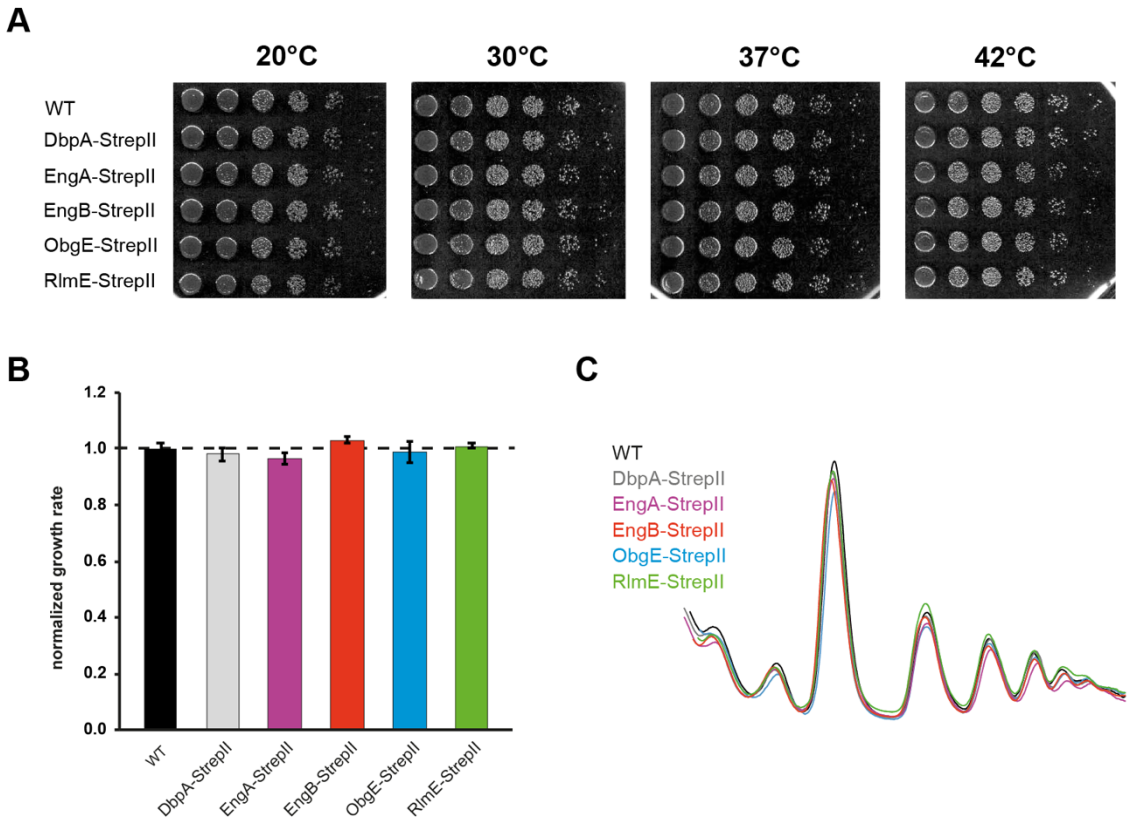

Figure 28: Phenotypic characterization of strains harboring affinity tagged ribosome assembly factors. A) Growth of the wild-type strain MG1655 was compared to the strains expressing DbpA-StrepII, EngA-StrepII, EngB-StrepII, ObgE-StrepII or RlmE-StrepII. Cells of the indicated strains were spotted onto LB agar plates in a serial dilution and incubated at the given temperatures. **B)** Growth analysis in liquid medium: Cells of the indicated strains were grown in LB medium in multiwell plates at 37 °C until stationary phase and A_{620} was determined every 30 minutes. Growth rates were calculated and normalized to the wild-type strain. N=8. Error bars show s.d. **C)** A_{254} profiles after 10 %-40 % sucrose gradient centrifugation of lysates derived from wild-type strain MG1655 and strains expressing DbpA-StrepII, EngA-StrepII, EngB-StrepII, ObgE-StrepII or RlmE-StrepII.

Spot-tests revealed that growth of the affinity-tagged strains and the parental strain were indistinguishable at all temperatures tested (**Figure 28A**). To analyze their growth behavior at optimal temperature more precisely, growth of the engineered strains was also tested in liquid culture at 37 °C in 96-well plate format.

Growth rate of the StrepII-tagged strains did not differ more than 5 % from the growth rate of the parental strain **(Figure 28B)**. Next, ribosome profile analysis was performed to investigate whether the tagging of assembly factors had any influence on the ribosomal composition of the engineered strains **(Figure 28C)**. Cell lysates were prepared from the different strains and loaded on a sucrose density gradient to separate ribosomal species by ultracentrifugation. Cells harboring the StrepII-tagged assembly factors did not show any differences in their ribosome profiles, as evident from the overlay of A_{254} curves. Additionally, the polysome levels were nearly identical, indicating that translation was not impaired and the ribosomal particles are fully functional. Thus, it was concluded that tagging of the assembly factors with a C-terminal StrepII epitope did not interfere with their assembly specific functions. Hence, all of the affinity-tagged strains are generally suitable for purification of pre-50S•assembly factor complexes.

3.3.3 Structure function analysis of the ribosome assembly factor ObgE in complex with a pre-50S precursor

Data of this chapter were obtained in close collaboration with Dr. R. Nikolay and Dr. T. Hilal and are part of and adapted from the manuscript which is currently under revision and entitled:

Snapshots of native pre-50S ribosomes reveal a biogenesis factor network and evolutionary specialization

R. Nikolay[1,*], T. Hilal[1,2*], S. Schmidt[3*], B. Qin[1], D. Schwefel[1], T. Mielke[4], J. Bürger[1,4], J. Loerke[1], K. Amikura[5,6], T. Flügel[1], T. Ueda[5,6], E. Deuerling[3] and C.M.T Spahn[1]

*These authors contributed equally to this work

1. Institut für Medizinische Physik und Biophysik, Charité – Universitätsmedizin Berlin, corporate member of Freie Universität Berlin, Humboldt-Universität zu Berlin, and Berlin Institute of Health, Berlin, Germany
2. Freie Universität Berlin, Research centre for electron microscopy, Fabeckstr. 36a, 14195 Berlin, Germany
3. Molekulare Mikrobiologie, Universität Konstanz, Germany
4. Microscopy and Cryo-Electron Microscopy Service Group, Max Planck Institute for Molecular Genetics, Ihnestr. 63-73, 14195 Berlin, Germany
5. Department of Computational Biology and Medical Sciences, Graduate School of Frontier Sciences, The University of Tokyo, FSB-401, 5-1-5, Kashiwanoha, Kashiwa, Chiba 277-8562, Japan.
6. Present address: Department of Molecular Biophysics and Biochemistry, Yale University, New Haven, CT 06511, USA
7. Present address: Department of Integrative Bioscience and Biomedical Engineering, Graduate School of Science and Engineering, Waseda University, 2-2 Wakamatsu-cho, Shinjuku-ku, Tokyo 162–8480, Japan

3.3.3.1 Detailed characterization of genetically modified strains harboring ObgE conjugated with StrepII or 3x FLAG tag

As co-purification of native pre-50S particles from prokaryotes via assembly factors as bait has never been described before, it was questionable whether affinity purification is generally possible and whether the purified amounts would be sufficient for subsequent structural analysis using cryo-EM. Since assembly intermediates are inherently low-abundant, first analyses were conducted using affinity-tagged ObgE, which is the most abundant of the late acting 50S assembly factors[299] and thus provides a favorable basis for the analyses. To allow biochemical analyses via western blotting, an additional strain expressing 3xFLAG-tagged ObgE was generated. Importantly, strains harboring either a StrepII- or 3xFLAG-tag conjugated ObgE exhibited normal growth at all temperatures tested and displayed wild type-like ribosomal composition (**Figure 29**), indicating that tagged ObgE entirely fulfills its functions irrespective of the choice of the tag.

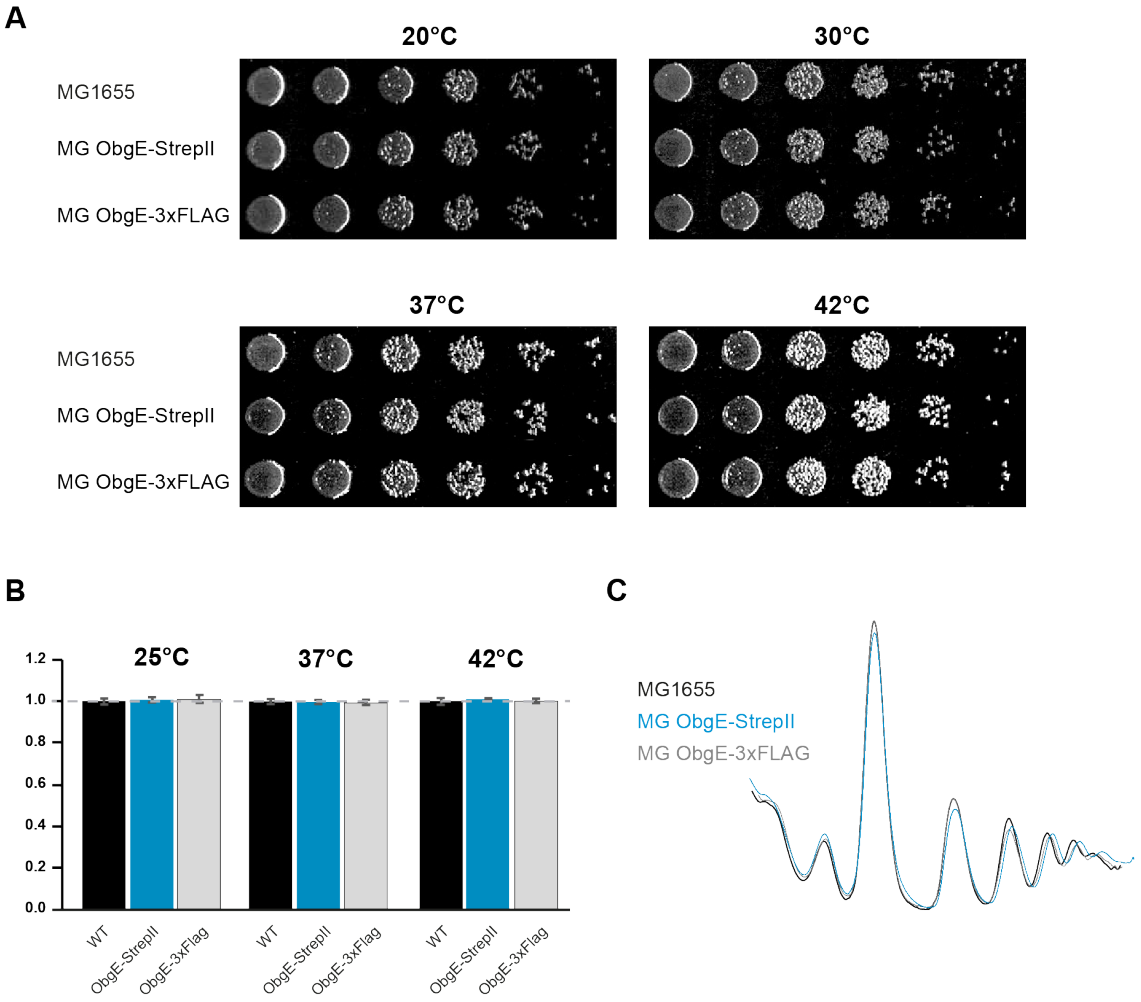

Figure 29: Phenotypic characterization of strains harboring affinity tagged ObgE. A) Growth of the wild-type strain MG1655 was compared to the strains expressing affinity-tagged ObgE. Cells of the indicated strains were spotted onto LB agar plates in a serial dilution and incubated at the given temperatures. Representative plates of three independent experiments are shown. **B)** Growth analysis in liquid medium: 25 ml cell cultures of the indicated strains were grown in LB medium at 25 °C, 37 °C or 42 °C in baffled flasks in a water-bath shaker and OD_{600} was determined every 30-60 minutes. Growth rates were calculated and normalized to the wild-type strain. N=3. Error bars show s.d. **C)** A_{254} profiles after 10 %-40 % sucrose gradient centrifugation of lysates derived from wild-type strain MG1655 and strains expressing affinity-tagged ObgE.

First, the supposed interaction between ObgE and ribosomal particles was assessed. For this purpose, cells harboring 3x-FLAG tagged ObgE were grown at 37 °C until early exponential phase and the cleared lysates were subjected to sucrose gradient ultracentrifugation. The separated ribosomal populations were investigated by ribosome profile analysis and the collected fractions were assayed for ObgE-3xFLAG by western blotting.

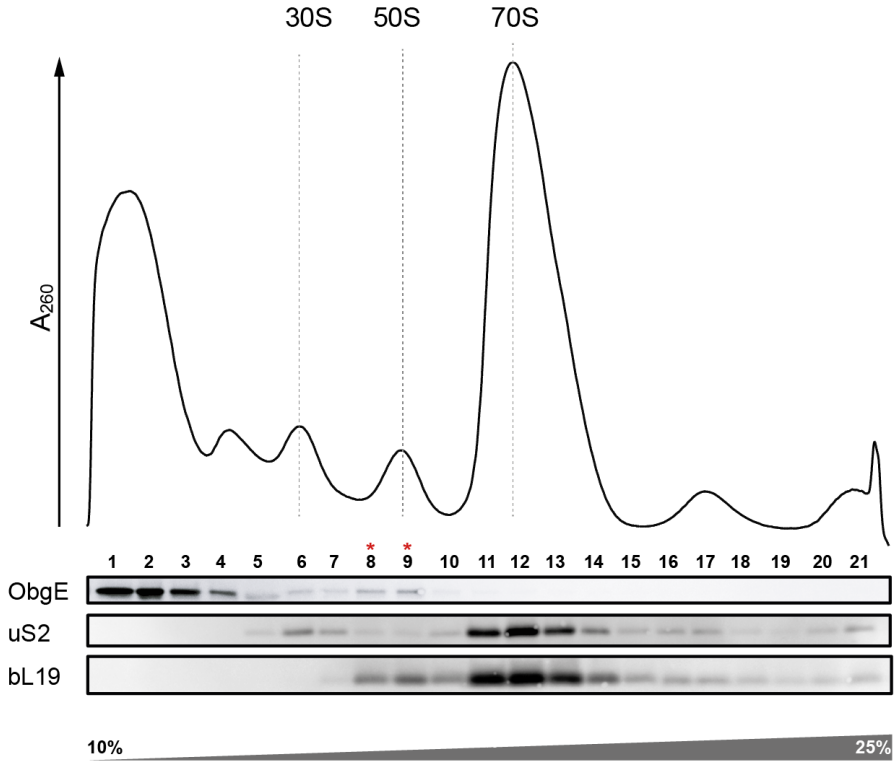

Figure 30: ObgE co-migrates with the 50S subunit. Cells of the strain MG1655 ObgE-3xFLAG were grown in LB medium at 37 °C and harvested by centrifugation. After sucrose gradient centrifugation, the centrifugate was analyzed and by A_{254} detection and fractionated. The indicated fractions were subjected to SDS-PAGE and western blotting and probed with anti-FLAG antibody. Red asterisks highlight fractions containing 50S/pre-50S-particles.

As reported previously[207], most ObgE was found within the cytosolic fraction (top of the gradient) and small amounts co-fractionated with the 50S subunit (**Fig-**

ure 30). This obvious co-migration with pre-50S/50S particles (**Figure 30**, red asterisks) and the massive accumulation of pre-50S particles upon ObgE knock-down (**Figure 20B**) suggest a direct role during 50S formation. Thus, lysates of the strain expressing ObgE-StrepII were subjected to affinity purification to allow isolation of these complexes.

3.3.3.2 Structural analysis of native pre-50S•ObgE complexes

To purify native pre-50S particles, the lysate of the strain expressing ObgE-StrepII was subjected to a Strep-TactinXT affinity matrix **(Figure 31)**[††].

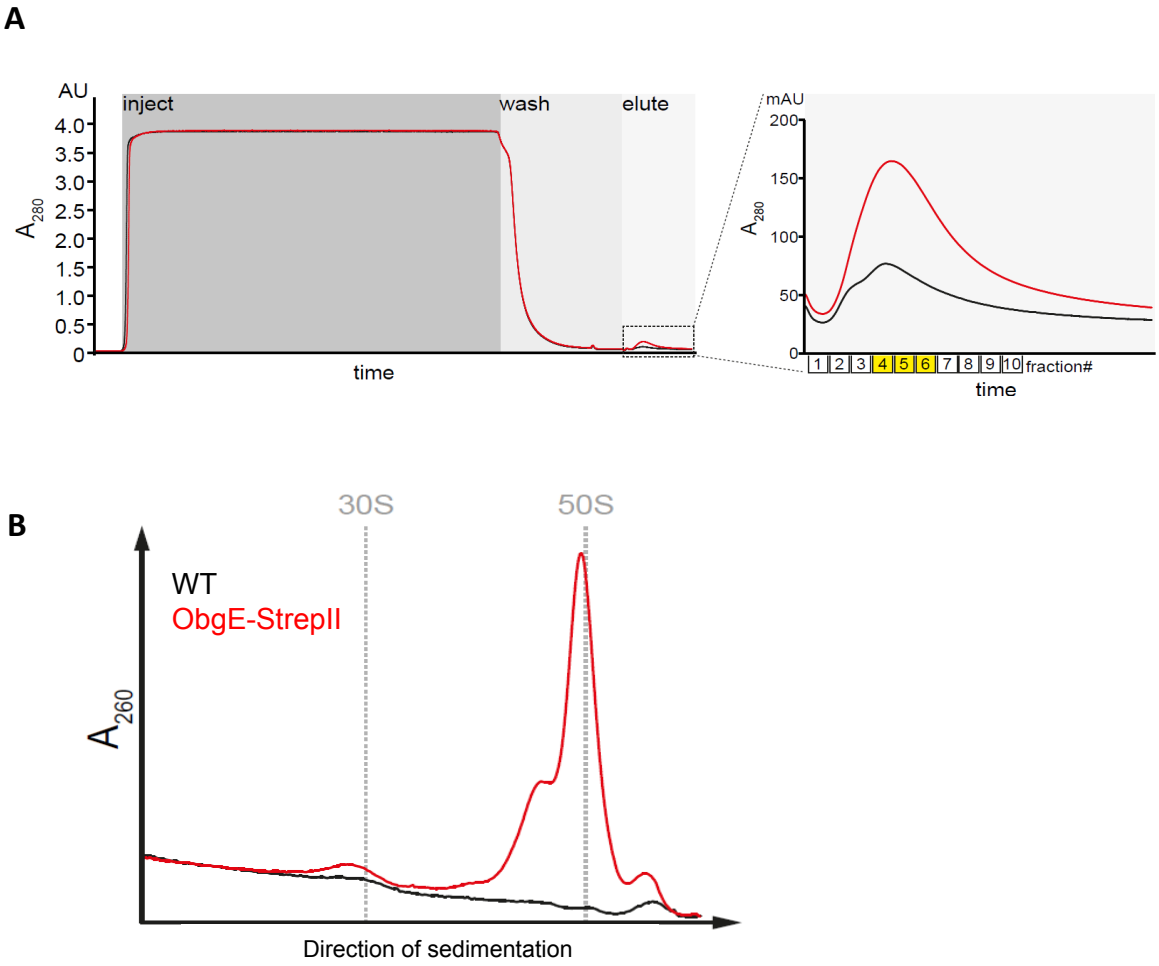

Figure 31. Affinity purification of ObgE-StrepII-tagged assembly factor complexes. **A)** The cell lysates of MG1655 (WT) or MG1655 ObgE-StrepII were loaded on a Strep-TactinXT Superflow High Capacity cartridge and StrepII-tagged ObgE (in complex with

[††] Affinity-purification of pre-50S•ObgE-StrepII complexes was performed by Dr. Rainer Nikolay.

ribosomal species) was eluted with 50 mM biotin. Plots of absorbance at 280 nm versus time are depicted. Additionally, a magnification of the elution profile is shown. Fractions that presumably contained ObgE in complex with ribosomal particles are highlighted in yellow. **B)** Analytical sucrose density gradient analysis of the fractions highlighted in (A). Dashed lines indicate the positions of mature 30S and 50S subunits.

Analytical sucrose density centrifugation of the eluate revealed that macromolecular complexes sedimenting with approximately 50S were isolated **(Figure 31B)**, indicating that the purification of pre-50S•ObgE-StrepII complexes was successful. Thus, the particles were subjected to cryo-EM analysis‡‡.

Single-particle cryo-EM analysis revealed the structure of a pre-50S•ObgE-StrepII complex with a nominal resolution of 3.4 Å, which exhibited an additional density that could be attributed to ObgE[169]. In the following, the characteristics of this particle - with a focus on the functional core - are described in detail.

In general, a comparison with mature 50S subunits revealed that the precursor exhibited mainly five distorted regions, including the CP, the uL1-stalk, the GTPase associated center (GAC), Helices 69-71 and importantly, the PTC and the functional core (**Figure 32**).

‡‡ Processing, modeling and analysis of multiple-particle cryo-EM data of pre-50S•ObgE-StrepII complexes was conducted by Dr. R. Nikolay and Dr. T. Hilal.

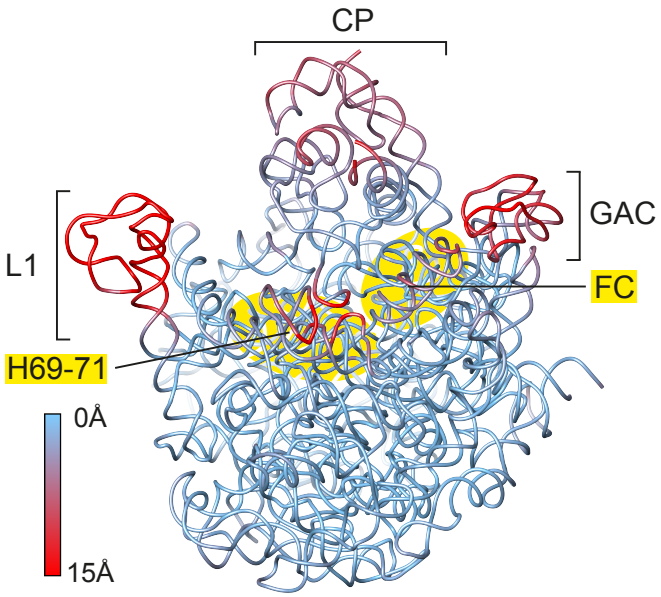

Figure 32: RMSD (root-mean square deviation of atomic positions) model highlighting deviations in rRNA conformation the precursor particle and a mature 50S subunit (0 Å (blue) - 15 Å (red)). The functional core (FC) and helices 69-71 are highlighted. GAC, GTPase-associated center (H43, H44) and CP (central protuberance) are indicated.

Interestingly, this particle exhibited three additional regions of extra electron density, corresponding to the assembly factors YjgA, RluD and RsfS, co-localizing with the immature areas described above (**Figure 33**).

The presence of YjgA and RluD, which have been suggested to be involved in maturation of the 50S subunit[207,300] and RsfS, which is known to act as an anti-association factor preventing 70S formation[301], further demonstrates that indeed, native intermediates have been purified.

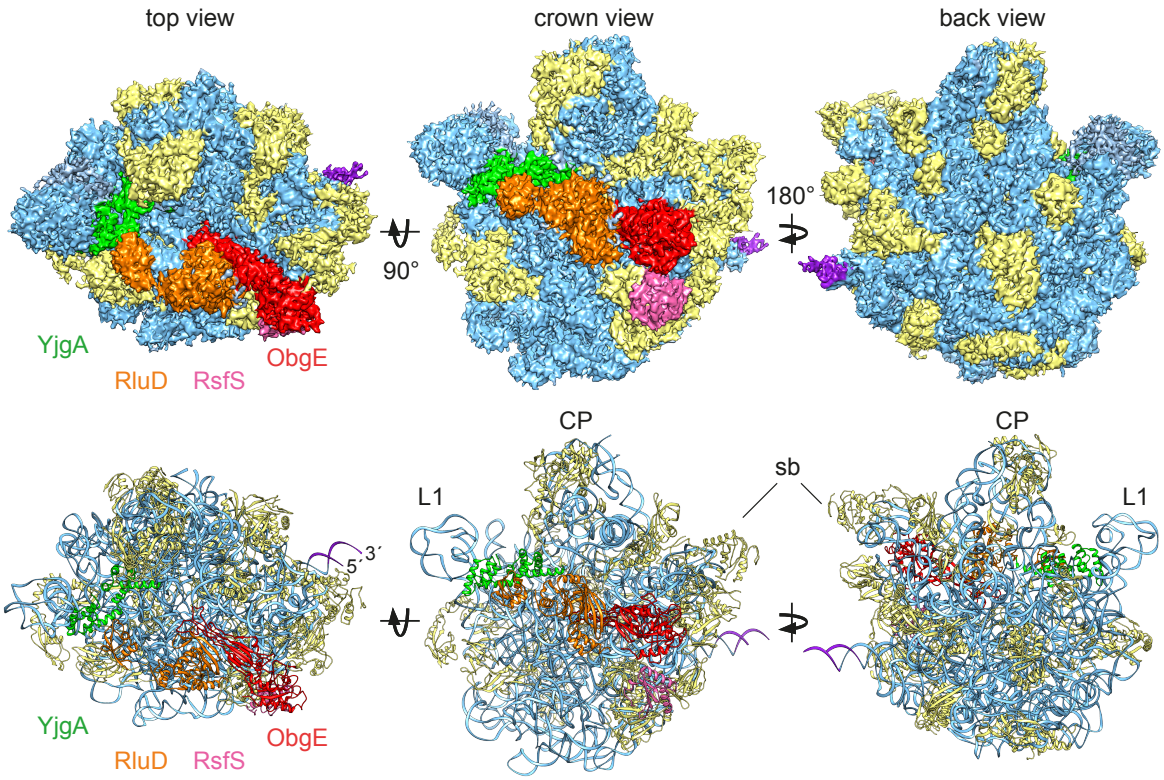

Figure 33: **A)** Map of precursor particle in top, crown and back view. Proteins are depicted in yellow, rRNA in blue. The assembly factors YjgA, RluD, RsfS and ObgE in green, orange hot pink and red, respectively. Incompletely processed 5′ and 3′ termini of the 23S rRNA are highlighted in dark violet. **B)** Corresponding PDB model with the same views and coloring. CP, central protuberance; L1, L1 stalk; sb, stalk base.

ObgE was found to be located directly below the bL12 stalk, occupying the area of the functional core (**Figure 33** and **Figure 34A**), indicating a direct role during its maturation. Interestingly, density for the functional core proteins bL36 and uL16 was found to be incomplete in the pre-50S•ObgE complexes.

In fact, the N-terminal domain of ObgE was found to undergo specific interactions with H89 (Arg60 contacts the tip of H89 (**Figure 34B**)), which is a central interaction partner of proteins uL16 (**Figure 34B**) and bL36. The non-canonical position of H89 is accompanied by a slight displacement of uL16 by ~2-4 Å and an even more pronounced shift of the CP (*cf.* bL25 and 5S rRNA) (**Figure 34B**).

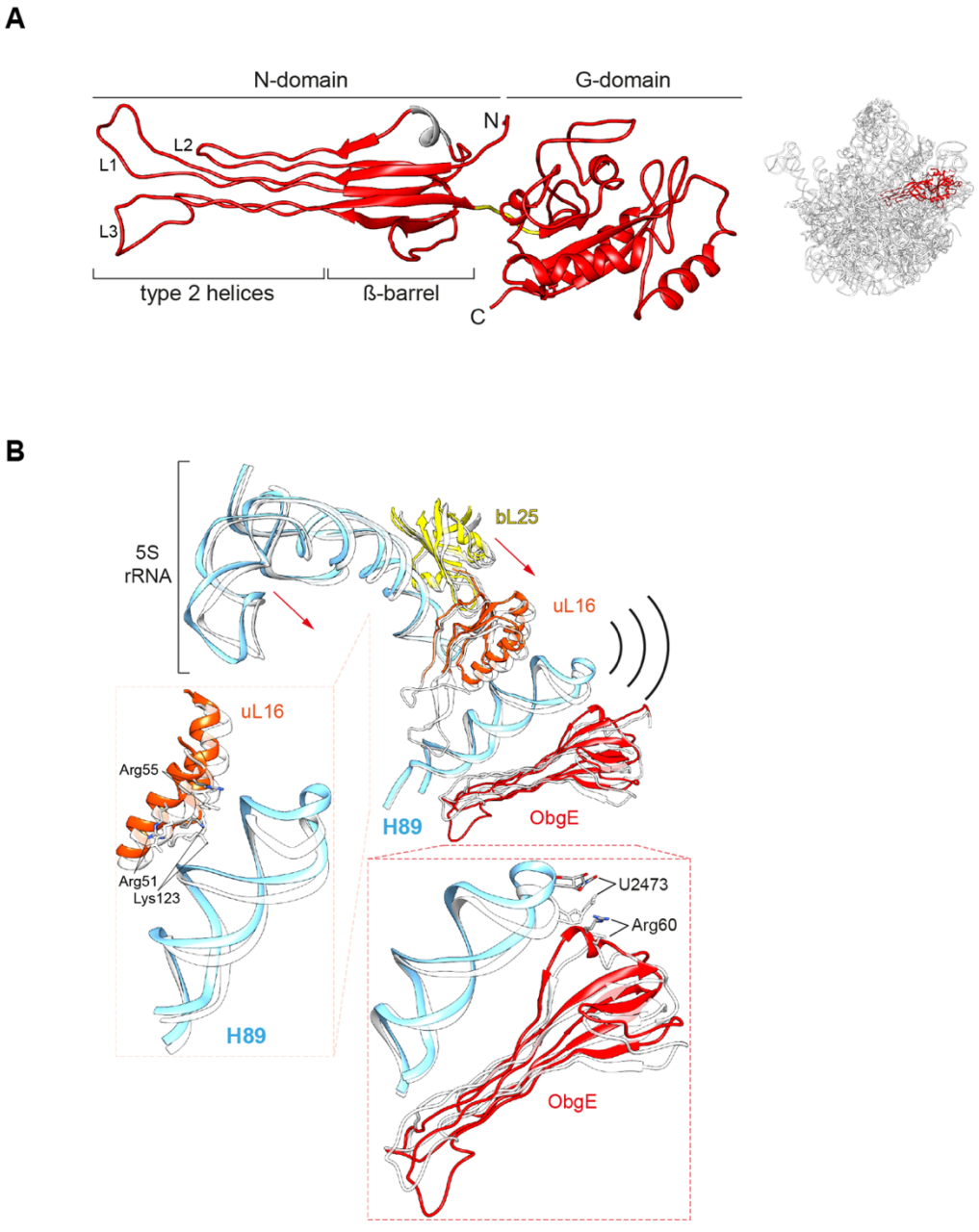

Figure 34: A) Domain architecture of ObgE (red). The N-terminal domain consists of six type-II helices connected by loops 1-3 (L1-L3), a ß-barrel domain and a short α-helix (gray),

which are connected by a highly conserved linker (yellow) with the G-domain (four-bladed beta sheet and five alpha-helices. N (N-terminus) and C (C-terminus) are indicated as resolved. The C-terminal amino acids 339-390 are not resolved in the cryo-map. Inset shows position of ObgE at the pre-50S particle. **B)** Pre-50S particle models of 5S rRNA, H89, bL25, uL16 and ObgE are shown in blue (both RNA moieties), yellow, orange and red, respectively. Red arrows indicate direction of a concerted movement involving all depicted RNA and protein elements. Models derived from 50S•ObgE•GMP-PNP in light gray to illustrate conformational differences in comparison to a more mature state. Close-up uL16 and H89: residues Arg51, Arg55 and Lys123 of uL16 interact with H89. Close-up N-terminal domain of ObgE and H89: nucleotide U2473 interacts with Arg60 of ObgE.

3.3.3.3 Absence of bL36 or uL16 favors ObgE occupancy on pre-50S subunits

To understand how ObgE contributes to the final maturation of the functional core, strains depleted of bL36 (knock-out) or uL16 (conditional knock-down) were generated and ObgE occupancy at 50S/pre-50S particles was analyzed. For this purpose, cleared lysates of the respective strains were subjected to sucrose gradient ultracentrifugation. The separated ribosomal populations were investigated by ribosome profile analysis and the collected fractions were assayed for ObgE-3xFLAG by western blotting (**Figure 35**).

The absorption profiles revealed that cells depleted of bL36 or uL16 accumulate free 50S and/or pre-50S assembly intermediates (**Figure 35B and C**) and immunoblotting indeed showed enhanced levels of ObgE in fractions corresponding to 50S/pre-50S particles (#8-11) (**Figure 35A-C**).

To quantify ObgE occupancy, a reporter strain producing endogenously fluorescently labeled uL1 (uL1-mAzami) and ObgE (ObgE-mCherry) was generated. Importantly, the unperturbed reporter strain exhibited normal growth at all temperatures tested and a ribosomal profile congruent with the one of the parental strain MG1655 (**Figure A7,** Appendix).

Proteins bL36 or uL16 were depleted and lysates of these strains were again subjected to sucrose gradient centrifugation. The isolated fractions were analyzed fluorometrically and the normalized fluorescence ratios (mCherry:mAzami corresponding to obgE:uL1) of each fraction were calculated. Indeed, higher occupancy of ObgE was observed in the fractions corresponding to 50S/pre-50S particles and the occupancy increased by up to 15-fold in the fractions #10 and #11. This suggests that the absence of either bL36 or uL16 leads to a prolonged association of ObgE, indicating that specific steps connected to ObgE involvement are perturbed and prevent the dissociation of ObgE. Hence, the maturation state of the functional core strongly affects ObgE occupancy, indicating a gatekeeper function.

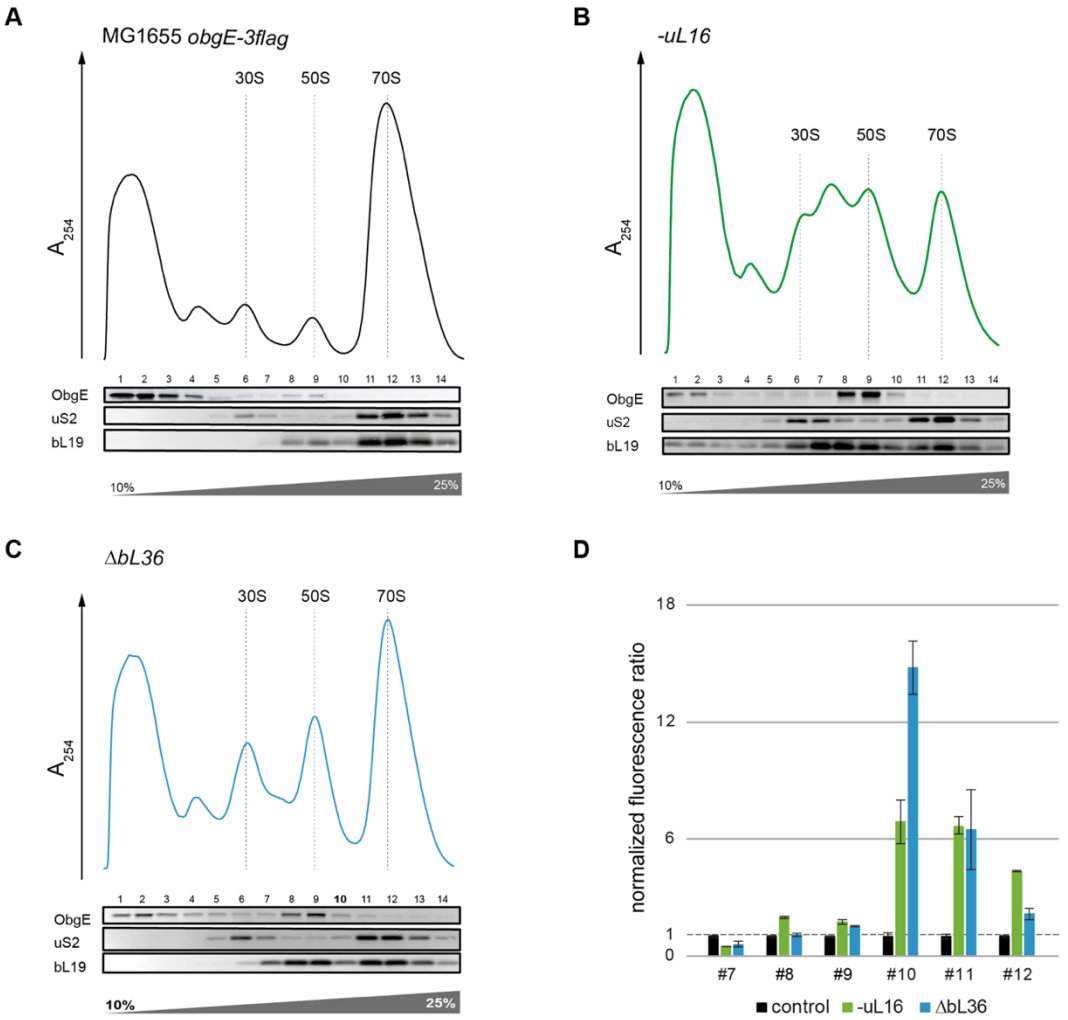

Figure 35: Absorption profiles after sucrose gradient centrifugation of lysates derived from **A)** MG1655 *obgE-3flag* (wild type, black), **B)** MG1655 *obgE-3flag rplP antisense* (-uL16,

green) and **C)** MG1655 *obgE-3flag ΔrpmJ* (ΔbL36, blue). The indicated fractions were subjected to SDS-PAGE and western blotting and probed with anti-FLAG-, anti uS2- and anti-bL19 antibodies. **D)** Lysates derived from MG1655 *uL1-mAzami obgE-mCherry* (control, black), MG1655 *uL1-mAzami obgE-mCherry rplP antisense* (-uL16, green) and MG1655 *uL1-mAzami obgE-mCherry ΔrpmJ* (ΔbL36, blue) were subjected to sucrose gradient centrifugation and fractionated. The normalized ratios between red and green fluorescence emissions were determined for the indicated fractions. N=2. Error bars show s.d.

Importantly, the deletion of late assembly proteins that are not part of the functional core do not result in higher ObgE occupancy (**Figure 36**).

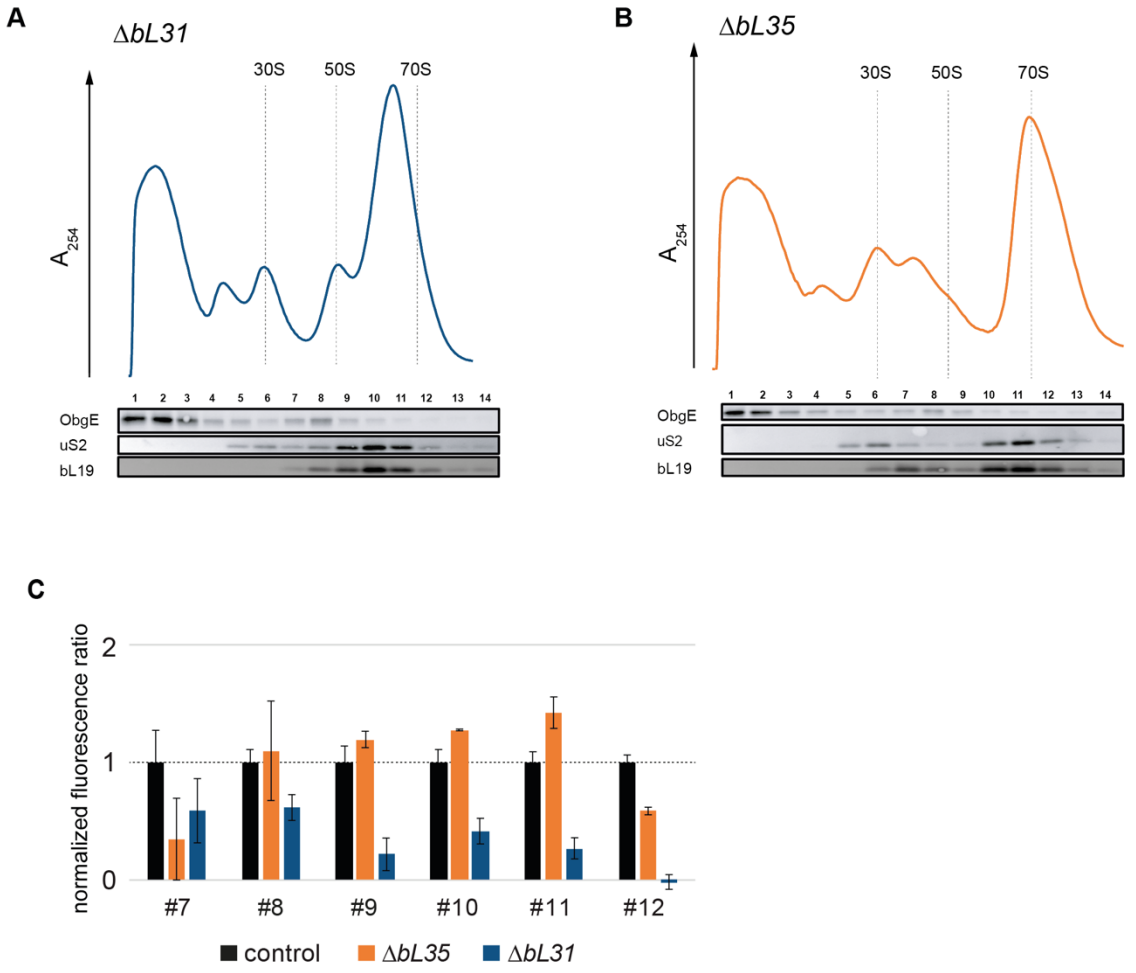

Figure 36: Absorption profiles after sucrose gradient centrifugation of lysates derived from **A)** MG1655 *obgE-3flag ΔrpmI* (ΔbL35, orange) and **B)** MG1655 *obgE-3flag ΔrpmE*

(ΔbL31, dark blue). The indicated fractions were subjected to SDS-PAGE and western blotting and probed with anti-FLAG-, anti uS2- and anti-bL19 antibodies. **C)** Lysates derived from MG1655 *uL1-mAzami obgE-Cherry* (control, black), MG1655 *uL1-mAzami obgE-Cherry ΔrpmI* (ΔbL35, orange) and MG1655 *uL1-mAzami obgE-Cherry 3flag ΔrpmE* (ΔbL31, dark blue) were subjected to sucrose gradient centrifugation and fractionated. The normalized ratios between red and green fluorescence emissions were determined for the indicated fractions. N=2. Error bars show s.d

4. Discussion and outlook

In general, the investigation of ribosome assembly *in vivo* is extremely challenging. This is not only because of the size or complexity of the ribosome itself, but also due to the numerous assisting factors that significantly accelerate the process. Hence, *in vivo* assembly is completed within a time-scale of ~ 2 min in rapidly growing *E. coli*[135], producing highly dynamic pre-ribosomal particles. As a result, it is difficult to isolate particles in different intermediate stages to dissect the key steps of subunit formation. This work focused on two complementary approaches that address the issues described above to provide a holistic view on late 50S assembly *in vivo*.

The first approach involved a previously validated PTasRNA-based strategy to deplete five different factors that were proposed to be involved in late 50S assembly. The phenotypes of these depletion strains were systematically studied to analyze the consequences of late assembly factor depletion. It could be confirmed that each of the factors plays a role during late 50S maturation in *E. coli*, as their absence caused an accumulation of pre-50S and/or free 50S particles. Cellular growth defects of the strains generally differed in severity and were strongly dependent on temperature. Moreover, microscopic analyses revealed that assembly defective cells, caused by depletion of either ObgE or ribosomal proteins, show a redistribution of ribosomal particles, exhibiting strong ribosome-nucleoid segregation and the formation of ribosomal foci that are entrapped by toroidal-shaped nucleoids.

The second strategy aimed at the affinity purification of authentic ribosomal precursors using assembly factors as bait. For this purpose, strains expressing endogenously StrepII-tagged assembly factors were generated and phenotypically characterized to ensure that each of the factors maintained its normal cellular function.

Pre-50S•ObgE-StrepII complexes were successfully purified and subsequently analyzed via cryo-EM. The pre-50S•ObgE-StrepII cryo-EM reconstruction exhibited additional extra density that could be attributed to the assembly factors YjgA, RluD and RsfS. The precursor particle exhibited five distorted areas, including the CP, the uL1-stalk, the GTPase-associated center, Helices 69-71 and importantly, the PTC and the functional core. As described in previous studies, ObgE was found to bind close to the A-site, spanning the area from the PTC to GAC, indicating a direct role during functional core formation. This was further corroborated by the finding that the maturation state of the functional core strongly affects ObgE occupancy.

In summary, this study describes the first systematic approach to simultaneously investigate the role of five different assembly factors acting late during 50S maturation. It thus provides a comprehensive overview of the consequences of assembly factor depletion on cell fitness, ribosomal composition and distribution of ribosomal particles in assembly defective cells and allows a direct comparison of the phenotypes.

Moreover, this is the first time that an affinity-tagged assembly factor was successfully used as bait to purify native ribosomal precursors from *E. coli*, allowing detailed characterization of these particles via cryo-EM. Additionally, the study provides in total five phenotypically validated strains expressing endogenously StrepII-tagged assembly factors that offer a toolbox for further structural and biochemical analyses of authentic ribosomal precursors.

Hence, this work marks a starting point for further in-depth analyses of ribosome assembly and paves the way for future perspectives that will be discussed below.

4.1 Effects on growth and ribosomal composition upon assembly factor depletion differ in severity

4.1.1 Systematic analysis of assembly factor depletion

Ribosomal subunits can be assembled *in vitro* using their purified rRNA and protein components. However, this process requires supply of thermal energy, to overcome energy barriers and convert trapped intermediates into mature subunits[302-304]. Assembly factors are thought to facilitate these processes *in vivo*[75,144,145,151-153]. Indeed, ribosome assembly is generally susceptible to low temperatures and thus, defects are often exacerbated below 37 °C. To assess the effects of assembly factor depletion, growth of the knock-down strains was tested and compared at different temperatures.

Surprisingly, cell growth of the five different depletion strains varied significantly, with some of the strains exhibiting sensitivity towards higher temperatures (*e.g.* upon depletion of EngA) and others showing cold-sensitivity (*e.g.* upon ObgE depletion). The diverse growth pattern indicates that the five assembly factors are required under different (stress) conditions. This agrees with earlier studies proposing that there are multiple parallel assembly pathways *in vivo* that allow the process to be completed in case a specific step is blocked[153].

Depletion strains of all of the five assembly factors with exception from EngB have been investigated in previous studies in *E. coli*. However, it is difficult to compare the results, as different approaches and strain backgrounds have been used for assembly factor depletion. Moreover, many of these studies did not focus on their possible role during ribosome assembly. This is especially true for ObgE which is linked to all kinds of cellular processes. Additionally, a comprehensive phenotypic analysis of these strains is often missing.

Previous studies mostly used temperature-sensitive alleles to deplete functional ObgE protein in *E. coli*[199,207,208], causing an accumulation of pre-ribosomal particles migrating at 50S[207]. Similarly, ObgE depletion induced by PTasRNA expression resulted in an accumulation of particles migrating at 50S at 37 °C (**Figure A6,** Appendix). However, analysis at 25 °C revealed an even stronger assembly defect, indicating that ObgE depletion causes severe cold-sensitivity that has not been demonstrated before.

Other studies similarly focused on the role of ObgE under specific stress conditions, *e.g*. sensitivity of mutants to the replication inhibitor hydroxyurea to determine effects on DNA replication[305] or the formation of persister cells upon ObgE depletion via PTasRNAs[285]. Furthermore, a conditional knockout mutant of ObgE was characterized with respect to chromosome segregation and cell division[198]. Yet, the consequences of ObgE depletion were often solely assessed at optimum temperature and generally, the use of temperature-sensitive alleles does not allow an adequate phenotypic analysis, as these mutants often exhibit complex effects on the proteins function.

As pointed out above, ObgE depletion leads to pleiotropic effects, as does depletion of various other assembly factors[297,306,307]. Since correct ribosome assembly is integral to maintain cell homeostasis, it is thus necessary to systematically analyze the functions of these factors specifically with respect to ribosome assembly. Hence, the comprehensive approach described in this work is so far unique, as it specifically focuses on the role of each of the factors during late 50S assembly and furthermore allows direct comparison of the phenotypes.

4.1.2 Silencing efficacy and operon structure

Interestingly, the analyses revealed that growth defects of the strains varied in severity. While strong effects were observed upon depletion of DbpA, EngA and

ObgE, they were only minor upon RlmE or EngB depletion. Although such variations are generally possible, especially the mild phenotype upon EngB depletion does not quite fit its essentiality. It is possible that the differences are rather due to differing silencing efficacy of the PTasRNAs. Indeed, it was shown that the silencing efficacy of PTasRNAs targeting slightly different positions of the same mRNA can vary. This was hypothesized to be due to mRNA secondary structures that affect the accessibility of PTasRNA[283]. To accurately determine the efficacy of every PTasRNA, protein levels of each of the assembly factors would have to be determined, as inhibition of translation and not mRNA degradation is the primary knock-down mechanism. Thus, microarray analysis and qRT-PCR analyses are insufficient, as expression of PTasRNA does not necessarily lead to a reduction of target mRNA[285]. To enhance the knock-down efficacy, a screening of alternative PTasRNAs is possible. However, as all of the depletion strains exhibited perturbed growth and importantly, also altered ribosomal composition, assembly defects can demonstrably be induced.

Exemplarily, the knock-down efficacy of ObgE depletion was assessed in cells that were cultivated at 25 °C (**Figure A6**, Appendix) by immunoblotting. Similar analyses were conducted to assess the silencing efficacy for PTasRNA constructs against the other factors, but due to their extremely low abundance, their levels could not be determined via immunoblotting. The analyses showed that a rather low efficacy of ~25 % was enough to provoke the severe assembly defects observed upon ObgE depletion. Interestingly, knock-down efficacy was even higher at 37 °C with ObgE levels decreasing by ~50 % (**Figure A6**, Appendix), although the assembly defects as observed by ribosome profile analysis were much milder. Hence, high knock-down efficacy does not guarantee stronger perturbation of assembly. Consequently, growth as well as ribosome profile analyses are necessary to assess

the general consequences of assembly factor depletion under specific stress conditions. However, these analyses emphasize that ObgE indeed is essential to maintain the integrity of ribosome assembly especially at low temperatures.

Another possible consequence of PTasRNA mediated knock-down is that its expression can exhibit polar silencing effects on downstream genes[283,308], causing decreased levels of not only the target protein, but also additional proteins from the same operon. However, such polar effects can also be caused by knock-outs and hence, cannot be completely ruled out when conducting genetic studies. Moreover, most of the assembly factors investigated are encoded by the most promoter-distal gene (**Figure 17**), inherently reducing the risk of such polar effects. Generally, the assembly-specific phenotypes of the depletion strains hence indicate an efficient downregulation of the assembly factors. However, global changes in protein levels upon assembly factor depletion should be analyzed by quantitative mass spectrometry (qMS).

4.1.3 Assembly perturbation leads to strong ribosome-nucleoid segregation and foci formation

The spatial organization of ribosomes throughout bacterial cells has been investigated under varying conditions using fluorescently labeled ribosomal fusion proteins and confocal, as well as super-resolution methods[82,288]. It was found that the treatment with different classes of antibiotics caused distinct redistribution of ribosomal particles in cells[82,288]. Although some studies describe morphological changes in bacteria upon interference with the ribosome assembly process, the distribution of ribosomal particles under these specific stress conditions has never been addressed in detail so far and high-resolution data is scarce. Several studies, however, describe the formation of elongated cells upon ObgE depletion with large expanding nucloids[198,199,208].

To obtain high-resolution data, a fluorescence microscopic method based on 3D-SIM was established that allows the visualization of ribosomal particles and the nucleoid in fluorescently labeled *E. coli*.

This way, the consequences of assembly perturbation upon ObgE depletion could be visualized with high spatial resolution using the reporter strain MGrg*.

The analyses revealed that assembly stress results in the formation of a number of elongated cells with large nucleoids. Moreover, ribosomal particles dramatically redistributed, exhibiting even stronger segregation from the nucleoid with most of them localizing towards the cell poles and along the membrane. Earlier studies suggested that the central region of the toroidal nucleoids contained cytoplasmic inclusions[79,309,310], but interestingly, 3D-SIM images revealed additional information that has not been resolved before. This is most likely due to the higher spatial resolution (xy-direction: ~130 nm for mAzami and 150 nm for mCherry) that can be achieved using this super-resolution technique. Distinct foci of mCherry- and mAzami-specific fluorescence from ribosomal particles were observed within the DAPI-stained nucleoids. Filamentous cells even exhibited multiple of these ribosomal foci within elongated DNA-structures.

A similar phenotype was observed upon the conditional knock-out of *rplC* encoding ribosomal protein uL3. In this case, ribosome-nucleoid-segregation was stronger than in the ObgE depleted cells and more, even larger foci were observed, with the nucleoids forming distinct toroidal shapes, strictly avoiding the ribosomal particles within their center. This agrees with the A_{260} profiles that reveal a more severe assembly defect upon deletion of this early assembly protein.

Although continuous axial nucleoid contraction and strong ribosome-DNA segregation have been described upon long-time exposure of translation inhibitors, this

is the first time that ribosomal foci within the nucleoids could be resolved via fluorescence microscopy. However, very early electron microscopic studies also described such toroidal-shaped nucleoids upon chloramphenicol treatment and thus further corroborate the findings, emphasizing that the foci formation is not artifactual[309,310]. They also observed the formation of chains of multiple toroidal nucleoids resembling the elongated DNA-structures with multiple foci in ObgE depleted cells[310]. These chains are thought to arise due to incomplete chromosome segregation upon completion of replication[310-312]. Indeed, these early studies suggest that ribosomal particles localize to the center of those toroidal nucleoids[310], but in-depth analysis has been missing and is now provided using the fluorescently labeled reporter strains in combination with high-resolution 3D-SIM.

4.1.4 Factors determining the spatial organization of ribosomes and the nucleoid in *E. coli*

In general, the mechanisms by which the cytoplasm is arranged and the nucleoid is formed are not completely understood, but they are proposed to involve balanced compacting and expanding forces, like confinement by the cell envelope or general macromolecular crowding, amongst others[313-315]. 70S ribosomes and polysomes are thought to be generally excluded from penetrating the DNA-mesh[316] due to their mere size and thus mainly localize to the cell poles, where the majority of translation is happening. As the nucleoid is described to be present in a state of intermediate density in normal growing, unperturbed cells, the smaller free ribosomal subunits, however, can penetrate this region and simultaneously represent one of the expanding forces on the nucleoid[289,317]. In general, 10-15 % of ribosomal particles can be found within the nucleoid, where they are thought to engage in co-transcriptional translation[317].

But what causes the severe redistribution and foci formation of ribosomal particles in assembly defective cells that resembles the phenotype observed upon chloramphenicol treatment? Indeed, treatment of cells with translation inhibitors in general (*e.g.* tetracycline, streptomycin) and even stationary phase cells were described to exhibit a similar phenotype, indicating that the redistribution is a general consequence of cessation of global translation[288]. Since assembly and translation are tightly coupled, it is conceivable that the same mechanisms cause their similar morphological phenotypes.

Generally, ribosome-nucleoid segregation, even in normal growing cells, is thought to be caused by "excluded volume effects" and the "maximal total entropy" of the DNA-ribosome system[83,318]. According to this theory, the DNA is hypothesized to localize to the center of the cell avoiding the walls as this positioning allows maximum conformational entropy, while the ribosomes occupy the excluded volume to maximize translational entropy[83]. Correspondingly, it is known that additional ribosome-rich regions appear in the cell center when the two major nucleoid lobes are built before cell division in log phase cells[288,289], indicating that the mere additional space within the nucleoid region allows ribosomes to diffuse towards the cell center. Hence, it is possible that spatial confinement is not only the reason for general ribosome-nucleoid segregation, but also for the formation of foci. As ObgE depleted cells were described to exhibit polyploid DNA content[198], it is indeed conceivable that ribosomal particles are entrapped within the toroidal-shaped nucleoid due to spatial limitations.

In agreement with the entropy-based theory, it is hypothesized that the general decrease of free ribosomal subunits (*e.g.* upon chloramphenicol treatment) reduces the expanding force within the DNA mesh and thus enhances a compaction of the nucleoid[318]. Moreover, co-transcriptionally translating ribosomes are thought to be

released from the nucleoid, as soon as transcription is completed[318], further enhancing the relaxation of the nucleoid into a fully condensed state causing even stronger compaction and consequently even an exclusion of free ribosomal subunits from the dense DNA-mesh[289,317,318]. Although ribosome assembly rather causes an accumulation of free subunits and subunit precursors than a conversion into 70S ribosomes and polysomes, it is conceivable that the perturbation of transcriptional and translational processes leads to a similar phenotype.

Interestingly, microscopic analyses using a reporter strain producing a fluorescently labeled early and a labeled late assembly protein of the large ribosomal subunit suggest that both immature pre-50S and mature 50S particles show the same distribution pattern, occupying both the polar regions and the region enclosed by the toroidal nucleoid. Hence, it is conceivable that the foci formation results from accumulated ribosomal precursors and subunits that simply remain trapped within the cell center where they are normally synthesized. Hence, foci formation could thus be a direct measure to determine the integrity of ribosome assembly.

Another possibility is that the fluorescence signal within the foci stems from free ribosomal proteins that cannot be incorporated into ribosomal particles upon assembly perturbation. However, the ribosomal proteins uS15 and uL1 are known to be feedback-regulated by autogenous control[319,320] and ribosome profile analysis shows that the amounts of both proteins in the soluble fractions are comparably low. Hence, it is more likely that the fluorescence signal indeed stems from proteins that are already incorporated into the respective subunit.

4.1.5 Colocalization of assembly factors with ribosomal particles

In normal growing cells, assembly factors can be assumed to be found in the vicinity of the 10-15 % of ribosomal particles that localize within the nucleoid region, as this is where ribosome assembly takes place. Previously, the cellular localization

of ObgE was followed by immunofluorescence using anti-ObgE[198]. Yet, it was found to mainly avoid the nucleoid region, indicating that it primarily acts as a cytoplasmic protein. However, ObgE is generally proposed to be involved in numerous cellular processes[321] and the number of ObgE proteins specifically dedicated to ribosome assembly in rapidly growing *E. coli* is likely to be very small. Another study described the fluorescence imaging of EngB[322] and also found that it distributed evenly throughout the cytoplasm. Yet, the spatial resolution achieved in this study is presumably quite low, with the DAPI staining spreading evenly throughout the cell, occupying the entire space, although the nucleoid is known to exhibit distinct sub-structures and preferably localizes to the cell center (see **Figure 22**).

Generally, the low abundance of assembly factors severely complicates colocalization studies (typically ~40-times less than ribosomal proteins[299]) and the resolution and sensitivity achieved by 3D-SIM was indeed not high enough to obtain reliable information on the distribution of ObgE-mCherry.

One possible approach to enhance the resolution would be to employ single-molecule localization techniques like PALM or STORM. However, these methods require special photoactivatable or photoswitchable fluorescent proteins to obtain the optimal results[323]. The design of an additional strain with alternative fluorescent proteins can be circumvented using DNA-PAINT (DNA Point Accumulation for Imaging in Nanoscale Topography)[324]. This technique generally applies primary antibodies that associate with the protein of interest and bind to secondary antibodies that carry one or more so-called "docking strands" (single stranded DNA oligonucleotides)[325]. The specimen is then incubated with a solution of complementary "imager strands" that bear a fluorophore that is used for imaging. Due to thermal fluctuations, imager strands constantly bind and unbind docking strands, resulting in "blinking" fluorescence detection events, with the solution

providing a constant exchange of new imager strands[326]. In the end, these events can then be reconstructed to obtain super-resolution images with resolutions down to 10 nm within cells[325,327]. Instead of using antibodies specific for the protein of interest which are often not easily available, nanobodies against fluorescent proteins can be used for DNA-PAINT[327,328]. This indirect visualization of FPs using imager strands that are coupled to organic dyes provides higher spatial resolution and sensitivity due to the photophysical properties of the dye and the single-molecule based approach in general[328].

This technique is thus the most promising approach to study the distribution of ribosomal precursors and assembly factors simultaneously and importantly, the fluorescently labeled reporter strains can be used for these analyses.

4.1.6 Multiple gene-silencing of assembly factors

Genetic approaches have been employed to determine possible functional relationships between different assembly factors. For example, overexpression of the GTPases ObgE or EngA was found to rescue the severe growth defect and restore impaired ribosome assembly in *rlmE* null mutants[210]. Moreover, RlmE was described to accumulate in immature 50S particles that are formed in an ObgE mutant strain[207], suggesting a direct link between the three factors.

The generation of knock-out mutants in *E. coli* to determine synthetic interactions between different factors is often problematic, especially when the specific factor of interest is essential for growth, as it is the case for the GTPases EngA, EngB and ObgE. Despite considerable efforts, it was not possible to generate a conditional *ΔobgE* knock-out strain using λ-red recombineering and data obtained from published *ΔobgE* knock-out mutants[199] was inconclusive (data not shown). Thus, the RNA-based antisense approach appears to be the most feasible and reliable strategy to achieve depletion of ObgE.

In addition, the conditional knock-down strategy that was used for single-factor depletions (see **3.1**) is ideally suited to achieve multiple-gene silencing, as three different PTasRNA expression vectors (pHN678, pHN1009 and pHN1257) are available for gene silencing (**Figure 37**). These vectors are possess IPTG-inducible promoters, but harbor different ORIs and resistance cassettes, which allows co-transformation in any desired combination[329].

Figure 37: Scheme of vector backbones suitable for multiple-gene silencing of assembly factors. Backbones contain combinable ORIs (green; pBR322, pSC101^{H} and paCYC) and resistance cassettes for individual antibiotics: Ampicillin (Amp^{R}, red), Kanamycin (Kan^{R}, blue) and Chloramphenicol (Cam^{R}, purple). asRNA coding sequence ("asDNA") of interest was cloned into each vector backbone via restriction cloning. Inverted repeats coding for paired termini (PT) are indicated as white segments.

As growth perturbation upon PTasRNA expression against assembly factors was achieved independent of the vector backbone (**Figure A2**, Appendix), these can now be used for multiple gene silencing to determine possible functional relationships between the five factors. Preliminary analyses have been conducted by double gene-silencing of ObgE and DbpA at the same time and as expected, additive effects on growth were observed at all temperatures tested (**Figure A9, Appendix**).

Interestingly, growth of the double mutant was almost completely abolished at 42 °C, while the single mutant exhibited only minor growth perturbation, indicating a functional relationship between DbpA and ObgE. However, further in-depth

analyses are necessary to corroborate such findings. For example, precursor particles isolated from such depletion strains could be isolated and their composition could be analyzed and compared to particles accumulating in the single-depletion strains.

4.2 High-throughput screening for *in vivo* detection of subunit assembly defects in *E. coli*

The fluorescently labeled reporter strain MGrg was employed to screen 307 small molecules for their effect on growth and the ratio of ribosomal subunit to specifically detect assembly inhibitors. Compounds that lead both to a significant alteration of the fluorescence ratio and inhibition of bacterial growth can now be further validated. However, multidimensional evaluation of the high-throughput data, like multidimensional scaling (visualization of the level of similarities/dissimilarities between data sets) and hierarchical clustering, will be necessary to find the most promising lead compounds by assigning functional relationships. Furthermore, so-called Pan-assay interference compounds (PAINS) which tend to react nonspecifically with a variety of biological targets and other compounds that give false positive results (*e.g.* due to auto-fluorescence) have to be identified and carefully evaluated.

Lead compounds will then be reexamined using the same fluorescence-based *in vivo* assay to obtain a series of dose-response relationships that allow the calculation of the respective IC_{50}. Effects on assembly will be evaluated with appropriate drug concentrations by ribosome profile analysis and fluorescence microscopy using the fluorescently labeled reporter strains. However, further analyses like microscale thermophoresis (MST) or pull-down assays are necessary to identify the specific target of the chemical probe.

Another possibility to identify specific inhibitors of assembly includes structure-

based drug design. Especially the structural information of the pre-50S•ObgE-StrepII complex, as well as additional data from precursors that will be obtained from the other knock-in and knock-down strains provided in this work can serve as a basis for structure-based design of small molecule inhibitors.

Moreover, the screening approach can readily be used to screen knock-out or knock-down libraries to detect novel factors involved in ribosome assembly.

4.3 Structural analysis of native pre-50S particles via assembly factors as bait

In addition to multiple-gene silencing studies, structural data of precursor particles can reveal spatial relationships or overlapping binding sites of different factors and thus provide insight into how the different steps of assembly at different construction sites are synchronized (see **4.3.2**). Hence, the structural analysis of 50S precursors via assembly factors as bait is presumably the method of choice to obtain information on such functional interactions. Moreover, this approach eliminates the risk of investigating off-pathway particles that are products of perturbations or pleiotropic effects.

4.3.1 Design of endogenously StrepII-tagged factors for the purification of native pre-50S particles

Multiple studies describe the use of affinity-tagged assembly factors as bait to purify native ribosomal precursors in yeast[330,331]. However, this technique has not been successfully transferred to prokaryotes so far. As *E. coli* does not allow efficient recombination of exogenous linear DNA fragments into its chromosome, λ-red recombineering was used to generate endogenously StrepII-tagged versions of the assembly factors of interest. Importantly, all of the strains were phenotypically validated with respect to cell growth and integrity of ribosome assembly. Hence, they now offer a toolbox for the purification of native pre-50S complexes.

4.3.2 Proof of principle: Purification of authentic pre-50S•ObgE-StrepII complexes

To provide proof of principle, pre-50S•ObgE-StrepII complexes were purified from rapidly growing *E. coli* cultures and indeed could be isolated in sufficient amounts for subsequent structural and biochemical analyses. Although structural data of assembly factors in complex with ribosomal particles is already available, these previous studies relied on the reconstruction of complexes *in vitro* from purified, mature subunits in combination with recombinant assembly factors in the presence of GMP-PNP, as described for EngA and ObgE[167,169]. Albeit they can provide initial insight into the interactions of the respective factor with a 50S subunit, they do not describe the interaction with its actual substrate, which is a precursor particle. Hence, understanding of the actual maturation processes is limited.

Thus, the structural analysis of authentic pre-50S complexes purified by ObgE-StrepII provides a first insight into how these precursor particles mature into functional subunits *in vivo*. This successful purification strategy can now be transferred to the whole subset of 50S assembly factors that participate in the maturation of the functional core using the generated reporter strains. Additionally, the assembly factors that were found to facilitate the maturation of the 50S interface (Yjga, RluD and and RsfS) and act in a concerted fashion with ObgE, can also be used to isolate pre-50S particles in related stages of late 50S maturation.

4.3.3 Role of ObgE during functional core formation

The analysis of authentic purified pre-50S•ObgE-StrepII complexes yielded a high resolution cryo-EM reconstruction and hence provided detailed insight into the composition and conformation of the functional core and adjacent regions during 50S formation. Especially interesting is the structural relationship of ObgE with the

functional core proteins uL16 and bL36. The structural data suggests that the simultaneous presence of ObgE with a mature positioning of both proteins is precluded and indeed, the absence of either protein resulted in increased ObgE occupancy on pre-50S particles. This indicates that a fully mature functional core acts as a signal for ObgE dissociation. Hence, ObgE presumably fulfils a gatekeeper function.

Further analyses to dissect the functional role of ObgE during 50S formation involve the mutation of ObgE residues that were found to specifically interact with helices of the functional core to dissect the structural signals that trigger GTPase activity and hence ObgE dissociation. Moreover, pre-50S particles affinity-purified in complex with other assembly factors could provide further insight into the importance of ObgE, as different intermediate states can be assumed capture different states of ObgE interaction. Additionally, the knock-down mutants provide a large range of precursor particles that can be isolated and analyzed in detail structurally.

In general, this study provides a useful toolbox that can be employed for further in-depth analysis of late 50S maturation. The combination of systematic genetic studies using assembly factor depletion in combination with the purification of authentic *in vivo* intermediates will allow a characterization of key steps during 50S formation and provide deepening mechanistic insights into the dynamic process of late 50S assembly.

5. Material and methods

5.1 Chemicals, material and instruments

5.1.1 Chemicals

Table 1: Chemicals

Common chemicals were ordered from Sigma-Aldrich, Merck or Carl Roth, respectively. All additional chemicals are listed below.

Chemicals	Supplier
Acrylamide	Carl Roth GmbH & Co.KG
Ammonium chloride	Riedel-de Haën AG
Ammonium persulfate (APS)	Carl Roth GmbH & Co.KG
Ampicillin	AppliChem, USA
Bacto™ agar	Becton, Dickinson and Company, USA
Bacto™ peptone	Becton, Dickinson and Company, USA
Bacto ™ tryptone	Becton, Dickinson and Company, USA
Bacto ™ yeast extract	Becton, Dickinson and Company, USA
Bicinchoninic acid (BCA)	Sigma-Aldrich Chemistry GmbH
Bradford reagent (5x)	Bio-Rad Laboratories GmbH
Bromphenol blue	SERVA Electrophoresis GmbH
Chloramphenicol	SERVA Electrophoresis GmbH
Complete EDTA-free protease inhibitor cocktail (TM complete)	Roche Dagnostics GmbH
4'6-diamidine-2-phenylindole (DAPI)	Sigma-Aldrich Chemistry GmbH
Deoxyribonucleotidetriphosphase (dNTPs)	New England Biolabs, USA
Dimethyl sulfoxide	Carl Roth GmbH & Co.KG
Dithiothreitol (DTT)	Carl Roth GmbH & Co.KG
EDTA	Carl Roth GmbH & Co.KG
Glucose	Carl Roth GmbH & Co.KG
Glycerol	VWR International GmbH
Hydrogen peroxide	Sigma-Aldrich Chemistry GmbH
Isopropyl-β-D-1-thiogalactopyranoside (IPTG)	Carl Roth GmbH & Co.KG

Isopropyl alcohol	Fisher Scientific
Kanamycin	Carl Roth GmbH & Co.KG
LB medium	Carl Roth GmbH & Co.KG
Midori Green	NIPPON Genetics EUROPE GmbH
Monopotassium phosphate	Sigma-Aldrich Chemistry GmbH
β-Mercaptoethanol	Merck
Magnesium chloride	Acros Organics, USA
Magnesium sulfate	Riedel-de Haën AG
NcoI-HF restriction enzyme	New England Biolabs, USA
4 % Paraformaldehyde in PBS	Boster Bio, USA
Potassium chloride	Acros Organics, USA
FastAP Phosphatase	ThermoFisher Scientific, USA
Rifampicin	Sigma-Aldrich Chemistry GmbH
Sodium azide	Merck
Sodium chloride	VWR International GmbH
Sodium dodecyl sulfate (SDS)	Carl Roth GmbH & Co.KG
Sucrose	Carl Roth GmbH & Co.KG
T4-Ligase	New England Biolabs, USA
Tetramethylendiamine (TEMED)	Carl Roth GmbH & Co.KG
Tris base (2-amino-2-hydroxymethyl-propane-1,3-diol) (	Carl Roth GmbH & Co.KG
Tween 20	Carl Roth GmbH & Co.KG
XhoI restriction enzyme	New England Biolabs, USA

5.1.2 Buffer and solutions

Table 2: Buffer and solutions

Buffer/Solution	Composition/Supplier
BCA working solution	bicinchoninic acid solution with 0.08 % (w/v) $CuSO_4$
TAE buffer	2 M Tris-HCl pH 8.0 1 M acetic acid 50 mM EDTA
6x DNA loading dye	30 % (w/v) glycerol

	0.25 % (w/v) bromphenol blue $_{dd}H_2O$
T4 DNA-ligase buffer (10x)	ThermoFisher Scientific, USA
Thermo-Pol reaction buffer (Taq-DNA polymerase buffer, 10x)	New England Biolabs GmbH, USA
Phusion reaction buffer (10x)	100 mM Tris-HCL pH 8.8 500 mM KCl 20 mM MgCl 1 % (v/v) Triton X-100
CutSmart buffer (10x)	New England Biolabs GmbH, USA
Antarctic Phosphatase buffer (10x)	New England Biolabs GmbH, USA
BCA working solution	Bicinchoninic acid solution with 0.08 % (w/v) $CuSO_4$
1x SDS running buffer	25 mM Tris 200 mM glycerol 1 % (w/v) SDS
5x SDS sample buffer	255 mM Tris-HCl pH 6.8 5 % SDS 715 mM β-mercaptoethanol 42.5 % glycerol 0.35 % (w/v) bromphenol blue
SDS Separation gel buffer	1.5M Tris-HCl pH 8.8 0.4 % (w/v) SDS
Separation gel (13 %)	10 ml separation gel buffer 17.2 ml acrylamide 12.6 ml H_2O 40 µl TEMED 200 µl APS (10 % w/v)
SDS Stacking gel buffer	0.5 M Tris-HCl pH 6.8 0.4 % (w/v) SDS
Stacking gel	3 ml stacking gel buffer 1.3 ml acrylamide 7.8 ml H_2O 20 µl TEMED 100 µl APS (10 % w/v)
Bis-Tris gel buffer (3.5x)	1.25 mM Bis-Tris Hcl pH 6.5
MOPS running buffer (5x)	250 mM MOPS

	250 mM Tris base 5 mM EDTA 0.5 % SDS
TAE buffer (50x)	2 M Tris-HCl pH 8.0 1 M acetic acid 50 mM EDTA
TBS-T	20 mM Tris-HCl pH 8.0 137 mM NaCl 0.1 % (v/v) Tween-20
1x Western blot transfer buffer	25 mM Tris 190 mM glycine 0.35 mM SDS 20 % (v/v) methanol
Enhanced chemiluminiscence solution (ECL)	Solution A: 0.1 M Tris-HCl pH 8.6 25 mg luminol ad. 100 ml $_{dd}H_2O$ Solution B: 11 mg p-hydroxycoumaric acid ad. 10 ml DMSO Solution C: H_2O_2 (30 %) Mixing ratio: 1 ml sol. A + 100 µl sol. B + 1 µl sol. C
Buffer A	10 mM Tris-HCl pH 7.5 10 mM $MgCl_2$ 100 mM NH_4Cl 250 µg/ml chloramphenicol
Gradient buffer 10 %/25 %/40 %	Buffer A 10 %/25 %/40 % (w/v) sucrose 0.5 mM DTT 1x TM Complete
Lysis buffer	Buffer A 0.5 mM DTT 1 mM PMSF 1x TM Complete 250 µg/ml Chloramphenicol

5.1.3 Antibodies

Table 3: Antibodies

Antibody	Supplier/Source
bL19, uL1 and uS2 specific sheep antibodies uS15 specific rabbit antibody	Dr. Knud Nierhaus
Monoclonal anti-FLAG M2 antibody	Sigma (F1084)
Strep-Tactin-HRP conjugate	IBA (2-1502-001)
Peroxidase conjugated rabbit anti-sheep antibody	Dianova GmbH (313-035-003)
Peroxidase conjugated donkey anti-rabbit antibody	Dianova GmbH (711-035-151)
Peroxidase conjugated donkey anti-mouse antibody	Dianova GmbH (715-035-151)

5.1.4 DNA and protein markers

Table 4: DNA and protein markers

DNA marker	Supplier
GeneRuler 1 kb DNA ladder	Fermentas, St. Leon-Rot
BlueStar Prestained Protein Marker	Fermentas, St. Leon-Rot

5.1.5 Molecular biology kits

Table 5: Molecular biology kits

Kit	Supplier
QIAprep Spin Miniprep Kit	Qiagen
QIAprep Gel Extraction Kit	Qiagen
DNA-spin™ Plasmid DNA Purification Kit	iNtRON Biotechnology, Korea

PierceTM BCA Protein Assay Kit	Thermo Scientific, USA

5.1.6 Software

Table 6: Software

Software	Provider
Chimera X	Wayne Rasband (National Institutes of Health)
Fiji (ImageJ)	Wayne Rasband (National Institutes of Health)
PyMol 2.3	Schrödinger, LLC
PeakTrak V1.1	Teledyne Isco, Inc.
Prism für macOS (Version 8.0.1)	GraphPad Software, Inc.
SnapGene, Version 3.2.1	GSL Biotech LLC, Chicago

5.1.7 Culture media

Table 7: Culture media

Culture medium	Composition
Lysogeny broth liquid medium (LB medium)	0.5 % (w/v) Bacto ™Yeast Extract 1 % (w/v) Bacto ™ Tryptone 0.5 % (w/v) NaCl
Concentration of added antibiotics/substances:	
Ampicillin	100 µg/ml
Chloramphenicol	25 µg/ml
Kanamycin	50 µg/ml
IPTG	1 mM
LB plates	0.5 % (w/v) Bacto ™ Yeast Extract 1 % (w/v) Bacto ™ Tryptone 0.5 % (w/v) NaCl 1.5 % Bacto™ Agar
Concentration of added substances:	
Ampicillin	100 µg/ml
Kanamycin	50 µg/ml
IPTG	1 mM
5x M9 Salts	64 g $Na_2HPO_4 \cdot 7H_2O$

	15 g KH_2PO_4 2.5 g NaCl 5 g NH_4Cl ad. 1000 ml $_{dd}H_2O$
M9 minimal medium	1 x M9 salts 2 mM $MgSO_4$ 0.1 mM $CaCl_2$ 0.4 % glucose

5.1.8 Expendable materials

Table 8: Expendable materials

Expendable materials	Supplier
Centrifuge tubes 12 ml	Seton Scientific, USA
Centrifuge tubes, 1 ml	Beckman Coulter, USA
Electroporation cuvettes (2 mm gap)	Peqlab Biotechnologie GmbH
Falcon™ tubes (15 ml)	Sarstedt
Falcon™ tubes (50 ml)	Sarstedt
Screw-cap tubes 2.0 ml	Alpha laboratories
Glass beads, 0.25-0.5 mm	Carl Roth GmbH & Co.KG
High precision cover glasses 18x19 mm (thickness No. 1.5H (170 µm ± 5 µM)	Paul Marienfeld GmbH and Co. KG
Imaging Spacer 20 mm x 2 mm	Electron Microscopy Sciences, GB
Micro reaction tube (1.5 and 2 ml)	Eppendorf AG
Microplate, PS, 96 well, F-bottom, black	Greiner Bio-One
Microplate, PS, 384 well, black, clear bottom	Corning, Glendale, USA
Microscope slides ECN 631-1550	VWR
Quartz cuvette, layer thickness: 10 mm	Hellma
Semi-Micro-cuvettes	Greiner Bio-One
Whatman® Protran® Nitrocellu-lose Transfer Membrane	GE HEalthcare, USA

5.1.9 Instruments

Table 9: Instruments

Instrument	Model	Manufacterer
Centrifuges	Avanti J-265 XPI, rotor JLA-10.500	Beckman Coulter, USA
	Multifuge 4KR (rotor LH400)	Heraeus
	Cryofuge 8500i	Heraeus
Confocal fluorescence microscope	Leica TCS SP8	Leica Microsystems, Switzerland
Electroporation system	Bio-Rad Gene Pulser Electroporation System	Bio-Rad Laboratories GmbH, USA
Fractionator	Gradient Former Model 160	Teledyne ISCO, USA
Gradient mixer	Gradient Master 107	BioComp Instruments, Inc., Canada
Homogenisator	FastPrep®-24	MP Biomedicals Germany GmbH
Incubator	Infors Multitron II	Infors GmbH
	MaxQ 8000	Thermo Scientific, USA
Luminescent Image Analyzer	LAS3000	Fujifilm
Photometer (UV/Vis)	Ultraspec 3100 pro,	GE Healthcare, GB
	Nano Vue™ Plus,	GE Healthcare, GB
	NanoPhotometer NP80	Implen GmbH
Microplate reader	Infinite F500	Tecan Group Ltd., Switzerland
Super-resolution microscope	GE DeltaVision OMXv4 Blaze	GE Healthcare, GB
Thermal cycler	iCycler	Bio-Rad Laboratories GmbH
	TAdvanced Thermal Cycler	Analytik Jena AG
Thermal shaker	ThermoMixer C	Eppendorf AG, Hamburg
Tabletop centrifuges	Pico 21 Microcentrifuge, rotor 24 x 1.5/2.0 ml	Heraeus
	Centrifuge 5427 R, rotor F45-48-11	Eppendorf AG
Ultracentrifuges	Optima L-90K (Beckman rotor SW-41 Ti)	Beckman Coulter, USA
	Optima LE-80K (Beckman rotor SW-41 Ti)	Beckman Coulter, USA

	Discovery M150SE Micro-ultracentrifuge (rotor S140 AT)	Thermo Scientific, USA
Vortexer	Vortex Genie 2	Scientific Industries, USA
Water bath shaker	Classic Series C76 Water Bath Shaker	New Brunswick, USA

5.1.10 Strains

Table 10: Strains

Name	Genotype	Reference/Source
DH5αZI	F- Φ80lacZΔM15 Δ(lacZYA-argF) U169 recA1 endA1 hsdR17(rk-, mk+) phoA supE44 thi-1 gyrA96 relA1 λ-	Invitrogen
DY330	W3110 ΔlacU169 gal490 λcI857 Δ (cro-bioA)	Yu et al., 2000[332]
MC4100	F- [araD139]B/r Δ(argF-lac)169* &lambda- e14- flhD5301 Δ(fruK-yeiR)725 (fruA25)‡ relA1 rpsL150(strR) rbsR22 Δ(fimB-fimE)632(::IS1) deoC1	Casadaban, 1967[333]
MCΔlC	MC4100 *ΔrplC* pTRC-*rplC*	Nikolay et al., 2015[293]
MCrg*	MC4100 *rpsO-mcherry rplA-mazami*	Nikolay et al., 2015[293]
MCrg*ΔlC	MC4100 *rpsO-mcherry rplA-mazami ΔrplC* pTRC-*rplC*	Nikolay et al., 2015[293]
MGrg*	MG1655 *rpsO-mcherry rplA-mazami*	this work
MG1655 *ObgE*-3xFLAG	MG1655 *obgE-3xflag*	this work
MG1655 DbpA-StrepII	MG1655 *dbpA-strepII*	this work
MG1655 EngA-StrepII	MG1655 *engA-strepII*	this work
MG1655 EngB-StrepII	MG1655 *engB-strepII*	this work
MG1655 ObgE-StrepII	MG1655 *obgE-strepII*	this work
MG1655 RlmE-StrepII	MG1655 *rlmE-strepII*	this work
MG1655 uL1-mAzami ObgE-mCherry	MG1655 *rplA-mAzami obgE-mCherry*	this work
MG1655 uL1-mAzami ObgE-mCherry Δrpmj	MG1655 *rplA-mAzami obgE-mCherry Δrpmj*	this work
MCrgLΔlC	MC4100 *rplA-mcherry rplS-mazami ΔrplC* pTRC-*rplC*	Nikolay et al., 2016[290]

5.1.11 Primers

Table 11: Primers

Gene	Name	Sequence
dbpA	5′ *dbpA-strepII* KI	ggcgggaagattaaaggaaaaacgtgccgggtgcggt-tattaaatggtcccatcctcagttt-gaaaaataagtgtaggctggagctgcttc
	3′ *dbpA* KI	gcaatcccgaataagatgtttactcttgcacccggcaattcaacattt-caatgaatatcctccttagttc
engA	5′ *engA-strepII* KI	atgcgtaaacgtaagcgtctgatgaagcacatca-agaaaaataaatggtcccatcctcagtt-tgaaaaataagtgtaggctggagctgcttc
	3′ *engA* KI	attccctctacattcatagagggaatggcagataaaatacttacg-gataaatgaatatcctccttagttc
engB	5′ *engB-strepII* KI	tggtttagcgagatgcagcctgtagaagaaacgcag-gacggcgaatggtcccatcctcagtt-tgaaaaataagtgtaggctggagctgcttc
	3′ *engB* KI	atttacgggccg-gatacgccacatccggcacaagcattaaggcaagaaaaatgaa-tatcctccttagttc
obgE	5′ *obgE-strepII* KI	tgggacgaagacgacgaagaaggcgttgagttcattta-caagcgttggtcccatcctcagtt-tgaaaaataagtgtaggctggagctgcttc
	5′ *obgE-3xflag* KI	tgggacgaagacgacgaagaaggcgttgagttcattta-caagcgtgattacaaggatgat-gacgacaaggattacaaggatgatgacgacaaggattacaagga tgatgacgacaagtaagtgtaggctggagctgcttc
	3′ *obgE* KI	ggcctgataagcgtagcgcatcaggctgatttggcgtttatcatca-gtgaatgaatatcctccttagttc
rlmE	5′ *rlmE-strepII* KI	gcacgttcgcgggaagtgtatattgtagcgaccgggcgtaaac-cctggtcccatcctcagtt-tgaaaaataagtgtaggctggagctgcttc
	3′ *rlmE* KI	aggatactctatatccagcatctttcaaactttcgtct-gaaatctcccggatgaatatcctccttagttc
obgE	5′ *obgE-mCherry* KI	acgactgggacgaagacgacgaagaaggcgttgagttcattta-caagcgtgggacgtcgggtggaagc
	3′ *obgE mCherry* KI	ggcctgataagcgtagcgcatcaggctgatttggcgtttatcatca-gtgaatgaatatcctccttagttc
rpmJ	5′ *rpmJ-KO*	ctaatctagccagctcaacccaactttgcaagaaaaa-tatgcgaaaaaaatgaatatcctccttagttc
	3′ *rpmJ-KO*	gaaaggctacggccgataattggtcgcccgagaagttacgga-gagtaaaagtgtaggctggagctgcttc

dbpA	5‘ *dbpA*as	ccgctcgaggtgaccgctttttctaccctg
	3‘ *dbpA*as	catgccatgggcatcaatttgctgtaacaag
engA	5‘ *engA*as	ccgctcgaggaggctttaaacatggtacc
	3‘ *engA*as	catgccatggcgtacttacggtcacgagtc
engB	5‘ *engB*as	ccgctcgagttgactaatttgaattatcaac
	3‘ *engB*as	catgccatggaggttgataagctgggtgcg
obgE	5‘ *obgE*as$_1$	ccgctcgagatgaagtttgttgatgaagca
	3‘ *obgE*as$_1$	catgccatgggcacggaaagatttttcaaaacg
	5‘ *obgE*as$_2$	caccctcgagccgcgcaggcgaatgatttacggag
	3‘ *obgE*as$_2$	actgccatgggctcacgcaaccattaccgccatc
rlmE	5‘ *rlmE*as	ccgctcgagatgacaggtaagaagcgttct
	3‘ *rlmE*as	atgccatggtgtgaccaaccacccggagc
rplP	5‘ *rplP*as	ccgctcgagatgttacaaccaaagcgtac
	3‘ *rplP*as	catgccatggacacggatccagatcttacc
dbpA	5’ *dbpA* upstream	tatttgcaaattcctgtccc
	3’ *dbpA* downstream	gcgtgctggcagccagaaga
engA	5’ *engA* upstream	ttccagactgaaccggttgc
	3’ *engA* downstream	acacctgcaacggttgatgg
engB	5’ *engB* upstream	gcaattcactgatttatata
	3’ *engB* downstream	ccttttacttcacgtaatcg
obgE	5’ *obgE* upstream	actggcctggcccgatttct
	3’ *obgE* downstream	agtcaaaaagaaaccccggc
rlmE	5’ *rlmE* upstream	gccaagcagaacaactggct
	3’ *rlmE* downstream	atccaccttacggccattag
rpmE	5’ *rpme* upstream	catcctgacttgaaattcgg
	3’ rpme downstream	cacaagttcaggcaaagctc
rpmI	5’ *rpmI* upstream	cgtgaaagacgatttgcaag
	3’ *rpmI* downstream	ggtcacggtaagcatactga
rpmJ	5’ *rpmJ* upstream	ggagttcatgcgtgatgcaa
	3’ *rpmJ* downstream	gcgattacggcatgcttatg

5.1.12 Plasmids

Table 12: Plasmids

Name	Description	Reference
pCP20	9400 bp; Flp protein encoding; ampicillin and chloramphenicol resistance cassettes	Cherepanov and Wackernagel, 1995[334]

pKD4	3267bp; ampicillin and kanamycin resistance cassette; FRT sites for Flp based cassette removal	Datsenko and Wanner, 2000[335]
pHN678	4043 bp; lacI repressor encoding; chloramphenicol resistance cassette	Nakashima et al., 2012[283]
pHN1009	4086 bp; lacI repressor encoding; ampicillin resistance cassette	Nakashima et al., 2012[283]
pHN1257	4073 bp; lacI repressor encoding; kanamycin resistance cassette	Nakashima et al., 2012[283]
pHN1009-DbpAas	derived from pHN1009; expressing *dbpA*-specific PTasRNA	this work
pHN1009-EngAas	derived from pHN1009; expressing *engA*-specific PTasRNA	this work
pHN1009-EngBas	derived from pHN1009; expressing *engB*-specific PTasRNA	this work
pHN1009-ObgEas_1	derived from pHN1009; expressing *obgE*-specific PTasRNA (primers 5‘ *obgE*as$_2$ and 3‘ *obgE*as$_1$ were used for generation of PTasRNA expressing construct)	this work
pHN1009-ObgEas_2	derived from pHN1009; expressing *obgE*-specific PTasRNA (primers 5‘ *obgE*as$_2$ and 3‘ *obgE*as$_2$ were used for generation of PTasRNA expressing construct)	this work, designed according to Verstraeten et al.[285]
pHN1009-RlmEas	derived from pHN1009; expressing *rlmE*-specific PTasRNA	this work
pHN1257-DbpAas	derived from pHN1257; expressing *dbpA*-specific PTasRNA	this work
pHN1257-EngAas	derived from pHN1257; expressing *engA*-specific PTasRNA	this work
pHN1257-EngAas	derived from pHN1257; expressing *engB*-specific PTasRNA	this work
pHN1257-ObgEas	derived from pHN1257; expressing *obgE*-specific PTasRNA	this work
pHN1257-RlmEas	derived from pHN1257; expressing *rlmE*-specific PTasRNA	this work
pHN687-DbpAas	derived from pHN687; expressing *dbpA*-specific PTasRNA	this work
pHN687-EngAas	derived from pHN687; expressing *engA*-specific PTasRNA	this work
pHN687-EngBas	derived from pHN687; expressing *engB*-specific PTasRNA	this work

pHN687-ObgEas	derived from pHN1009; expressing *obgE*-specific PTasRNA	this work
pHN687-RlmEas	derived from pHN687; expressing *rlmE*-specific PTasRNA	this work

5.2 Methods

5.2.1 Plasmid DNA isolation

Plasmid DNA from liquid *E. coli* culture was isolated using a commercial DNA-spin™ Plasmid DNA Purification Kit (iNtRON) according to the manufacturer's instructions. DNA concentration was determined photometrically at an absorbance of 260 nm using a photometer (Nano Vue™ Plus, GE Healthcare or Nano-Photometer NP80, Implen).

5.2.2 PCR and colony-PCR

Polymerase chain reaction was employed to amplify specific DNA fragments of interest. Sequences for λ Red Recombineering were generated using Phusion DNA-Polymerase. 50 µl PCR reaction mixtures were prepared as follows: 100 ng of DNA template were mixed with 200 µM dNTP mix (10 mM stock), 0.4 µM of forward and reverse primer (10 µM stock), 1x Phusion buffer and 0.5 µl Phusion DNA-Polymerase ad. 50 µl of $_{dd}H_2O$. Conditions for PCR reactions using Phusion DNA-Polymerase are listed in table 13.

Table 13: Cycling conditions for PCR reactions using Phusion DNA-Polymerase

Amplification Step	Cycle(s)	Temperature	Time
Initial Denaturation	1x	98 °C	2 min
Denaturation		98 °C	30 s
Annealing	35x	55 °C	30 s
Elongation		72 °C	60 s

Final Elongation	1x	72 °C	10 min
Cooling down	1x	15 °C	∞

Tag DNA-polymerase was used for colony-PCR. PCR reactions were prepared as follows: material of one single colony was picked from an agar plate using a sterile toothpick. It was dipped into a reaction tube containing 40 µl of $_{dd}H_2O$ until the solution became turbid. 200 µM dNTP mix (10 mM stock), 0.4 µM of each primer (forward and reverse, 10 µM stock), 5 µl 10x ThermoPol® reaction buffer and 0.5 µl Taq Polymerase were added. PCR conditions are listed in table 14.

Table 14: Cycling conditions for PCR reactions using Taq-Polymerase

Amplification Step	Cycle(s)	Temperature	Time
Initial Denaturation	1x	95 °C	5 min
Denaturation		95 °C	30 s
Annealing	35x	55 °C	30 s
Elongation		68 °C	2 min
Final Elongation	1x	68 °C	10 min
Cooling down	1x	15 °C	∞

5.2.3 Agarose gel electrophoresis and gelextraction

DNA fragments of interest were separated by agarose gel electrophoresis. 1 % (w/v) of agarose was dissolved in 1x TAE buffer to prepare 1 % gels. The gels were supplemented with Midori Green Nucleic Acid Staining Solution for visualization of DNA using a UV light imaging system. Samples were mixed in a 5:1 ratio with 6x loading dye and loaded onto the gel. Separation was performed at a current of 120 V in 1x TAE buffer. A 1 kb DNA ladder (Fermentas) was used to determine the fragment size. DNA fragments of the appropriate size were excised from the gel

and purified using the DNA QIAquick Gel Extraction Kit (Qiagen) according to the manufacturer's instructions.

5.2.4 λ Red Recombineering

λ Red Recombineering (*homologous recombination-mediated genetic engineering*) is a standard technique to endogenously modify genes (replace DNA segments or insert recombinant DNA) in *E. coli*. Homologous recombination is achieved by introducing linear DNA fragments of interest into cells which harbor a defective λ prophage on their chromosome (*e.g.* helper strain DY330[332]). Alternatively, the proteins encoded by the defective λ prophage can be expressed from the helper plasmid pKD46[335]. In short, homologous recombination is mediated by the proteins Bet, Gam and Exo, encoded by the genes *bet, gam* and *exo* on the prophage DNA. The Gam protein inhibits the *E. coli* RecBCD exonuclease, enabling the transformation by linear DNA fragments without their rapid degradation. Exo is proposed to degrade dsDNA (5'→3') into DNA with a double-stranded region that is flanked by 3' overhangs, allowing the Beta protein, an ssDNA annealing protein, to perform recombination with a complementary target.[336-338] According to an alternative theory, Exo completely degrades the dsDNA into a single-stranded intermediate that recombines at the replication fork mediated by annealing by the Beta protein[339].

In the following, the procedures necessary for homologous recombineering via the λ Red system are illustrated by describing the generation of a strain endogenously expressing a StrepII-tagged version of the assembly factor ObgE (**Figure 38**). For this purpose, the linear DNA fragment encoding the epitope-tagged assembly factor was generated by PCR (**5.2.2**). The corresponding fragment was purified by agarose gel electrophoresis and gel extraction (**5.2.3**). For selection of positive

transformants, the fragment was designed to additionally harbor a resistance cassette, flanked by frt sites (from plasmid pKD4[335]). Homologous recombination was achieved by introducing 45 bases of homology for 3′ insertion in frame *obgE*. Via electroporation the PCR fragment was transformed into competent DY330 cells that have been induced for the recombineering system (**5.2.4.1**). After selecting positive transformants, the sequence of interest was brought into target strains by P1 Phage transduction (**5.2.4.2**) and the resistance cassette was eliminated using a FLP recombinase expressing plasmid pCP20 (**5.2.4.3**).

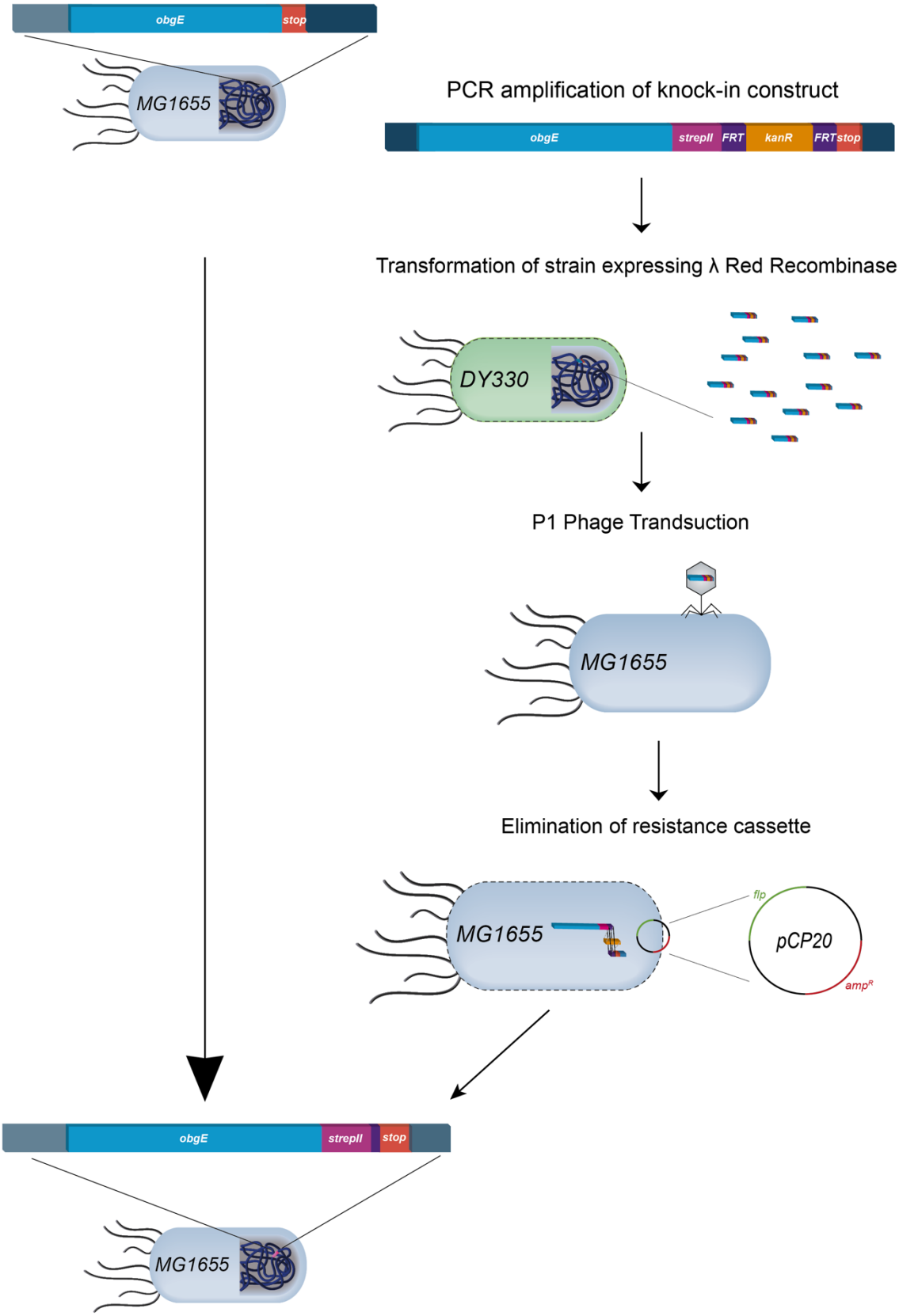

Figure 38: Gene disruption strategy for λ Red Recombineering. FRT = Flp recombinase target. HR = homologous regions. Amp^r = Ampicilin resistance cassette.

Table 10 lists the deletion and fusion strains that were generated using this technique.

5.2.4.1 λ Red Recombineering via helper strain DY330

DY330 is a helper strain that harbors the defective λ prophage in its genome. In this strain, the expression of the recombination genes is under control of a temperature-sensitive λ cI-repressor. This repressor represses the expression of genes from lambda promoters at low temperatures (28-30 °C)[340], while expression of target genes is derepressed at a temperature of 42 °C.

Consequently, *E. coli* DY330 cells were cultured at 200 rpm and 30 °C in a water bath shaker until they reached an OD_{600} of 0.5-0.8. To deactivate the repressor and induce temperature-sensitive expression of the prophage genes, the temperature was shifted to 42 °C for 15 minutes. Subsequently, cultures were immediately cooled down in an ice bath to stop the expression of the recombination genes. One culture was kept at 30 °C as a negative control. Cultures were sedimented at 4.4 krpm and 4 °C (Heraeus Multifuge 4KR) and washed three times using ice cold $_{dd}H_2O$ to lower the salt concentration. After the washing steps, cell pellets were resuspended in an appropriate amount of $_{dd}H_2O$ for electroporation (100 µl $_{dd}H_2O$ were used per 10 ml culture). 50 µl of this cell suspension were used for individual transformation reactions by electroporation (**5.2.4.2**).

5.2.4.2 Electroporation

For transformation, 100 ng of donor DNA were mixed with 50 µl of competent DY330 cells (**5.2.4.1**) in an electroporation cuvette with 2 mm gap width (Peqlab). After electroporation at 2.5 kV (Bio-Rad Gene Pulser Electroporation System, 25 µF and Pulse controller set to 200 ohms), 1 ml of ice-cold LB medium was added. For phenotypic expression, the mixture was transferred into a test tube and incubated at 30 °C for 1 hour in a roller drum. Non-induced cells were transformed

as negative control. As a second negative control, a corresponding volume of $_{dd}H_2O$ was added to induced cells instead of donor DNA. Cells were sedimented at 13 krpm for 1 minute (Heraeus Pico 21 microfuge), plated on selective LB-agar plates and incubated at 30 °C for a maximum of 48 hours. Successful deletions or insertions were verified by colony PCR and sequencing. Genetic modifications of interest were transferred into the target strain by P1-phage transduction (**5.2.4.3**).

5.2.4.3 P1 Phage Transduction

A stationary pre-culture of the donor strain was diluted 1:100 in 5 ml of fresh LB medium and incubated at the appropriate temperature while shaking until early log phase. 1 mM $CaCl_2$ (1 M stock) was added to facilitate transduction of the donor strain by P1 phages. Either 50 or 100 µl of P1 starter lysate added to the cultures, respectively. They were incubated at 30/ 37 °C (depending on the strain requirements) under constant shaking until lysis occurred. To ensure complete elimination of the donor cells, 3 drops of $CHCl_3$ were added to each sample and vortexed for 15 seconds. After incubation at room temperature for 10 minutes the supernatant was stored at 4 °C in a screw cap tube in the dark. Before transduction, cell debris were sedimented at 13 krpm (Heraeus Pico 21 microfuge) for 10 min and the donor lysate was filter-sterilized using a 0.2 µm filter to produce bacterial-free phage suspensions.

For transduction, stationary *E. coli* cells of the target strains were diluted 1:100 in 5 ml fresh LB medium and cultured until early log phase. 1 mM $CaCl_2$ (1 M stock) was added to allow infection of the acceptor strain. For one transduction reaction, 1 ml of cell culture was mixed with appropriate amounts of P1 lysate (50-100 µl), respectively and incubated for 15 min at RT. To minimize secondary infection, sodium citrate (1 mM) was added for chelation of calcium. Subsequently, the samples were incubated at 37 °C for 1 hour in a roller drum for phenotypic expression.

Cells were sedimented at 13 krpm for 1 minute (Heraeus Pico 21 Microfuge) and plated on selective plates, supplemented with 20 mM sodium citrate.

5.2.4.4 FLP Recombination to eliminate kanamycin resistance cassette

For elimination of the kanamycin resistance cassette, target strains were transformed with plasmid pCP20[334] (encodes FLP recombinase (thermally induced), possesses a temperature-sensitive origin of replication and confers ampicillin resistance). Incubation of the transformed strains at 42 °C for approximately 15 hours led to FLP recombinase expression and the loss of pCP20. Elimination of the plasmid and the resistance cassette was confirmed by the failure to grow on ampicillin and kanamycin plates.

5.2.5 Cloning of plasmids expressing PTasRNA

The oligonucleotides that were used to amplify asRNA sequences from the genomic DNA of the MG1655 strain by PCR are shown in table 11. The PCR fragments were digested with NcoI and XhoI and cloned into the NcoI-XhoI opened plasmids pHN678, pHN1009 and pHN1257[283], respectively. For standard digestion reaction, ~2-4 µg of either plasmid was digested in a final reaction volume of 20-30 µl and incubated for 2-4 hours at 37 °C according to the manufacterer's instructions. PCR fragments were purified by gel by gel extraction (**5.2.3**), eluted in 20 µl $_{dd}H_2O$ and digested as described above. Heat inactivation of restriction enzymes for 20 min at 80 °C was used to terminate the restriction reaction. FastAP Thermosensitive Alkaline Phosphatase was used for dephosphorylation of the vectors. For this purpose, 25 µl of the restriction reactions were mixed with 3.5 µl FastAP, 3.5 µl of FastAP buffer in a total volume of 35 µl at 37 °C for 20 min. FastAP was heat inactivated for 5 min at 75 °C. For ligation with T4 Ligase, 150 ng of linearized vector were mixed with the respective insert in a 1:3 or 1:2 molar ratio (total reaction volume of 20 µl) and incubated for 30 min at RT. A religation control was included.

After heat inactivation of T4 Ligase at 65 °C for 10 min, 10µl of the ligase reaction was immediately transformed into competent DH5α cells. PTasRNA expressing plasmids were brought into MCrg* by electroporation.

5.2.6 Transformation into chemically competent DH5α

100 µl of chemically competent DH5α cells were thawed on ice and mixed with 10 µl ligation reaction (**5.2.5**). Cells were incubated on ice for 30 min, heat-shocked for 90 s at 42 °C and subsequently cooled on ice for additional 90 s. 900 µl fresh LB medium were added, followed by phenotypic expression at 37 °C for 1 hour. Eventually, cells were plated on selective plates.

5.2.7 TSS Transformation

A stationary pre-culture of the target strain was diluted 1:100 in 5 ml of fresh LB medium and incubated at the appropriate temperature while shaking until early log phase. Cells were chilled on ice for 30 min and an aliquot was mixed 1:1 with 2xTSS. For transformation, 100 ng of plasmid DNA were mixed with 100 µl of competent cells and incubated on ice for 20 min. 900 µl fresh LB medium were added and the cultures were incubated at 37 °C for 1 hour to allow phenotypic expression. Cells were sedimented at 13 krpm for 1 minute (Heraeus Pico 21 Microfuge) and plated on selective plates.

5.2.8 Spot test analyses and growth tests in liquid medium

To test growth on solid media, stationary pre-cultures of the individual strains were diluted in fresh LB medium to a cell density of OD_{600} ~ 0.025. Five-fold serial dilutions were prepared and transferred onto LB agar plates using a plating stamp. The plates were supplemented with IPTG or antibiotics when necessary. Plates were incubated at 20 °C, 30 °C, 37 °C and 42 °C until single colonies of each dilution were visible.

For testing growth in liquid medium, stationary *E. coli* cells of the individual strains were diluted to an OD_{600} of 0.025 for incubation at 42 °C and to an OD_{600} = 0.05 for incubation at 37 °C and 20 °C. Cell suspensions of 25 ml were incubated in baffled flasks in a water bath incubator with a shaking frequency of 200 rpm until stationary phase was reached or a maximum of 10 hours had passed. OD_{600} was measured every 30 min or hourly using a Ultrospec 3100 pro photometer (GE Healthcare). Growth rates were calculated for periods of exponential growth and normalized to the wild-type strain.

To test growth and fluorescence of the strains in multiwell-format, stationary *E. coli* cells of MGrg in LB medium were diluted to an OD_{600} of 0.05 in LB medium. 80 µl aliquots (n=8) were pipetted manually into 384-multiwell plates and cultivated at 37 °C under constant shaking until stationary phase. A_{650} was determined every hour using Infinite F500 microplate reader (Tecan). Growth rates were calculated for periods of exponential growth and normalized to the wild-type strain.

5.2.9 Analytical sucrose gradient ultracentrifugation

Analytical sucrose gradient centrifugation was employed to separate different ribosomal populations (30S subunit, 50S subunit, 70S ribosome and polysomes). Stationary pre-cultures of the strain MG1655 and the epitope-tagged strains were diluted in fresh LB medium to OD_{600} = 0.05 and cultured to OD_{600} ~ 0.5-0.6. Five minutes before harvesting, chloramphenicol (250 µg/mL) was added. The cultures were immediately cooled down in an ice water bath and harvested at 5.5 krpm at 4 °C for 10 minutes (Rotor JLA-10.500). The pellets were flash-frozen in liquid nitrogen and stored at – 80 °C.

MGrg* strains transformed with PTasRNA expressing plasmids were cultivated differently. Stationary *E. coli* cells of these pre-cultures were diluted to OD_{600} = 0.1 and cultured at 120 rpm and 25 °C until OD_{600} = 0.15. To induce the expression of

PTasRNA, 1mM of IPTG was added and cells were further cultivated at 25 °C to OD_{600} = 0.3-0.5 before harvesting. For cultivation at 42 °C, stationary *E. coli* cells of these pre-cultures were diluted to OD_{600} = 0.05 and cultured at 120 rpm and 42 °C in the presence of 1mM of IPTG. Cells were to OD_{600} = 0.3-0.5 before harvesting.

To analyze co-fractionation of ObgE with ribosomal particles, cells of the individual strains were cultured in LB medium at 37 °C until stationary phase. Pre-cultures were diluted in fresh LB medium to OD_{600} = 0.05 and cultured to OD_{600} = 0.5-0.6 at 37 °C. Expression of *rplP*-specific PTasRNA was induced at an OD_{600}= 0.1. Harvesting and the preparation of cleared lysates was conducted as described above, with the exception that Chloramphenicol was neither added before harvesting nor added to the lysis buffer (**5.2.10**).

For further preparation, pellets were resuspended in 1 ml lysis buffer (table 2) and mechanically disrupted using FastPrep®-24.

5.2.10 Cell lysis using FastPrep®-24

For this purpose, cell suspensions were transferred into 2 ml screw-cap tubes, containing 1 g of acid washed glass beads (pre-equilibrated in 1 ml of lysis buffer) and homogenized at 5 m/s for 20 seconds. Homogenization was repeated three times with incubation on ice for 2 minutes in between. Samples were sedimented at 12.7 krpm and 4 °C (Eppendorf centrifuge 5427 R) for 7 min to pellet cell debris and lysing matrix. The supernatant was transferred into a new 2 ml reaction tube and centrifuged again at 12.7 krpm at 4 °C (Eppendorf centrifuge 5427 R) for 25 minutes. Concentrations of cleared lysates were adjusted to A_{260} = 20. 500 µl of the lysates were loaded on 11 ml of linear 10-40 % (w/v) sucrose gradients and sedimented at 17.5 krpm at 4 °C for 14:40 h in a SW41-Ti rotor (Beckmann). 10 % - 25 % sucrose gradients were used to analyze co-fractionation of ObgE with ribosomal

particles. The sucrose gradient was prepared using a gradient mixer (Gradient Master 107).

To assess the knock-down efficacy, protein concentration of the cleared lysate was determined via the BCA assay using the PierceTM BCA Protein Assay Kit. To calculate the standard curve 0-20 µg BSA were adjusted in a total volume of 50 µl (with lysis buffer), respectively. Protein samples were diluted (1:10 and 1:25) in lysis buffer and standard, as well as protein samples were mixed with 1 ml BCA working solution (table 2). Samples were incubated at 60 °C and 500 rpm for 15 minutes. After incubation on ice for 2 minutes, absorbance of the reaction mixtures was measured at 562 nm. Protein concentrations were adjusted to 20 µg total protein.

5.2.11 Polysome profile analyses and fluorometric analyses

Sucrose gradient centrifugates were analyzed using a Teledyne Isco gradient reader (Teledyne ISCOr, Lincoln, Nebraska, USA). A_{254} profiles were recorded and fractions were collected in 96-well plates (5 drops per well) for the following fluorometric analyses. mAzami and mCherry specific fluorescence emissions were determined using Infinite F500 fluorescence microplate reader (Tecan). The parameters are listed in table 15. Fluorescence intensities were normalized to the first polysome peak.

For analyzing ObgE co-fractionating with ribosomal particles, fractions of ~ 500 µl were collected for time intervals of 22 s each. Fluorometric analyses was performed with 200 µl aliquots in individual wells of 96-well plates.

Table 15: Parameters for fluorometric analyses by Tecan Infinite F500

Parameter	Value

mAzami specific Fluorescence	excitation: 485 nm ± 20 nm band width emission: 535 nm ± 25 nm band width gain: 40 number of reads: 10
mCherry specific Fluorescence	excitation: 535 nm ± 25 nm band width emission: 635 nm ± 35 nm band width gain: 50 number of reads: 10
Shaking parameters	3 seconds, linear mode, amplitude: 2 mm, frequency: 610.2 rpm

5.2.12 SDS-PAGE

To detect ObgE in sucrose gradient fractions, 32 µl of the collected fractions were resolved by 12 % Bis-Tris gels. Samples were mixed with 5x sample buffer (table 2), incubated for 5 minutes at 95 °C to denature proteins and loaded onto the gel. Electrophoresis was performed in 1x MOPS buffer (table 2). After concentrating the samples in the stacking gel with a current of 150 V, separation was conducted at 250 V for 2 hours and 30 min.

5.2.13 Western blot analysis

Proteins separated by SDS-PAGE were electroblotted onto a nitrocellulose membrane (250 mA for 2 hours and 45 min). After transfer, the membrane was incubated in 5 % (w/v) milk powder in 1x TBS-T to prevent unspecific binding of antibodies. First and secondary antibodies, as well as Strep-Tactin HRP conjugate were used at 1:10,000 dilution (monoclonal anti-FLAG M2 antibody and Strep-Tactin HRP conjugate: 1:10,000 in TBS-T; uS2 and bL19-specific antisera: 1:10,000 in TBS-T + 3 % (w/v) milk powder HRP-conjugated donkey anti-mouse or rabbit anti-sheep secondary antibodies in combination with ECL Western Blotting Detection

Reagent were used for immunodetection. Chemiluminescence was monitored using the chemiluminescence system FUSION SL (Analis).

5.2.14 Super-resolution fluorescence microscopy

Stationary *E. coli* cells of the strain MGrg* and the individual assembly factor depletion strains, were diluted in 25 ml fresh LB medium (supplemented with the respective antibiotics) to an initial OD_{600} of 0.1 and cultured 200 rpm and 37 °C until OD_{600} = 0.15. After addition of 1 mM IPTG to induce PTasRNA expression, cells were further cultured until OD_{600} = 0.3-0.5. 1 ml of cell suspension was centrifuged for 1 min at 13 krpm (Heraeus Pico 21 microfuge) and the pellet was resuspended in 1 ml or 100 µl of 4 % paraformaldehyde solution in 1x PBS and incubated for 30-60 min at 37 °C for fixation. Cells were sedimented and resuspended in 1xPBS + Glycine (1.5 mM) and incubated for 10 min at 37 °C. Cells were washed twice with PBS-G (1x PBS + 20 mM Glucose) and resuspended in 50-100 µl of PBS-G. For DNA staining, 0.5-1 µl of DAPI (0.1 µg/µl stock) was added and cells were incubated for at least 5 min.

3 µl of cell suspension were directly pipetted onto a high precision cover slip (18x18 mm, 170±5 µM) and covered with a 3 mm agarose pad with 0.5 cm edge length (0.5 % (w/v) agarose in PBS). The cover slip was placed headlong onto a 5 mm silicon imaging spacer, which was placed onto a microscope slide (**Figure 39**).

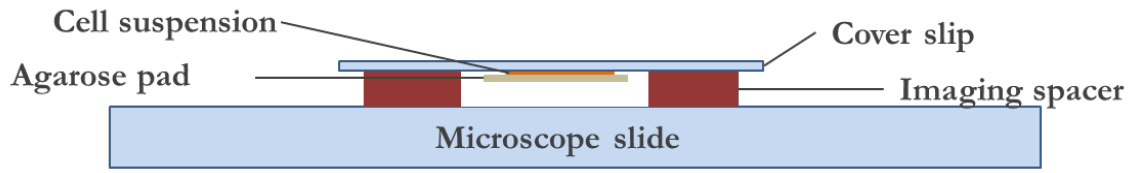

Figure 39: Sample preparation for microscopic analyses

3D SIM super resolution images were taken with a DeltaVision OMX Blazev4 microscope (GE Healthcare). Multichannel stacks (21 sections with 0.125 nm spacing

and a sample thickness of 2.5 μm) were recorded using a PlanApo N Olympus 60x 1.42 oil immersion objective (oil with refractive index of 1.516) and a sCMOS camera (512x512 pixels SIM). DAPI-stained DNA was monitored with 504 nm laser excitation (diode laser, exposure time: 100 ms, intensity: 10 or 31.3 %, gain: 1). mAzami-specific fluorescence was monitored using a 488 nm excitation laser (diode, exposure time: 50 ms, intensity: 1 %, gain: 1) and mCherry-specific fluorescence was monitored using 586 nm laser excitation (diode, exposure time: 80 or 20 ms, intensity: 10 %, gain: 1). Images were reconstructed using the SoftWorX package from GE Healthcare. From the structured illumination data image stacks with increased resolution were calculated and the different channels were registered. Pictures of mCherry-, mAzami- and DAPI-specific fluorescence of the same cut-out were adjusted to the appropriate dynamic range and merged using Fiji.

5.2.15 Isolation of pre-50S•ObgE complexes and cryo-EM

This part of „Material and methods" is quoted verbatim from the manuscript:

Snapshots of native pre-50S ribosomes reveal a biogenesis factor network and evolutionary specialization

R. Nikolay[1,*], T. Hilal[1,2*], S. Schmidt[3*], B. Qin[1], D. Schwefel[1], T. Mielke[4], J. Bürger[1,4], J. Loerke[1], K. Amikura[5,6], T. Flügel[1], T. Ueda[6,7], E. Deuerling[3] and C.M.T Spahn[1]

*These authors contributed equally to this work

1. Institut für Medizinische Physik und Biophysik, Charité – Universitätsmedizin Berlin, corporate member of Freie Universität Berlin, Humboldt-Universität zu Berlin, and Berlin Institute of Health, Berlin, Germany
2. Freie Universität Berlin, Research centre for electron microscopy, Fabeckstr. 36a, 14195 Berlin, Germany
3. Molekulare Mikrobiologie, Universität Konstanz, Germany
4. Microscopy and Cryo-Electron Microscopy Service Group, Max Planck Institute for Molecular Genetics, Ihnestr. 63-73, 14195 Berlin, Germany

5. Department of Computational Biology and Medical Sciences, Graduate School of Frontier Sciences, The University of Tokyo, FSB-401, 5-1-5, Kashiwanoha, Kashiwa, Chiba 277-8562, Japan.
6. Present address: Department of Molecular Biophysics and Biochemistry, Yale University, New Haven, CT 06511, USA
7. Present address: Department of Integrative Bioscience and Biomedical Engineering, Graduate School of Science and Engineering, Waseda University, 2-2 Wakamatsu-cho, Shinjuku-ku, Tokyo 162–8480, Japan

"Isolation of pre-50S•ObgE-StrepII complexes

Two liters 2xYT cultures in 5-liter flasks (batch 1, 16 liters; batch 2, 32 liters in total) were inoculated with MG1655-obgE-strepII cells from a stationary culture to a start OD_{600} of 0.05. Cells were incubated at 140 rpm and 37 °C to an OD_{600} of 0.5-0.6. Cell suspensions were sedimented in a JLA 9.1000 rotor (Beckman Coulter) for 15 min at 5.5 krpm and 4 °C, subsequently pellets were flash-frozen in liquid nitrogen and stored at -80 °C. Pellets were resuspended in lysis buffer (50 mM TRIS pH 7.8, 100 mM KCl, 10 mM $MgCl_2$, 1 mM DTT, TM Complete) on ice and cells were lyzed by two cycles in an ice-cooled microfluidizer device (Microfluidics). The cell lysate was centrifuged in a JLA25.50 rotor for 30 min at 22.5 krpm and 4 °C. The cleared lysate was loaded on a 1 ml Strep-TactinTM XT SuperflowTM high capacity column (iba-lifesciences) equilibrated with buffer A (50 mM TRIS pH 7.8, 100 mM KCl, 10 mM $MgCl_2$, 1 mM DTT), using Äkta pure FPLC (GE Healthcare Life Sciences). The column was washed with 10 column volumes buffer A and bound protein complexes were eluted with buffer B (50 mM TRIS pH 7.8, 100 mM KCl, 10 mM $MgCl_2$, 1 mM DTT, 50 mM biotin). Fractions with highest protein content were pooled and concentrated three-fold, using a spin concentrator (Amicon ultra-15 30,000 MWCO, Millipore). Both, samples for cryo-EM analysis and for analytical sucrose gradient runs were applied freshly without prior freezing. For control purpose, a MG1655 wild type culture was subjected to the same purification procedure and the eluate of the Strep-Tactin column (unspecific background) was concentrated three-fold, as well.

[…]

Analytical sucrose gradient ultracentrifugation of pre-50S•ObgE-StrepII

0.6 A_{260} (batch 1) and 0.8 A_{260} (batch 2) of pre-50S•ObgE-StrepII particles were loaded on a 10-30 % sucrose gradient (in 50 mM TRIS pH 7.8, 100 mM KCl, 10 mM $MgCl_2$, 1 mM DTT) and subjected to ultracentrifugation in a SW40 rotor for 16 hours at 26 krpm and 4°C.

[…]

Cryo-electron microscopy

3.5 µl of freshly isolated pre-50S•ObgE-StrepII particles (8 A_{260}/ml) were applied to glow-discharged R2/4 holey carbon grids with 2 nm continuous carbon film on top (Quantifoil MicroTools GmbH) and cryo plunged in liquid ethane (-157 °C) after blotting using a Vitrobot device (FEI) operated at 7 °C and set to 100 % humidity. Data were collected on a FEI Tecnai G2 Polara equipped with a Gatan K2 Summit detector operated in super-resolution mode at 300 kV at a calibrated pixel size of 0.62 A°. Movies were acquired for 5 s applying a total electron dose of 30 $e^-/Å^2$. In vitro reconstituted 50S•ObgE•GMP-PNP complexes (20 A_{260}/ml) were applied to glow-discharged R1/4 holey carbon grids (Quantifoil MicroTools GmbH) and cryo-plunged using a Vitrobot Mark IV (FEI) at 10 °C and 100 % humidity. Imaging was performed on a FEI Talos Arctica equipped with a Falcon3EC operated at 200 kV with a calibrated pixel size of 0.85 Å. Movies were recorded for 0.35 s with a total electron dose of 60 $e^-/ Å^2$ in linear mode.

Data processing

K2 super-resolution movies were aligned and dose-weighted with MotionCor2 (Zheng et al., 2017[341]). Estimation of defocus values was achieved with Gctf (Zhang, 2016[342]). Gautomatch (developed by K. Zhang) was applied for reference-free picking of particle coordinates. Particle images were extracted and normalized with Relion 2.1 (Kimanius et al., 2016[343]) using a box size of 540 and Fourier cropped to 90 for further processing. Cryosparc v2 (Punjani et al., 2017[344]) was employed to remove bad particles after reference-free 2D classification and for initial estimation of orientational parameters by homogenous refinement using a low-pass filtered (40A°) 50S reference map. Subsequent iterative classification of particle images was accomplished with Frealign/cisTEM (Grant et al., 2018[345]; Zeng et al., 2007[346]). After completion of particle classifications, particle images were re-extracted and cropped to a box size of 270. Per particle defocus estimation and high-resolution refinement was finally done with cisTEM. Falcon3EC movies were processed in a similar manner with the exception that particle picking was achieved template-based with Cryosparc. Extraction was done with a box size of 400 and particle images were initially cropped to 100 for 2D and 3D classifications. For the final refinement steps unbinned particles were used.

Model building

Initial modeling of the ribosome was achieved by rigid body docking of a 50S subunit from a 70S crystal structure (PDB-ID 3R8S (Dunkle et al., 2011[347])) in Chimera (Pettersen et al., 2004[348]). Flexible fitting of ribosomal RNA was achieved by MD-simulation with MDFit (Whitford et al., 2011[349]). Extensively altered regions, e.g.

H69 of the 23S rRNA, were tentatively modeled manually using coot-0.8.9 (Emsley and Cowtan, 2004[350]). The unprocessed RNA of the precursor was modeled as idealized RNA helix based on the sequence given in (Gutgsell and Jain, 2012[351]). Ribosomal proteins, whose densities were absent in our maps were deleted. ObgE was modeled by individual rigid body docking of the N- and C-terminal domain from the crystal structure PDB-ID 5M04 (Gkekas et al., 2017[201]). Disordered regions of the reference were modeled de novo and altered regions were manually adjusted in coot. YjgA was homology modeled based on the Pseudomonas syringae crystal structure PDB-ID 2P0T with minor modifications and RluD was modeled by rigid-body docking of the Escherichia coli crystal structure (PDB-ID 2IST) followed by manual adjustments. RsfS was homology modeled based on the Mycobacterium tuberculosis crystal structure PDB-ID 4WCW (Li et al., 2015[352]). A final real-space refinement was implemented using Phenix 1.13 (Adams et al., 2010[353]) to improve model statistics, carefully monitoring overfitting. Modeling of the in vitro reconstituted 50S•ObgE complex was achieved similarly with the exception that the pre-50S•ObgE-StrepII derived ObgE-model served as starting point for MDFit, followed by Phenix real-space refinement."

5.2.16 High-throughput screening

To test growth and fluorescence of the strains in multiwell-format, stationary *E. coli* cells of MGrg in LB medium were washed twice, diluted in M9 minimal medium and cultured again until stationary phase. They were then diluted to an OD_{600} of 0.05 in M9 minimal medium. 80 µl aliquots were pipetted manually into 384-multiwell plates using a multichannel pipette (Intron). Before compound transfer, cells were pre-incubated at 30 °C in a tower shaker for 10 minutes (shaking frequency: 8.5 Hz). A pipetting robot (Tecan Freedom EVO Workstation) was employed to transfer the appropriate amount of each compound or DMSO at time point t_0 (final compound concentration 10µM).

After compound transfer, both absorption at 650 nm and mAzami- and mCherry-specific fluorescence intensities were measured fully automated every hour in a

microplate reader (Tecan Infinite F500) for a time span of 12 hours. Between measurements, cells were incubated at 30 °C in a tower shaker (shaking frequency: 8.5 Hz). The parameters are listed in table 16.

Afterwards, fluorescence ratios were calculated by dividing the mAzami-specific fluorescence emission by the one of mCherry. Ratios were normalized to the mean value of the untreated reporter strain (control: n=22).

Table 16: Parameters for fluorometric analyses by Tecan Infinite F500

Parameter	Value
mAzami specific Fluorescence	excitation: 485 nm ± 20 nm band width emission: 535 nm ± 25 nm band width gain: 40 number of reads: 10
mCherry specific Fluorescence	excitation: 535 nm ± 25 nm band width emission: 635 nm ± 35 nm band width gain: 50 number of reads: 10
Absorbance	650 nm

6. Abbreviations

Å	Ångström unit	GAC	GTPase-associated center
A_{260}	Absorption at 260 nm	GFP	Green Fluorescent Protein
°C	Degrees celsius	H_2O_2	Hydrogen peroxide
µg	Microgram	HCl	Hydrochloric acid
aa	Amino acid	HRP	Horseradish peroxidase
Amp	Ampicillin	IPTG	Isopropyl β-D-1-thiogalac-topyranoside
µl	Microliter	KCl	Potassium chloride
$CaCl_2$	Calcium chloride	kDA	Kilodalton
Cam	Chloramphenicol	KH_2PO_4	Monopotassium phosphate
cryo-EM	cryogenic electron microscopy	krpm	Kilo rotation per minute
Da/kDa	Dalton/Kilodalton	l	Liter
DMSO	Dimethyl sulfoxide	LB	Lysogeny broth
DNA	Deoxyribonucleic acid	M	Molar
dNTP	Desoxyribonucleosidtriphosphate	mA	Milliampere
DTT	Dithiothreitol	$MgCl_2$	Magnesium chloride
E. coli	*Escherichia coli*	$MgSO_4$	Magnesium sulfate
e.g.	Exempli gratia	min	Minute/s
et al.	And others, lat: et alii	mM	Millimole
EGFP	Green Fluorescent Protein	MOPS	3-(N-morpholino)propane-sulfonic acid
FC	Functional core	mRNA	Messenger ribonucleic acid
FP	Fluorescent protein	N_2	Nitrogen
fwd	forward	NaCl	Sodium chloride
Na_2HPO_4	Disodium phosphate	rRNA	Ribosomal ribonucleoic acid

Abbreviations

NH_4Cl	Ammonium chloride	S	Svedberg Constant
OD_{600}	Optical density at 600 nm	s	Second/s
PBS	Phosphate buffered saline	Sol.	Solution
PCR	Polymerase chain reaction	SDS	Sodium dodecyl sulfate
pmol	Picomole	SDS-PAGE	SDS polyacrylamide gelelectrophoresis
PMSF	Phenylmethylmulfonylfluorid	TBS	Tris buffered saline
PTC	Peptidyl transferase center	Tris	Tris(hydroxymethyl)aminomethane
RNA	Ribonucleic acid	tRNA	Transfer ribonucleic acid
rev	reverse	V	Volt
rpm	rounds per minute	v/v	Volume per volume
RP	Ribosomal protein	w/v	Weight per volume

7. Figure licenses

Figure 3

License-ID: 1021734-1

Nucleic Acids Research by Fluorescence by Oxford Univserity Press - Journals.

Reproduced with permission of Oxford Univserity Press - Journals in the format thesis/dissertation via Copyright Clearance Center.

Figure 4

License-ID: 1021734-1

Nucleic Acids Research by Oxford University Press - Journals.

Reproduced with permission of Oxford University Press - Journals in the format thesis/dissertation via Copyright Clearance Center.

Figure 5

Under Creative Commons Attribution (CC BY 3.0) license.

Information: Retrieved from. http://apollo.chemistry.gatech.edu/RibosomeGallery. Petrov, A. S. et al. Secondary structure and domain architecture of the 23S and 5S rRNAs. Nucleic Acids Res 41, 7522-7535, doi:10.1093/nar/gkt513 (2013).

Accessed 6 March 2020.

Figure 8

Under Creative Commons Attribution (CC BY 4.0) license

Bennison, D. J., Irving, S. E. & Corrigan, R. M. The Impact of the Stringent Response on TRAFAC GTPases and Prokaryotic Ribosome Assembly. *Cells* **8**, doi:10.3390/cells8111313 (2019).

Figure 9

License-ID: 1021735-1

Figure licences

Methods and Applications in Fluorescence by Annual Reviews, Inc.

Reproduced with permission of Annual Reviews, Inc. in the format thesis/dissertation via Copyright Clearance Center.

Figure 10

License-ID: 1021735-1

Methods and Applications in Fluorescence by Annual Reviews, Inc.

Reproduced with permission of Annual Reviews, Inc. in the format thesis/dissertation via Copyright Clearance Center.

Figure 15

License-ID: 1021707-1

Methods and Applications in Fluorescence by IOP Publishing.

Reproduced with permission of IOP Publishing in the format thesis/dissertation via Copyright Clearance Center.

Figure 16

Under Creative Commons Attribution (CC BY 4.0) license.

Information: Claudionico commonswiki. (2015) *Electron Interaction with Matter*. https://commons.wikimedia.org/wiki/File:Electron_Interaction_with_Matter.svg. Accessed 6 March 2020.

Claudionico~commonswiki/ CC BY-SA (https://creativecommons.org/licenses/by-sa/4.0

Figure 24

License-ID: 1022338-1

Nucleic Acids Research by Oxford University Press – Journals.

Reproduced with permission of Oxford University Press in the format thesis/dissertation via Copyright Clearance Center.

8. Literature

1 Claude, A. The Constitution of Protoplasm. *Science* **97**, 451-456, doi:10.1126/science.97.2525.451 (1943).
2 Cleaves, H. J. in *Encyclopedia of Astrobiology* (eds Muriel Gargaud *et al.*) 2446-2446 (Springer Berlin Heidelberg, 2015).
3 Schachman, H. K., Pardee, A. B. & Stanier, R. Y. Studies on the macro-molecular organization of microbial cells. *Arch Biochem Biophys* **38**, 245-260, doi:10.1016/0003-9861(52)90029-5 (1952).
4 Palade, G. E. A small particulate component of the cytoplasm. *J Biophys Biochem Cytol* **1**, 59-68, doi:10.1083/jcb.1.1.59 (1955).
5 Littlefield, J. W., Keller, E. B., Gross, J. & Zamecnik, P. C. Studies on cytoplasmic ribonucleoprotein particles from the liver of the rat. *J Biol Chem* **217**, 111-123 (1955).
6 Chao, F. C. & Schachman, H. K. The isolation and characterization of a macro-molecular ribonucleoprotein from yeast. *Arch Biochem Biophys* **61**, 220-230, doi:10.1016/0003-9861(56)90334-4 (1956).
7 Ts'O, P. O., Bonner, J., Eggman, L. & Vinograd, J. Observations on an ATP-sensitive protein system from the plasmodia of a myxomycete. *J Gen Physiol* **39**, 325-347, doi:10.1085/jgp.39.3.325 (1956).
8 Petermann, M. L. & Hamilton, M. G. The purification and properties of cytoplasmic ribonucleoprotein from rat liver. *J Biol Chem* **224**, 725-736 (1957).
9 Tissieres, A. & Watson, J. D. Ribonucleoprotein particles from Escherichia coli. *Nature* **182**, 778-780, doi:10.1038/182778b0 (1958).
10 Biophysical Society. Symposium (1st : 1958 : Cambridge Mass.) & Roberts, R. B. *Microsomal particles and protein synthesis; papers presented at the First Symposium of the Biophysical Society, at the Massachusetts Institute of Technology, Cambridge, February 5, 6, and 8, 1958*. (Published on behalf of the Washington Academy of Sciences, Washington, D.C., by Pergamon Press, 1958).
11 Schluenzen, F., Tocilj, A., Zarivach, R., Harms, J., Gluehmann, M., Janell, D., . . . Yonath, A. Structure of functionally activated small ribosomal subunit at 3.3 angstroms resolution. *Cell* **102**, 615-623, doi:10.1016/s0092-8674(00)00084-2 (2000).
12 Ban, N., Nissen, P., Hansen, J., Moore, P. B. & Steitz, T. A. The complete atomic structure of the large ribosomal subunit at 2.4 A resolution. *Science* **289**, 905-920, doi:10.1126/science.289.5481.905 (2000).
13 Wimberly, B. T., Brodersen, D. E., Clemons, W. M., Jr., Morgan-Warren, R. J., Carter, A. P., Vonrhein, C., . . . Ramakrishnan, V. Structure of the 30S ribosomal subunit. *Nature* **407**, 327-339, doi:10.1038/35030006 (2000).
14 Williamson, J. R. The ribosome at atomic resolution. *Cell* **139**, 1041-1043, doi:10.1016/j.cell.2009.11.028 (2009).
15 Palade, G. E. & Siekevitz, P. Pancreatic microsomes; an integrated morphological and biochemical study. *J Biophys Biochem Cytol* **2**, 671-690, doi:10.1083/jcb.2.6.671 (1956).
16 Nomura, M., Gourse, R. & Baughman, G. Regulation of the synthesis of ribosomes and ribosomal components. *Annu Rev Biochem* **53**, 75-117, doi:10.1146/annurev.bi.53.070184.000451 (1984).
17 Bremer, H. & Dennis, P. P. Modulation of Chemical Composition and Other Parameters of the Cell at Different Exponential Growth Rates. *EcoSal Plus* **3**, doi:10.1128/ecosal.5.2.3 (2008).
18 de Narvaez, C. C. & Schaup, H. W. In vivo transcriptionally coupled assembly of Escherichia coli ribosomal subunits. *J Mol Biol* **134**, 1-22 (1979).

19 Moore, P. B. & Steitz, T. A. The roles of RNA in the synthesis of protein. *Cold Spring Harb Perspect Biol* **3**, a003780, doi:10.1101/cshperspect.a003780 (2011).
20 Steitz, T. A. & Moore, P. B. RNA, the first macromolecular catalyst: the ribosome is a ribozyme. *Trends Biochem Sci* **28**, 411-418, doi:10.1016/S0968-0004(03)00169-5 (2003).
21 Glotz, C., Zwieb, C., Brimacombe, R., Edwards, K. & Kossel, H. Secondary structure of the large subunit ribosomal RNA from Escherichia coli, Zea mays chloroplast, and human and mouse mitochondrial ribosomes. *Nucleic Acids Res* **9**, 3287-3306, doi:10.1093/nar/9.14.3287 (1981).
22 Branlant, C., Krol, A., Machatt, M. A., Pouyet, J., Ebel, J. P., Edwards, K. & Kossel, H. Primary and secondary structures of Escherichia coli MRE 600 23S ribosomal RNA. Comparison with models of secondary structure for maize chloroplast 23S rRNA and for large portions of mouse and human 16S mitochondrial rRNAs. *Nucleic Acids Res* **9**, 4303-4324, doi:10.1093/nar/9.17.4303 (1981).
23 Noller, H. F., Kop, J., Wheaton, V., Brosius, J., Gutell, R. R., Kopylov, A. M., . . . Waese, C. R. Secondary structure model for 23S ribosomal RNA. *Nucleic Acids Res* **9**, 6167-6189, doi:10.1093/nar/9.22.6167 (1981).
24 Petrov, A. S., Bernier, C. R., Hershkovits, E., Xue, Y., Waterbury, C. C., Hsiao, C., . . . Williams, L. D. Secondary structure and domain architecture of the 23S and 5S rRNAs. *Nucleic Acids Res* **41**, 7522-7535, doi:10.1093/nar/gkt513 (2013).
25 Brown, A. & Shao, S. Ribosomes and cryo-EM: a duet. *Curr Opin Struct Biol* **52**, 1-7, doi:10.1016/j.sbi.2018.07.001 (2018).
26 Radermacher, M., Wagenknecht, T., Verschoor, A. & Frank, J. Three-dimensional reconstruction from a single-exposure, random conical tilt series applied to the 50S ribosomal subunit of Escherichia coli. *J Microsc* **146**, 113-136, doi:10.1111/j.1365-2818.1987.tb01333.x (1987).
27 Kaczanowska, M. & Ryden-Aulin, M. Ribosome biogenesis and the translation process in Escherichia coli. *Microbiol Mol Biol Rev* **71**, 477-494, doi:10.1128/MMBR.00013-07 (2007).
28 Korepanov, A. P., Korobeinikova, A. V., Shestakov, S. A., Garber, M. B. & Gongadze, G. M. Protein L5 is crucial for in vivo assembly of the bacterial 50S ribosomal subunit central protuberance. *Nucleic Acids Res* **40**, 9153-9159, doi:10.1093/nar/gks676 (2012).
29 Korepanov, A. P., Gongadze, G. M., Garber, M. B., Court, D. L. & Bubunenko, M. G. Importance of the 5 S rRNA-binding ribosomal proteins for cell viability and translation in Escherichia coli. *J Mol Biol* **366**, 1199-1208, doi:10.1016/j.jmb.2006.11.097 (2007).
30 Boublik, M., Hellmann, W. & Roth, H. E. Localization of ribosomal proteins L7L12 in the 50 S subunit of Escherichia coli Ribosomes by electron microscopy. *J Mol Biol* **107**, 479-490, doi:10.1016/s0022-2836(76)80079-4 (1976).
31 Strycharz, W. A., Nomura, M. & Lake, J. A. Ribosomal proteins L7/L12 localized at a single region of the large subunit by immune electron microscopy. *J Mol Biol* **126**, 123-140, doi:10.1016/0022-2836(78)90355-8 (1978).
32 Cornish, P. V., Ermolenko, D. N., Staple, D. W., Hoang, L., Hickerson, R. P., Noller, H. F. & Ha, T. Following movement of the L1 stalk between three functional states in single ribosomes. *Proc Natl Acad Sci U S A* **106**, 2571-2576, doi:10.1073/pnas.0813180106 (2009).
33 Fei, J., Kosuri, P., MacDougall, D. D. & Gonzalez, R. L., Jr. Coupling of ribosomal L1 stalk and tRNA dynamics during translation elongation. *Mol Cell* **30**, 348-359, doi:10.1016/j.molcel.2008.03.012 (2008).
34 Wang, X., Kirkpatrick, J. P., Launay, H. M. M., de Simone, A., Haussinger, D., Dobson, C. M., . . . Christodoulou, J. Probing the dynamic stalk region of the ribosome using solution NMR. *Sci Rep* **9**, 13528, doi:10.1038/s41598-019-49190-1 (2019).

35 Mohan, S. & Noller, H. F. Recurring RNA structural motifs underlie the mechanics of L1 stalk movement. *Nat Commun* **8**, 14285, doi:10.1038/ncomms14285 (2017).
36 Gao, H., Sengupta, J., Valle, M., Korostelev, A., Eswar, N., Stagg, S. M., . . . Frank, J. Study of the structural dynamics of the E coli 70S ribosome using real-space refinement. *Cell* **113**, 789-801, doi:10.1016/s0092-8674(03)00427-6 (2003).
37 Korostelev, A., Trakhanov, S., Laurberg, M. & Noller, H. F. Crystal structure of a 70S ribosome-tRNA complex reveals functional interactions and rearrangements. *Cell* **126**, 1065-1077, doi:10.1016/j.cell.2006.08.032 (2006).
38 Tourigny, D. S., Fernandez, I. S., Kelley, A. C. & Ramakrishnan, V. Elongation factor G bound to the ribosome in an intermediate state of translocation. *Science* **340**, 1235490, doi:10.1126/science.1235490 (2013).
39 Bock, L. V., Blau, C., Schroder, G. F., Davydov, II, Fischer, N., Stark, H., . . . Grubmuller, H. Energy barriers and driving forces in tRNA translocation through the ribosome. *Nat Struct Mol Biol* **20**, 1390-1396, doi:10.1038/nsmb.2690 (2013).
40 Diaconu, M., Kothe, U., Schlunzen, F., Fischer, N., Harms, J. M., Tonevitsky, A. G., . . . Wahl, M. C. Structural basis for the function of the ribosomal L7/12 stalk in factor binding and GTPase activation. *Cell* **121**, 991-1004, doi:10.1016/j.cell.2005.04.015 (2005).
41 Heimark, R. L., Hershey, J. W. & Traut, R. R. Cross-linking of initiation factor IF2 to proteins L7/L12 in 70 S ribosomes of Escherichia coli. *J Biol Chem* **251**, 7779-7784 (1976).
42 Savelsbergh, A., Mohr, D., Wilden, B., Wintermeyer, W. & Rodnina, M. V. Stimulation of the GTPase activity of translation elongation factor G by ribosomal protein L7/12. *J Biol Chem* **275**, 890-894, doi:10.1074/jbc.275.2.890 (2000).
43 Youngman, E. M., Brunelle, J. L., Kochaniak, A. B. & Green, R. The active site of the ribosome is composed of two layers of conserved nucleotides with distinct roles in peptide bond formation and peptide release. *Cell* **117**, 589-599, doi:10.1016/s0092-8674(04)00411-8 (2004).
44 Chowdhury, S., Pal, S., Ghosh, J. & DasGupta, C. Mutations in domain V of the 23S ribosomal RNA of Bacillus subtilis that inactivate its protein folding property in vitro. *Nucleic Acids Res* **30**, 1278-1285, doi:10.1093/nar/30.5.1278 (2002).
45 Pal, D., Chattopadhyay, S., Chandra, S., Sarkar, D., Chakraborty, A. & Das Gupta, C. Reactivation of denatured proteins by domain V of bacterial 23S rRNA. *Nucleic Acids Res* **25**, 5047-5051, doi:10.1093/nar/25.24.5047 (1997).
46 Noller, H. F. Ribosomal RNA and translation. *Annu Rev Biochem* **60**, 191-227, doi:10.1146/annurev.bi.60.070191.001203 (1991).
47 Noller, H. F., Hoffarth, V. & Zimniak, L. Unusual resistance of peptidyl transferase to protein extraction procedures. *Science* **256**, 1416-1419, doi:10.1126/science.1604315 (1992).
48 Beringer, M. & Rodnina, M. V. The ribosomal peptidyl transferase. *Mol Cell* **26**, 311-321, doi:10.1016/j.molcel.2007.03.015 (2007).
49 Nissen, P., Hansen, J., Ban, N., Moore, P. B. & Steitz, T. A. The structural basis of ribosome activity in peptide bond synthesis. *Science* **289**, 920-930, doi:10.1126/science.289.5481.920 (2000).
50 Lancaster, L., Lambert, N. J., Maklan, E. J., Horan, L. H. & Noller, H. F. The sarcin-ricin loop of 23S rRNA is essential for assembly of the functional core of the 50S ribosomal subunit. *RNA* **14**, 1999-2012, doi:10.1261/rna.1202108 (2008).
51 Li, W., Sengupta, J., Rath, B. K. & Frank, J. Functional conformations of the L11-ribosomal RNA complex revealed by correlative analysis of cryo-EM and molecular dynamics simulations. *RNA* **12**, 1240-1253, doi:10.1261/rna.2294806 (2006).

52 Connell, S. R., Takemoto, C., Wilson, D. N., Wang, H., Murayama, K., Terada, T., . . . Spahn, C. M. Structural basis for interaction of the ribosome with the switch regions of GTP-bound elongation factors. *Mol Cell* **25**, 751-764, doi:10.1016/j.molcel.2007.01.027 (2007).
53 Gilbert, R. J., Fucini, P., Connell, S., Fuller, S. D., Nierhaus, K. H., Robinson, C. V., . . . Stuart, D. I. Three-dimensional structures of translating ribosomes by Cryo-EM. *Mol Cell* **14**, 57-66, doi:10.1016/s1097-2765(04)00163-7 (2004).
54 Woolhead, C. A., McCormick, P. J. & Johnson, A. E. Nascent membrane and secretory proteins differ in FRET-detected folding far inside the ribosome and in their exposure to ribosomal proteins. *Cell* **116**, 725-736, doi:10.1016/s0092-8674(04)00169-2 (2004).
55 Etchells, S. A. & Hartl, F. U. The dynamic tunnel. *Nat Struct Mol Biol* **11**, 391-392, doi:10.1038/nsmb0504-391 (2004).
56 Kudva, R., Tian, P., Pardo-Avila, F., Carroni, M., Best, R. B., Bernstein, H. D. & von Heijne, G. The shape of the bacterial ribosome exit tunnel affects cotranslational protein folding. *Elife* **7**, doi:10.7554/eLife.36326 (2018).
57 Fulle, S. & Gohlke, H. Statics of the ribosomal exit tunnel: implications for cotranslational peptide folding, elongation regulation, and antibiotics binding. *J Mol Biol* **387**, 502-517, doi:10.1016/j.jmb.2009.01.037 (2009).
58 Tenson, T. & Ehrenberg, M. Regulatory nascent peptides in the ribosomal tunnel. *Cell* **108**, 591-594, doi:10.1016/s0092-8674(02)00669-4 (2002).
59 Nakatogawa, H. & Ito, K. The ribosomal exit tunnel functions as a discriminating gate. *Cell* **108**, 629-636, doi:10.1016/s0092-8674(02)00649-9 (2002).
60 Yonath, A. Antibiotics targeting ribosomes: resistance, selectivity, synergism and cellular regulation. *Annu Rev Biochem* **74**, 649-679, doi:10.1146/annurev.biochem.74.082803.133130 (2005).
61 Berisio, R., Schluenzen, F., Harms, J., Bashan, A., Auerbach, T., Baram, D. & Yonath, A. Structural insight into the role of the ribosomal tunnel in cellular regulation. *Nat Struct Biol* **10**, 366-370, doi:10.1038/nsb915 (2003).
62 Woese, C. R., Magrum, L. J., Gupta, R., Siegel, R. B., Stahl, D. A., Kop, J., . . . Noller, H. F. Secondary structure model for bacterial 16S ribosomal RNA: phylogenetic, enzymatic and chemical evidence. *Nucleic Acids Res* **8**, 2275-2293, doi:10.1093/nar/8.10.2275 (1980).
63 Noller, H. F. & Woese, C. R. Secondary structure of 16S ribosomal RNA. *Science* **212**, 403-411, doi:10.1126/science.6163215 (1981).
64 Woese, C. R., Gutell, R., Gupta, R. & Noller, H. F. Detailed analysis of the higher-order structure of 16S-like ribosomal ribonucleic acids. *Microbiol Rev* **47**, 621-669 (1983).
65 Ramakrishnan, V. & Moore, P. B. Atomic structures at last: the ribosome in 2000. *Curr Opin Struct Biol* **11**, 144-154, doi:10.1016/s0959-440x(00)00184-6 (2001).
66 Rodnina, M. V. The ribosome in action: Tuning of translational efficiency and protein folding. *Protein Sci* **25**, 1390-1406, doi:10.1002/pro.2950 (2016).
67 O'Connor, M., Thomas, C. L., Zimmermann, R. A. & Dahlberg, A. E. Decoding fidelity at the ribosomal A and P sites: influence of mutations in three different regions of the decoding domain in 16S rRNA. *Nucleic Acids Res* **25**, 1185-1193, doi:10.1093/nar/25.6.1185 (1997).
68 Steitz, J. A. & Jakes, K. How ribosomes select initiator regions in mRNA: base pair formation between the 3' terminus of 16S rRNA and the mRNA during initiation of protein synthesis in Escherichia coli. *Proc Natl Acad Sci U S A* **72**, 4734-4738, doi:10.1073/pnas.72.12.4734 (1975).
69 Shine, J. & Dalgarno, L. The 3'-terminal sequence of Escherichia coli 16S ribosomal RNA: complementarity to nonsense triplets and ribosome binding sites. *Proc Natl Acad Sci U S A* **71**, 1342-1346, doi:10.1073/pnas.71.4.1342 (1974).

70 Kaminishi, T., Wilson, D. N., Takemoto, C., Harms, J. M., Kawazoe, M., Schluenzen, F., . . . Yokoyama, S. A snapshot of the 30S ribosomal subunit capturing mRNA via the Shine-Dalgarno interaction. *Structure* **15**, 289-297, doi:10.1016/j.str.2006.12.008 (2007).
71 Di Giacco, V., Marquez, V., Qin, Y., Pech, M., Triana-Alonso, F. J., Wilson, D. N. & Nierhaus, K. H. Shine-Dalgarno interaction prevents incorporation of noncognate amino acids at the codon following the AUG. *Proc Natl Acad Sci U S A* **105**, 10715-10720, doi:10.1073/pnas.0801974105 (2008).
72 Demirci, H., Wang, L., Murphy, F. V. t., Murphy, E. L., Carr, J. F., Blanchard, S. C., . . . Gregory, S. T. The central role of protein S12 in organizing the structure of the decoding site of the ribosome. *RNA* **19**, 1791-1801, doi:10.1261/rna.040030.113 (2013).
73 Takyar, S., Hickerson, R. P. & Noller, H. F. mRNA helicase activity of the ribosome. *Cell* **120**, 49-58, doi:10.1016/j.cell.2004.11.042 (2005).
74 Cukras, A. R., Southworth, D. R., Brunelle, J. L., Culver, G. M. & Green, R. Ribosomal proteins S12 and S13 function as control elements for translocation of the mRNA:tRNA complex. *Mol Cell* **12**, 321-328, doi:10.1016/s1097-2765(03)00275-2 (2003).
75 Shajani, Z., Sykes, M. T. & Williamson, J. R. Assembly of bacterial ribosomes. *Annu Rev Biochem* **80**, 501-526, doi:10.1146/annurev-biochem-062608-160432 (2011).
76 Thomson, E., Ferreira-Cerca, S. & Hurt, E. Eukaryotic ribosome biogenesis at a glance. *J Cell Sci* **126**, 4815-4821, doi:10.1242/jcs.111948 (2013).
77 Venema, J. & Tollervey, D. Ribosome synthesis in Saccharomyces cerevisiae. *Annu Rev Genet* **33**, 261-311, doi:10.1146/annurev.genet.33.1.261 (1999).
78 Fromont-Racine, M., Senger, B., Saveanu, C. & Fasiolo, F. Ribosome assembly in eukaryotes. *Gene* **313**, 17-42, doi:10.1016/s0378-1119(03)00629-2 (2003).
79 Robinow, C. & Kellenberger, E. The bacterial nucleoid revisited. *Microbiol Rev* **58**, 211-232 (1994).
80 Bernstein, J. A., Khodursky, A. B., Lin, P. H., Lin-Chao, S. & Cohen, S. N. Global analysis of mRNA decay and abundance in Escherichia coli at single-gene resolution using two-color fluorescent DNA microarrays. *Proc Natl Acad Sci U S A* **99**, 9697-9702, doi:10.1073/pnas.112318199 (2002).
81 Montero Llopis, P., Jackson, A. F., Sliusarenko, O., Surovtsev, I., Heinritz, J., Emonet, T. & Jacobs-Wagner, C. Spatial organization of the flow of genetic information in bacteria. *Nature* **466**, 77-81, doi:10.1038/nature09152 (2010).
82 Bakshi, S., Siryaporn, A., Goulian, M. & Weisshaar, J. C. Superresolution imaging of ribosomes and RNA polymerase in live Escherichia coli cells. *Mol Microbiol* **85**, 21-38, doi:10.1111/j.1365-2958.2012.08081.x (2012).
83 Mondal, J., Bratton, B. P., Li, Y., Yethiraj, A. & Weisshaar, J. C. Entropy-based mechanism of ribosome-nucleoid segregation in E. coli cells. *Biophys J* **100**, 2605-2613, doi:10.1016/j.bpj.2011.04.030 (2011).
84 Woldringh, C. L. The role of co-transcriptional translation and protein translocation (transertion) in bacterial chromosome segregation. *Mol Microbiol* **45**, 17-29, doi:10.1046/j.1365-2958.2002.02993.x (2002).
85 Pace, N. R. Structure and synthesis of the ribosomal ribonucleic acid of prokaryotes. *Bacteriol Rev* **37**, 562-603 (1973).
86 Hamkalo, B. A. & Miller, O. L., Jr. Electronmicroscopy of genetic activity. *Annu Rev Biochem* **42**, 379-396, doi:10.1146/annurev.bi.42.070173.002115 (1973).
87 Kiss, A., Sain, B. & Venetianer, P. The number of rRNA genes in Escherichia coli. *FEBS Lett* **79**, 77-79, doi:10.1016/0014-5793(77)80354-2 (1977).
88 Williamson, J. R. After the ribosome structures: how are the subunits assembled? *RNA* **9**, 165-167, doi:10.1261/rna.2164903 (2003).

89 Hayes, F. & Vasseur, M. Processing of the 17-S Escherichia coli precursor RNA in the 27-S pre-ribosomal particle. *Eur J Biochem* **61**, 433-442, doi:10.1111/j.1432-1033.1976.tb10037.x (1976).
90 Bennison, D. J., Irving, S. E. & Corrigan, R. M. The Impact of the Stringent Response on TRAFAC GTPases and Prokaryotic Ribosome Assembly. *Cells* **8**, doi:10.3390/cells8111313 (2019).
91 Bram, R. J., Young, R. A. & Steitz, J. A. The ribonuclease III site flanking 23S sequences in the 30S ribosomal precursor RNA of E. coli. *Cell* **19**, 393-401, doi:10.1016/0092-8674(80)90513-9 (1980).
92 Liiv, A. & Remme, J. Importance of transient structures during post-transcriptional refolding of the pre-23S rRNA and ribosomal large subunit assembly. *J Mol Biol* **342**, 725-741, doi:10.1016/j.jmb.2004.07.082 (2004).
93 Young, R. A. & Steitz, J. A. Complementary sequences 1700 nucleotides apart form a ribonuclease III cleavage site in Escherichia coli ribosomal precursor RNA. *Proc Natl Acad Sci U S A* **75**, 3593-3597, doi:10.1073/pnas.75.8.3593 (1978).
94 Sirdeshmukh, R. & Schlessinger, D. Ordered processing of Escherichia coli 23S rRNA in vitro. *Nucleic Acids Res* **13**, 5041-5054, doi:10.1093/nar/13.14.5041 (1985).
95 Li, Z., Pandit, S. & Deutscher, M. P. Maturation of 23S ribosomal RNA requires the exoribonuclease RNase T. *RNA* **5**, 139-146, doi:10.1017/s1355838299981669 (1999).
96 Condon, C. Maturation and degradation of RNA in bacteria. *Curr Opin Microbiol* **10**, 271-278, doi:10.1016/j.mib.2007.05.008 (2007).
97 Misra, T. K. & Apirion, D. RNase E, an RNA processing enzyme from Escherichia coli. *J Biol Chem* **254**, 11154-11159 (1979).
98 Li, Z., Pandit, S. & Deutscher, M. P. RNase G (CafA protein) and RNase E are both required for the 5' maturation of 16S ribosomal RNA. *EMBO J* **18**, 2878-2885, doi:10.1093/emboj/18.10.2878 (1999).
99 Vercruysse, M., Kohrer, C., Shen, Y., Proulx, S., Ghosal, A., Davies, B. W., . . . Walker, G. C. Identification of YbeY-Protein Interactions Involved in 16S rRNA Maturation and Stress Regulation in Escherichia coli. *MBio* **7**, doi:10.1128/mBio.01785-16 (2016).
100 Sulthana, S. & Deutscher, M. P. Multiple exoribonucleases catalyze maturation of the 3' terminus of 16S ribosomal RNA (rRNA). *J Biol Chem* **288**, 12574-12579, doi:10.1074/jbc.C113.459172 (2013).
101 Roy, M. K., Singh, B., Ray, B. K. & Apirion, D. Maturation of 5-S rRNA: ribonuclease E cleavages and their dependence on precursor sequences. *Eur J Biochem* **131**, 119-127, doi:10.1111/j.1432-1033.1983.tb07238.x (1983).
102 Li, Z. & Deutscher, M. P. The tRNA processing enzyme RNase T is essential for maturation of 5S RNA. *Proc Natl Acad Sci U S A* **92**, 6883-6886, doi:10.1073/pnas.92.15.6883 (1995).
103 Deutscher, M. P. Maturation and degradation of ribosomal RNA in bacteria. *Prog Mol Biol Transl Sci* **85**, 369-391, doi:10.1016/S0079-6603(08)00809-X (2009).
104 Limbach, P. A., Crain, P. F. & McCloskey, J. A. Summary: the modified nucleosides of RNA. *Nucleic Acids Res* **22**, 2183-2196, doi:10.1093/nar/22.12.2183 (1994).
105 Bakin, A. & Ofengand, J. Four newly located pseudouridylate residues in Escherichia coli 23S ribosomal RNA are all at the peptidyltransferase center: analysis by the application of a new sequencing technique. *Biochemistry* **32**, 9754-9762, doi:10.1021/bi00088a030 (1993).
106 Bakin, A., Kowalak, J. A., McCloskey, J. A. & Ofengand, J. The single pseudouridine residue in Escherichia coli 16S RNA is located at position 516. *Nucleic Acids Res* **22**, 3681-3684, doi:10.1093/nar/22.18.3681 (1994).

107 Kowalak, J. A., Bruenger, E. & McCloskey, J. A. Posttranscriptional modification of the central loop of domain V in Escherichia coli 23 S ribosomal RNA. *J Biol Chem* **270**, 17758-17764, doi:10.1074/jbc.270.30.17758 (1995).
108 Andersen, T. E., Porse, B. T. & Kirpekar, F. A novel partial modification at C2501 in Escherichia coli 23S ribosomal RNA. *RNA* **10**, 907-913, doi:10.1261/rna.5259404 (2004).
109 Brimacombe, R., Mitchell, P., Osswald, M., Stade, K. & Bochkariov, D. Clustering of modified nucleotides at the functional center of bacterial ribosomal RNA. *FASEB J* **7**, 161-167, doi:10.1096/fasebj.7.1.8422963 (1993).
110 Cunningham, P. R., Richard, R. B., Weitzmann, C. J., Nurse, K. & Ofengand, J. The absence of modified nucleotides affects both in vitro assembly and in vitro function of the 30S ribosomal subunit of Escherichia coli. *Biochimie* **73**, 789-796, doi:10.1016/0300-9084(91)90058-9 (1991).
111 Green, R. & Noller, H. F. In vitro complementation analysis localizes 23S rRNA posttranscriptional modifications that are required for Escherichia coli 50S ribosomal subunit assembly and function. *RNA* **2**, 1011-1021 (1996).
112 Wagner, R. (2001).
113 Chen, R., Brosius, J. & Wittmann-Liebold, B. Occurrence of methylated amino acids as N-termini of proteins from Escherichia coli ribosomes. *J Mol Biol* **111**, 173-181, doi:10.1016/s0022-2836(77)80121-6 (1977).
114 Lhoest, J. & Colson, C. Genetics of ribosomal protein methylation in Escherichia coli. II. A mutant lacking a new type of methylated amino acid, N5-methylglutamine, in protein L3. *Mol Gen Genet* **154**, 175-180, doi:10.1007/bf00330833 (1977).
115 Muranova, T. A., Muranov, A. V., Markova, L. F. & Ovchinnikov, Y. A. The primary structure of ribosomal protein L3 from Escherichia coli 70 S ribosomes. *FEBS Lett* **96**, 301-305, doi:10.1016/0014-5793(78)80423-2 (1978).
116 Chang, F. N. Temperature-dependent variation in the extent of methylation of ribosomal proteins L7 and L12 in Escherichia coli. *J Bacteriol* **135**, 1165-1166 (1978).
117 Brosius, J. & Chen, R. The primary structure of protein L16 located at the peptidyltransferase center of Escherichia coli ribosomes. *FEBS Lett* **68**, 105-109, doi:10.1016/0014-5793(76)80415-2 (1976).
118 Chang, C. N., Schwartz, M. & Chang, F. N. Identification and characterization of a new methylated amino acid in ribosomal protein L33 of Escherichia coli. *Biochem Biophys Res Commun* **73**, 233-239, doi:10.1016/0006-291x(76)90698-7 (1976).
119 Wittmann-Liebold, B. & Greuer, B. The primary structure of protein S5 from the small subunit of the Escherichia coli ribosome. *FEBS Lett* **95**, 91-98, doi:10.1016/0014-5793(78)80059-3 (1978).
120 Yaguchi, M. Primary structure of protein S18 from the small Escherichia coli ribosomal subunit. *FEBS Lett* **59**, 217-220, doi:10.1016/0014-5793(75)80378-4 (1975).
121 Terhorst, C., Moller, W., Laursen, R. & Wittmann-Liebold, B. The primary structure of an acidic protein from 50-S ribosomes of Escherichia coli which is involved in GTP hydrolysis dependent on elongation factors G and T. *Eur J Biochem* **34**, 138-152, doi:10.1111/j.1432-1033.1973.tb02740.x (1973).
122 Tanaka, S., Matsushita, Y., Yoshikawa, A. & Isono, K. Cloning and molecular characterization of the gene rimL which encodes an enzyme acetylating ribosomal protein L12 of Escherichia coli K12. *Mol Gen Genet* **217**, 289-293, doi:10.1007/bf02464895 (1989).
123 Fontecave, M., Mulliez, E. & Atta, M. New light on methylthiolation reactions. *Chem Biol* **15**, 209-210, doi:10.1016/j.chembiol.2008.02.011 (2008).
124 Reeh, S. & Pedersen, S. Post-translational modification of Escherichia coli ribosomal protein S6. *Mol Gen Genet* **173**, 183-187, doi:10.1007/bf00330309 (1979).

125 Arnold, R. J. & Reilly, J. P. Observation of Escherichia coli ribosomal proteins and their posttranslational modifications by mass spectrometry. *Anal Biochem* **269**, 105-112, doi:10.1006/abio.1998.3077 (1999).
126 Adams, J. M. & Capecchi, M. R. N-formylmethionyl-sRNA as the initiator of protein synthesis. *Proc Natl Acad Sci U S A* **55**, 147-155, doi:10.1073/pnas.55.1.147 (1966).
127 Nesterchuk, M. V., Sergiev, P. V. & Dontsova, O. A. Posttranslational Modifications of Ribosomal Proteins in Escherichia coli. *Acta Naturae* **3**, 22-33 (2011).
128 Ben-Bassat, A., Bauer, K., Chang, S. Y., Myambo, K., Boosman, A. & Chang, S. Processing of the initiation methionine from proteins: properties of the Escherichia coli methionine aminopeptidase and its gene structure. *J Bacteriol* **169**, 751-757, doi:10.1128/jb.169.2.751-757.1987 (1987).
129 Aseev, L. V. & Boni, I. V. [Extraribosomal functions of bacterial ribosomal proteins]. *Mol Biol (Mosk)* **45**, 805-816 (2011).
130 Traub, P. & Nomura, M. Structure and function of E. coli ribosomes. V. Reconstitution of functionally active 30S ribosomal particles from RNA and proteins. *Proc Natl Acad Sci U S A* **59**, 777-784, doi:10.1073/pnas.59.3.777 (1968).
131 Held, W. A., Mizushima, S. & Nomura, M. Reconstitution of Escherichia coli 30 S ribosomal subunits from purified molecular components. *J Biol Chem* **248**, 5720-5730 (1973).
132 Culver, G. M. & Noller, H. F. Efficient reconstitution of functional Escherichia coli 30S ribosomal subunits from a complete set of recombinant small subunit ribosomal proteins. *RNA* **5**, 832-843, doi:10.1017/s1355838299990714 (1999).
133 Rohl, R. & Nierhaus, K. H. Assembly map of the large subunit (50S) of Escherichia coli ribosomes. *Proc Natl Acad Sci U S A* **79**, 729-733, doi:10.1073/pnas.79.3.729 (1982).
134 Herold, M. & Nierhaus, K. H. Incorporation of six additional proteins to complete the assembly map of the 50 S subunit from Escherichia coli ribosomes. *J Biol Chem* **262**, 8826-8833 (1987).
135 Lindahl, L. Intermediates and time kinetics of the in vivo assembly of Escherichia coli ribosomes. *J Mol Biol* **92**, 15-37 (1975).
136 Duss, O., Stepanyuk, G. A., Grot, A., O'Leary, S. E., Puglisi, J. D. & Williamson, J. R. Real-time assembly of ribonucleoprotein complexes on nascent RNA transcripts. *Nat Commun* **9**, 5087, doi:10.1038/s41467-018-07423-3 (2018).
137 Gausing, K. Ribosomal protein in E. coli: rate of synthesis and pool size at different growth rates. *Mol Gen Genet* **129**, 61-75, doi:10.1007/bf00269266 (1974).
138 Guthrie, C., Nashimoto, H. & Nomura, M. Structure and function of E. coli ribosomes. 8. Cold-sensitive mutants defective in ribosome assembly. *Proc Natl Acad Sci U S A* **63**, 384-391, doi:10.1073/pnas.63.2.384 (1969).
139 Nashimoto, H., Held, W., Kaltschmidt, E. & Nomura, M. Structure and function of bacterial ribosomes. XII. Accumulation of 21 s particles by some cold-sensitive mutants of Escherichia coli. *J Mol Biol* **62**, 121-138, doi:10.1016/0022-2836(71)90135-5 (1971).
140 Alix, J. H. & Guerin, M. F. Mutant DnaK chaperones cause ribosome assembly defects in Escherichia coli. *Proc Natl Acad Sci U S A* **90**, 9725-9729, doi:10.1073/pnas.90.20.9725 (1993).
141 Mangiarotti, G., Apirion, D., Schlessinger, D. & Silengo, L. Biosynthetic precursors of 30S and 50S ribosomal particles in Escherichia coli. *Biochemistry* **7**, 456-472, doi:10.1021/bi00841a058 (1968).
142 Sykes, M. T., Shajani, Z., Sperling, E., Beck, A. H. & Williamson, J. R. Quantitative proteomic analysis of ribosome assembly and turnover in vivo. *J Mol Biol* **403**, 331-345, doi:10.1016/j.jmb.2010.08.005 (2010).

143 Chen, S. S. & Williamson, J. R. Characterization of the ribosome biogenesis landscape in E. coli using quantitative mass spectrometry. *J Mol Biol* **425**, 767-779, doi:10.1016/j.jmb.2012.11.040 (2013).
144 Mulder, A. M., Yoshioka, C., Beck, A. H., Bunner, A. E., Milligan, R. A., Potter, C. S., . . . Williamson, J. R. Visualizing ribosome biogenesis: parallel assembly pathways for the 30S subunit. *Science* **330**, 673-677, doi:10.1126/science.1193220 (2010).
145 Bunner, A. E., Nord, S., Wikstrom, P. M. & Williamson, J. R. The effect of ribosome assembly cofactors on in vitro 30S subunit reconstitution. *J Mol Biol* **398**, 1-7, doi:10.1016/j.jmb.2010.02.036 (2010).
146 Britton, R. A. Role of GTPases in bacterial ribosome assembly. *Annu Rev Microbiol* **63**, 155-176, doi:10.1146/annurev.micro.091208.073225 (2009).
147 Warner, J. R. Twenty years of ribosome assembly and ribosomopathies. *RNA* **21**, 758-759, doi:10.1261/rna.050435.115 (2015).
148 Jiang, M., Sullivan, S. M., Walker, A. K., Strahler, J. R., Andrews, P. C. & Maddock, J. R. Identification of novel Escherichia coli ribosome-associated proteins using isobaric tags and multidimensional protein identification techniques. *J Bacteriol* **189**, 3434-3444, doi:10.1128/JB.00090-07 (2007).
149 Hage, A. E. & Tollervey, D. A surfeit of factors: why is ribosome assembly so much more complicated in eukaryotes than bacteria? *RNA Biol* **1**, 10-15 (2004).
150 Connolly, K. & Culver, G. Deconstructing ribosome construction. *Trends Biochem Sci* **34**, 256-263, doi:10.1016/j.tibs.2009.01.011 (2009).
151 Bunner, A. E., Beck, A. H. & Williamson, J. R. Kinetic cooperativity in Escherichia coli 30S ribosomal subunit reconstitution reveals additional complexity in the assembly landscape. *Proc Natl Acad Sci U S A* **107**, 5417-5422, doi:10.1073/pnas.0912007107 (2010).
152 Guo, Q., Goto, S., Chen, Y., Feng, B., Xu, Y., Muto, A., . . . Gao, N. Dissecting the in vivo assembly of the 30S ribosomal subunit reveals the role of RimM and general features of the assembly process. *Nucleic Acids Res* **41**, 2609-2620, doi:10.1093/nar/gks1256 (2013).
153 Davis, J. H., Tan, Y. Z., Carragher, B., Potter, C. S., Lyumkis, D. & Williamson, J. R. Modular Assembly of the Bacterial Large Ribosomal Subunit. *Cell* **167**, 1610-1622 e1615, doi:10.1016/j.cell.2016.11.020 (2016).
154 Kargas, V., Castro-Hartmann, P., Escudero-Urquijo, N., Dent, K., Hilcenko, C., Sailer, C., . . . Warren, A. J. Mechanism of completion of peptidyltransferase centre assembly in eukaryotes. *Elife* **8**, doi:10.7554/eLife.44904 (2019).
155 Zhou, Y., Musalgaonkar, S., Johnson, A. W. & Taylor, D. W. Tightly-orchestrated rearrangements govern catalytic center assembly of the ribosome. *Nat Commun* **10**, 958, doi:10.1038/s41467-019-08880-0 (2019).
156 Nikolay, R., Hilal, T., Qin, B., Mielke, T., Burger, J., Loerke, J., . . . Spahn, C. M. T. Structural Visualization of the Formation and Activation of the 50S Ribosomal Subunit during In Vitro Reconstitution. *Mol Cell* **70**, 881-893 e883, doi:10.1016/j.molcel.2018.05.003 (2018).
157 Arai, T., Ishiguro, K., Kimura, S., Sakaguchi, Y., Suzuki, T. & Suzuki, T. Single methylation of 23S rRNA triggers late steps of 50S ribosomal subunit assembly. *Proc Natl Acad Sci U S A* **112**, E4707-4716, doi:10.1073/pnas.1506749112 (2015).
158 Jomaa, A., Jain, N., Davis, J. H., Williamson, J. R., Britton, R. A. & Ortega, J. Functional domains of the 50S subunit mature late in the assembly process. *Nucleic Acids Res* **42**, 3419-3435, doi:10.1093/nar/gkt1295 (2014).
159 Ni, X., Davis, J. H., Jain, N., Razi, A., Benlekbir, S., McArthur, A. G., . . . Ortega, J. YphC and YsxC GTPases assist the maturation of the central protuberance, GTPase associated

region and functional core of the 50S ribosomal subunit. *Nucleic Acids Res* **44**, 8442-8455, doi:10.1093/nar/gkw678 (2016).

160 Li, N., Chen, Y., Guo, Q., Zhang, Y., Yuan, Y., Ma, C., . . . Gao, N. Cryo-EM structures of the late-stage assembly intermediates of the bacterial 50S ribosomal subunit. *Nucleic Acids Res* **41**, 7073-7083, doi:10.1093/nar/gkt423 (2013).

161 Wout, P., Pu, K., Sullivan, S. M., Reese, V., Zhou, S., Lin, B. & Maddock, J. R. The Escherichia coli GTPase CgtAE cofractionates with the 50S ribosomal subunit and interacts with SpoT, a ppGpp synthetase/hydrolase. *J Bacteriol* **186**, 5249-5257, doi:10.1128/JB.186.16.5249-5257.2004 (2004).

162 Schaefer, L., Uicker, W. C., Wicker-Planquart, C., Foucher, A. E., Jault, J. M. & Britton, R. A. Multiple GTPases participate in the assembly of the large ribosomal subunit in Bacillus subtilis. *J Bacteriol* **188**, 8252-8258, doi:10.1128/JB.01213-06 (2006).

163 Nicol, S. M. & Fuller-Pace, F. V. The "DEAD box" protein DbpA interacts specifically with the peptidyltransferase center in 23S rRNA. *Proc Natl Acad Sci U S A* **92**, 11681-11685, doi:10.1073/pnas.92.25.11681 (1995).

164 Sharpe Elles, L. M., Sykes, M. T., Williamson, J. R. & Uhlenbeck, O. C. A dominant negative mutant of the E. coli RNA helicase DbpA blocks assembly of the 50S ribosomal subunit. *Nucleic Acids Res* **37**, 6503-6514, doi:10.1093/nar/gkp711 (2009).

165 Hardin, J. W., Hu, Y. X. & McKay, D. B. Structure of the RNA binding domain of a DEAD-box helicase bound to its ribosomal RNA target reveals a novel mode of recognition by an RNA recognition motif. *J Mol Biol* **402**, 412-427, doi:10.1016/j.jmb.2010.07.040 (2010).

166 Peil, L., Virumae, K. & Remme, J. Ribosome assembly in Escherichia coli strains lacking the RNA helicase DeaD/CsdA or DbpA. *FEBS J* **275**, 3772-3782, doi:10.1111/j.1742-4658.2008.06523.x (2008).

167 Zhang, X., Yan, K., Zhang, Y., Li, N., Ma, C., Li, Z., . . . Gao, N. Structural insights into the function of a unique tandem GTPase EngA in bacterial ribosome assembly. *Nucleic Acids Res* **42**, 13430-13439, doi:10.1093/nar/gku1135 (2014).

168 Majumdar, S., Acharya, A., Tomar, S. K. & Prakash, B. Disrupting domain-domain interactions is indispensable for EngA-ribosome interactions. *Biochim Biophys Acta Proteins Proteom* **1865**, 289-303, doi:10.1016/j.bbapap.2016.12.005 (2017).

169 Feng, B., Mandava, C. S., Guo, Q., Wang, J., Cao, W., Li, N., . . . Gao, N. Structural and functional insights into the mode of action of a universally conserved Obg GTPase. *PLoS Biol* **12**, e1001866, doi:10.1371/journal.pbio.1001866 (2014).

170 Adams, A., Lindahl, T. & Fresco, J. R. Conformational differences between the biologically active and inactive forms of a transfer ribonucleic acid. *Proc Natl Acad Sci U S A* **57**, 1684-1691, doi:10.1073/pnas.57.6.1684 (1967).

171 Crothers, D. M., Cole, P. E., Hilbers, C. W. & Shulman, R. G. The molecular mechanism of thermal unfolding of Escherichia coli formylmethionine transfer RNA. *J Mol Biol* **87**, 63-88, doi:10.1016/0022-2836(74)90560-9 (1974).

172 Woodson, S. A. Recent insights on RNA folding mechanisms from catalytic RNA. *Cell Mol Life Sci* **57**, 796-808, doi:10.1007/s000180050042 (2000).

173 Talkington, M. W., Siuzdak, G. & Williamson, J. R. An assembly landscape for the 30S ribosomal subunit. *Nature* **438**, 628-632, doi:10.1038/nature04261 (2005).

174 Herschlag, D. RNA chaperones and the RNA folding problem. *J Biol Chem* **270**, 20871-20874, doi:10.1074/jbc.270.36.20871 (1995).

175 Lorsch, J. R. RNA chaperones exist and DEAD box proteins get a life. *Cell* **109**, 797-800, doi:10.1016/s0092-8674(02)00804-8 (2002).

176 Jarmoskaite, I. & Russell, R. DEAD-box proteins as RNA helicases and chaperones. *Wiley Interdiscip Rev RNA* **2**, 135-152, doi:10.1002/wrna.50 (2011).

177 Rocak, S. & Linder, P. DEAD-box proteins: the driving forces behind RNA metabolism. *Nat Rev Mol Cell Biol* **5**, 232-241, doi:10.1038/nrm1335 (2004).
178 Tanner, N. K., Cordin, O., Banroques, J., Doere, M. & Linder, P. The Q motif: a newly identified motif in DEAD box helicases may regulate ATP binding and hydrolysis. *Mol Cell* **11**, 127-138, doi:10.1016/s1097-2765(03)00006-6 (2003).
179 Cordin, O., Banroques, J., Tanner, N. K. & Linder, P. The DEAD-box protein family of RNA helicases. *Gene* **367**, 17-37, doi:10.1016/j.gene.2005.10.019 (2006).
180 Linder, P. Dead-box proteins: a family affair--active and passive players in RNP-remodeling. *Nucleic Acids Res* **34**, 4168-4180, doi:10.1093/nar/gkl468 (2006).
181 Tanner, N. K. & Linder, P. DExD/H box RNA helicases: from generic motors to specific dissociation functions. *Mol Cell* **8**, 251-262, doi:10.1016/s1097-2765(01)00329-x (2001).
182 Fuller-Pace, F. V., Nicol, S. M., Reid, A. D. & Lane, D. P. DbpA: a DEAD box protein specifically activated by 23s rRNA. *EMBO J* **12**, 3619-3626 (1993).
183 Pugh, G. E., Nicol, S. M. & Fuller-Pace, F. V. Interaction of the Escherichia coli DEAD box protein DbpA with 23 S ribosomal RNA. *J Mol Biol* **292**, 771-778, doi:10.1006/jmbi.1999.3112 (1999).
184 Tsu, C. A., Kossen, K. & Uhlenbeck, O. C. The Escherichia coli DEAD protein DbpA recognizes a small RNA hairpin in 23S rRNA. *RNA* **7**, 702-709, doi:10.1017/s1355838201010135 (2001).
185 Silverman, E., Edwalds-Gilbert, G. & Lin, R. J. DExD/H-box proteins and their partners: helping RNA helicases unwind. *Gene* **312**, 1-16, doi:10.1016/s0378-1119(03)00626-7 (2003).
186 Baba, T., Ara, T., Hasegawa, M., Takai, Y., Okumura, Y., Baba, M., . . . Mori, H. Construction of Escherichia coli K-12 in-frame, single-gene knockout mutants: the Keio collection. *Mol Syst Biol* **2**, 2006 0008, doi:10.1038/msb4100050 (2006).
187 Elles, L. M. & Uhlenbeck, O. C. Mutation of the arginine finger in the active site of Escherichia coli DbpA abolishes ATPase and helicase activity and confers a dominant slow growth phenotype. *Nucleic Acids Res* **36**, 41-50, doi:10.1093/nar/gkm926 (2008).
188 Gentry, R. C., Childs, J. J., Gevorkyan, J., Gerasimova, Y. V. & Koculi, E. Time course of large ribosomal subunit assembly in E. coli cells overexpressing a helicase inactive DbpA protein. *RNA* **22**, 1055-1064, doi:10.1261/rna.055137.115 (2016).
189 Tsu, C. A. & Uhlenbeck, O. C. Kinetic analysis of the RNA-dependent adenosinetriphosphatase activity of DbpA, an Escherichia coli DEAD protein specific for 23S ribosomal RNA. *Biochemistry* **37**, 16989-16996, doi:10.1021/bi981837y (1998).
190 Yusupov, M. M., Yusupova, G. Z., Baucom, A., Lieberman, K., Earnest, T. N., Cate, J. H. & Noller, H. F. Crystal structure of the ribosome at 5.5 A resolution. *Science* **292**, 883-896, doi:10.1126/science.1060089 (2001).
191 Verstraeten, N., Fauvart, M., Versees, W. & Michiels, J. The universally conserved prokaryotic GTPases. *Microbiol Mol Biol Rev* **75**, 507-542, second and third pages of table of contents, doi:10.1128/MMBR.00009-11 (2011).
192 Leipe, D. D., Wolf, Y. I., Koonin, E. V. & Aravind, L. Classification and evolution of P-loop GTPases and related ATPases. *J Mol Biol* **317**, 41-72, doi:10.1006/jmbi.2001.5378 (2002).
193 Walker, J. E., Saraste, M., Runswick, M. J. & Gay, N. J. Distantly related sequences in the alpha- and beta-subunits of ATP synthase, myosin, kinases and other ATP-requiring enzymes and a common nucleotide binding fold. *EMBO J* **1**, 945-951 (1982).
194 Wittinghofer, A. & Vetter, I. R. Structure-function relationships of the G domain, a canonical switch motif. *Annu Rev Biochem* **80**, 943-971, doi:10.1146/annurev-biochem-062708-134043 (2011).

195 delToro, D., Ortiz, D., Ordyan, M., Sippy, J., Oh, C. S., Keller, N., . . . Smith, D. E. Walker-A Motif Acts to Coordinate ATP Hydrolysis with Motor Output in Viral DNA Packaging. *J Mol Biol* **428**, 2709-2729, doi:10.1016/j.jmb.2016.04.029 (2016).

196 Carvalho, A. T., Szeler, K., Vavitsas, K., Aqvist, J. & Kamerlin, S. C. Modeling the mechanisms of biological GTP hydrolysis. *Arch Biochem Biophys* **582**, 80-90, doi:10.1016/j.abb.2015.02.027 (2015).

197 Daumke, O. & Praefcke, G. J. Invited review: Mechanisms of GTP hydrolysis and conformational transitions in the dynamin superfamily. *Biopolymers* **105**, 580-593, doi:10.1002/bip.22855 (2016).

198 Foti, J. J., Persky, N. S., Ferullo, D. J. & Lovett, S. T. Chromosome segregation control by Escherichia coli ObgE GTPase. *Mol Microbiol* **65**, 569-581, doi:10.1111/j.1365-2958.2007.05811.x (2007).

199 Kobayashi, G., Moriya, S. & Wada, C. Deficiency of essential GTP-binding protein ObgE in Escherichia coli inhibits chromosome partition. *Mol Microbiol* **41**, 1037-1051, doi:10.1046/j.1365-2958.2001.02574.x (2001).

200 Scott, J. M. & Haldenwang, W. G. Obg, an essential GTP binding protein of Bacillus subtilis, is necessary for stress activation of transcription factor sigma(B). *J Bacteriol* **181**, 4653-4660 (1999).

201 Gkekas, S., Singh, R. K., Shkumatov, A. V., Messens, J., Fauvart, M., Verstraeten, N., . . . Versees, W. Structural and biochemical analysis of Escherichia coli ObgE, a central regulator of bacterial persistence. *J Biol Chem* **292**, 5871-5883, doi:10.1074/jbc.M116.761809 (2017).

202 Foti, J. J., Schienda, J., Sutera, V. A., Jr. & Lovett, S. T. A bacterial G protein-mediated response to replication arrest. *Mol Cell* **17**, 549-560, doi:10.1016/j.molcel.2005.01.012 (2005).

203 Kok, J., Trach, K. A. & Hoch, J. A. Effects on Bacillus subtilis of a conditional lethal mutation in the essential GTP-binding protein Obg. *J Bacteriol* **176**, 7155-7160, doi:10.1128/jb.176.23.7155-7160.1994 (1994).

204 Vidwans, S. J., Ireton, K. & Grossman, A. D. Possible role for the essential GTP-binding protein Obg in regulating the initiation of sporulation in Bacillus subtilis. *J Bacteriol* **177**, 3308-3311, doi:10.1128/jb.177.11.3308-3311.1995 (1995).

205 Persky, N. S., Ferullo, D. J., Cooper, D. L., Moore, H. R. & Lovett, S. T. The ObgE/CgtA GTPase influences the stringent response to amino acid starvation in Escherichia coli. *Mol Microbiol* **73**, 253-266, doi:10.1111/j.1365-2958.2009.06767.x (2009).

206 Datta, K., Skidmore, J. M., Pu, K. & Maddock, J. R. The Caulobacter crescentus GTPase CgtAC is required for progression through the cell cycle and for maintaining 50S ribosomal subunit levels. *Mol Microbiol* **54**, 1379-1392, doi:10.1111/j.1365-2958.2004.04354.x (2004).

207 Jiang, M., Datta, K., Walker, A., Strahler, J., Bagamasbad, P., Andrews, P. C. & Maddock, J. R. The Escherichia coli GTPase CgtAE is involved in late steps of large ribosome assembly. *J Bacteriol* **188**, 6757-6770, doi:10.1128/JB.00444-06 (2006).

208 Sato, A., Kobayashi, G., Hayashi, H., Yoshida, H., Wada, A., Maeda, M., . . . Wada, C. The GTP binding protein Obg homolog ObgE is involved in ribosome maturation. *Genes Cells* **10**, 393-408, doi:10.1111/j.1365-2443.2005.00851.x (2005).

209 Scott, J. M., Ju, J., Mitchell, T. & Haldenwang, W. G. The Bacillus subtilis GTP binding protein obg and regulators of the sigma(B) stress response transcription factor cofractionate with ribosomes. *J Bacteriol* **182**, 2771-2777, doi:10.1128/jb.182.10.2771-2777.2000 (2000).

210 Tan, J., Jakob, U. & Bardwell, J. C. Overexpression of two different GTPases rescues a null mutation in a heat-induced rRNA methyltransferase. *J Bacteriol* **184**, 2692-2698, doi:10.1128/jb.184.10.2692-2698.2002 (2002).

211 Lin, B., Thayer, D. A. & Maddock, J. R. The Caulobacter crescentus CgtAC protein cosediments with the free 50S ribosomal subunit. *J Bacteriol* **186**, 481-489, doi:10.1128/jb.186.2.481-489.2004 (2004).

212 Kallstrom, G., Hedges, J. & Johnson, A. The putative GTPases Nog1p and Lsg1p are required for 60S ribosomal subunit biogenesis and are localized to the nucleus and cytoplasm, respectively. *Mol Cell Biol* **23**, 4344-4355, doi:10.1128/mcb.23.12.4344-4355.2003 (2003).

213 Dassain, M., Leroy, A., Colosetti, L., Carole, S. & Bouche, J. P. A new essential gene of the 'minimal genome' affecting cell division. *Biochimie* **81**, 889-895, doi:10.1016/s0300-9084(99)00207-2 (1999).

214 Morimoto, T., Loh, P. C., Hirai, T., Asai, K., Kobayashi, K., Moriya, S. & Ogasawara, N. Six GTP-binding proteins of the Era/Obg family are essential for cell growth in Bacillus subtilis. *Microbiology* **148**, 3539-3552, doi:10.1099/00221287-148-11-3539 (2002).

215 Pragai, Z. & Harwood, C. R. YsxC, a putative GTP-binding protein essential for growth of Bacillus subtilis 168. *J Bacteriol* **182**, 6819-6823, doi:10.1128/jb.182.23.6819-6823.2000 (2000).

216 Cooper, E. L., Garcia-Lara, J. & Foster, S. J. YsxC, an essential protein in Staphylococcus aureus crucial for ribosome assembly/stability. *BMC Microbiol* **9**, 266, doi:10.1186/1471-2180-9-266 (2009).

217 Hwang, J. & Inouye, M. An essential GTPase, der, containing double GTP-binding domains from Escherichia coli and Thermotoga maritima. *J Biol Chem* **276**, 31415-31421, doi:10.1074/jbc.M104455200 (2001).

218 Muench, S. P., Xu, L., Sedelnikova, S. E. & Rice, D. W. The essential GTPase YphC displays a major domain rearrangement associated with nucleotide binding. *Proc Natl Acad Sci U S A* **103**, 12359-12364, doi:10.1073/pnas.0602585103 (2006).

219 Robinson, V. L., Hwang, J., Fox, E., Inouye, M. & Stock, A. M. Domain arrangement of Der, a switch protein containing two GTPase domains. *Structure* **10**, 1649-1658, doi:10.1016/s0969-2126(02)00905-x (2002).

220 Mehr, I. J., Long, C. D., Serkin, C. D. & Seifert, H. S. A homologue of the recombination-dependent growth gene, rdgC, is involved in gonococcal pilin antigenic variation. *Genetics* **154**, 523-532 (2000).

221 Zalacain, M., Biswas, S., Ingraham, K. A., Ambrad, J., Bryant, A., Chalker, A. F., . . . Burnham, M. K. A global approach to identify novel broad-spectrum antibacterial targets among proteins of unknown function. *J Mol Microbiol Biotechnol* **6**, 109-126, doi:10.1159/000076741 (2003).

222 Tomar, S. K., Dhimole, N., Chatterjee, M. & Prakash, B. Distinct GDP/GTP bound states of the tandem G-domains of EngA regulate ribosome binding. *Nucleic Acids Res* **37**, 2359-2370, doi:10.1093/nar/gkp107 (2009).

223 Bharat, A., Jiang, M., Sullivan, S. M., Maddock, J. R. & Brown, E. D. Cooperative and critical roles for both G domains in the GTPase activity and cellular function of ribosome-associated Escherichia coli EngA. *J Bacteriol* **188**, 7992-7996, doi:10.1128/JB.00959-06 (2006).

224 Butland, G., Zhang, J. W., Yang, W., Sheung, A., Wong, P., Greenblatt, J. F., . . . Zamble, D. B. Interactions of the Escherichia coli hydrogenase biosynthetic proteins: HybG complex formation. *FEBS Lett* **580**, 677-681, doi:10.1016/j.febslet.2005.12.063 (2006).

225 Uicker, W. C., Schaefer, L. & Britton, R. A. The essential GTPase RbgA (YlqF) is required for 50S ribosome assembly in Bacillus subtilis. *Mol Microbiol* **59**, 528-540, doi:10.1111/j.1365-2958.2005.04948.x (2006).
226 Hwang, J. & Inouye, M. The tandem GTPase, Der, is essential for the biogenesis of 50S ribosomal subunits in Escherichia coli. *Mol Microbiol* **61**, 1660-1672, doi:10.1111/j.1365-2958.2006.05348.x (2006).
227 Shimomura, O., Johnson, F. H. & Saiga, Y. Extraction, purification and properties of aequorin, a bioluminescent protein from the luminous hydromedusan, Aequorea. *J Cell Comp Physiol* **59**, 223-239, doi:10.1002/jcp.1030590302 (1962).
228 Shimomura, O. A short story of aequorin. *Biol Bull* **189**, 1-5, doi:10.2307/1542194 (1995).
229 Shimomura, O. & Johnson, F. H. Properties of the bioluminescent protein aequorin. *Biochemistry* **8**, 3991-3997, doi:10.1021/bi00838a015 (1969).
230 Shimomura, O., Johnson, F. H. & Morise, H. Mechanism of the luminescent intramolecular reaction of aequorin. *Biochemistry* **13**, 3278-3286, doi:10.1021/bi00713a016 (1974).
231 Morise, H., Shimomura, O., Johnson, F. H. & Winant, J. Intermolecular energy transfer in the bioluminescent system of Aequorea. *Biochemistry* **13**, 2656-2662, doi:10.1021/bi00709a028 (1974).
232 Chalfie, M., Tu, Y., Euskirchen, G., Ward, W. W. & Prasher, D. C. Green fluorescent protein as a marker for gene expression. *Science* **263**, 802-805, doi:10.1126/science.8303295 (1994).
233 Heim, R., Prasher, D. C. & Tsien, R. Y. Wavelength mutations and posttranslational autoxidation of green fluorescent protein. *Proc Natl Acad Sci U S A* **91**, 12501-12504, doi:10.1073/pnas.91.26.12501 (1994).
234 Kricka, L. J. & Stanley, P. E. Scientists awarded Nobel Prize for work with GFP. *Luminescence* **24**, 1, doi:10.1002/bio.1113 (2009).
235 Ormo, M., Cubitt, A. B., Kallio, K., Gross, L. A., Tsien, R. Y. & Remington, S. J. Crystal structure of the Aequorea victoria green fluorescent protein. *Science* **273**, 1392-1395, doi:10.1126/science.273.5280.1392 (1996).
236 Yang, F., Moss, L. G. & Phillips, G. N., Jr. The molecular structure of green fluorescent protein. *Nat Biotechnol* **14**, 1246-1251, doi:10.1038/nbt1096-1246 (1996).
237 Cubitt, A. B., Heim, R., Adams, S. R., Boyd, A. E., Gross, L. A. & Tsien, R. Y. Understanding, improving and using green fluorescent proteins. *Trends Biochem Sci* **20**, 448-455, doi:10.1016/s0968-0004(00)89099-4 (1995).
238 Reid, B. G. & Flynn, G. C. Chromophore formation in green fluorescent protein. *Biochemistry* **36**, 6786-6791, doi:10.1021/bi970281w (1997).
239 Barondeau, D. P., Putnam, C. D., Kassmann, C. J., Tainer, J. A. & Getzoff, E. D. Mechanism and energetics of green fluorescent protein chromophore synthesis revealed by trapped intermediate structures. *Proc Natl Acad Sci U S A* **100**, 12111-12116, doi:10.1073/pnas.2133463100 (2003).
240 Chudakov, D. M., Matz, M. V., Lukyanov, S. & Lukyanov, K. A. Fluorescent proteins and their applications in imaging living cells and tissues. *Physiol Rev* **90**, 1103-1163, doi:10.1152/physrev.00038.2009 (2010).
241 Matz, M. V., Fradkov, A. F., Labas, Y. A., Savitsky, A. P., Zaraisky, A. G., Markelov, M. L. & Lukyanov, S. A. Fluorescent proteins from nonbioluminescent Anthozoa species. *Nat Biotechnol* **17**, 969-973, doi:10.1038/13657 (1999).
242 Icha, J., Weber, M., Waters, J. C. & Norden, C. Phototoxicity in live fluorescence microscopy, and how to avoid it. *Bioessays* **39**, doi:10.1002/bies.201700003 (2017).

243 Gross, L. A., Baird, G. S., Hoffman, R. C., Baldridge, K. K. & Tsien, R. Y. The structure of the chromophore within DsRed, a red fluorescent protein from coral. *Proc Natl Acad Sci U S A* **97**, 11990-11995, doi:10.1073/pnas.97.22.11990 (2000).
244 Bravaya, K. B., Subach, O. M., Korovina, N., Verkhusha, V. V. & Krylov, A. I. Insight into the common mechanism of the chromophore formation in the red fluorescent proteins: the elusive blue intermediate revealed. *J Am Chem Soc* **134**, 2807-2814, doi:10.1021/ja2114568 (2012).
245 Strack, R. L., Strongin, D. E., Mets, L., Glick, B. S. & Keenan, R. J. Chromophore formation in DsRed occurs by a branched pathway. *J Am Chem Soc* **132**, 8496-8505, doi:10.1021/ja1030084 (2010).
246 Shaner, N. C., Campbell, R. E., Steinbach, P. A., Giepmans, B. N., Palmer, A. E. & Tsien, R. Y. Improved monomeric red, orange and yellow fluorescent proteins derived from Discosoma sp. red fluorescent protein. *Nat Biotechnol* **22**, 1567-1572, doi:10.1038/nbt1037 (2004).
247 Vangindertael, J., Camacho, R., Sempels, W., Mizuno, H., Dedecker, P. & Janssen, K. P. F. An introduction to optical super-resolution microscopy for the adventurous biologist. *Methods Appl Fluoresc* **6**, 022003, doi:10.1088/2050-6120/aaae0c (2018).
248 Lavrentovich, O. D. in *Characterization of Materials* 1-15 (2012).
249 Abbe, E. Beiträge zur Theorie des Mikroskops und der mikroskopischen Wahrnehmung. *Archiv für Mikroskopische Anatomie* **9**, 413-468, doi:10.1007/BF02956173 (1873).
250 Huang, B., Bates, M. & Zhuang, X. Super-resolution fluorescence microscopy. *Annu Rev Biochem* **78**, 993-1016, doi:10.1146/annurev.biochem.77.061906.092014 (2009).
251 Ding, Y., Xi, P. & Ren, Q. Hacking the optical diffraction limit: Review on recent developments of fluorescence nanoscopy. *Chinese Science Bulletin* **56**, 1857, doi:10.1007/s11434-011-4502-3 (2011).
252 Heilemann, M., van de Linde, S., Schuttpelz, M., Kasper, R., Seefeldt, B., Mukherjee, A., . . . Sauer, M. Subdiffraction-resolution fluorescence imaging with conventional fluorescent probes. *Angew Chem Int Ed Engl* **47**, 6172-6176, doi:10.1002/anie.200802376 (2008).
253 Taniguchi, Y., Choi, P. J., Li, G. W., Chen, H., Babu, M., Hearn, J., . . . Xie, X. S. Quantifying E. coli proteome and transcriptome with single-molecule sensitivity in single cells. *Science* **329**, 533-538, doi:10.1126/science.1188308 (2010).
254 English, B. P., Hauryliuk, V., Sanamrad, A., Tankov, S., Dekker, N. H. & Elf, J. Single-molecule investigations of the stringent response machinery in living bacterial cells. *Proc Natl Acad Sci U S A* **108**, E365-373, doi:10.1073/pnas.1102255108 (2011).
255 Lee, S. F., Thompson, M. A., Schwartz, M. A., Shapiro, L. & Moerner, W. E. Super-resolution imaging of the nucleoid-associated protein HU in Caulobacter crescentus. *Biophys J* **100**, L31-33, doi:10.1016/j.bpj.2011.02.022 (2011).
256 Wang, W., Li, G. W., Chen, C., Xie, X. S. & Zhuang, X. Chromosome organization by a nucleoid-associated protein in live bacteria. *Science* **333**, 1445-1449, doi:10.1126/science.1204697 (2011).
257 Stracy, M., Lesterlin, C., Garza de Leon, F., Uphoff, S., Zawadzki, P. & Kapanidis, A. N. Live-cell superresolution microscopy reveals the organization of RNA polymerase in the bacterial nucleoid. *Proc Natl Acad Sci U S A* **112**, E4390-4399, doi:10.1073/pnas.1507592112 (2015).
258 Gustafsson, M. G. Surpassing the lateral resolution limit by a factor of two using structured illumination microscopy. *J Microsc* **198**, 82-87, doi:10.1046/j.1365-2818.2000.00710.x (2000).
259 Gustafsson, M. G., Shao, L., Carlton, P. M., Wang, C. J., Golubovskaya, I. N., Cande, W. Z., . . . Sedat, J. W. Three-dimensional resolution doubling in wide-field fluorescence

microscopy by structured illumination. *Biophys J* **94**, 4957-4970, doi:10.1529/biophysj.107.120345 (2008).
260 Lagrange, T., Reed, B., King, W., Kim, J. & Campbell, G. 71-97 (2012).
261 Weston, A., Armer, H. & Collinson, L. Towards native-state imaging in biological context in the electron microscope. *Journal of chemical biology* **3**, 101-112, doi:10.1007/s12154-009-0033-7 (2009).
262 Marton, L. Electron Microscopy of Biological Objects. *Nature* **133**, 911-911, doi:10.1038/133911b0 (1934).
263 Brenner, S. & Horne, R. W. A negative staining method for high resolution electron microscopy of viruses. *Biochim Biophys Acta* **34**, 103-110, doi:10.1016/0006-3002(59)90237-9 (1959).
264 Huxley, H. E. & Zubay, G. Preferential staining of nucleic acid-containing structures for electron microscopy. *J Biophys Biochem Cytol* **11**, 273-296, doi:10.1083/jcb.11.2.273 (1961).
265 Chaffey, N. Hayat MA. 2000. Principles and techniques of electron microscopy: biological applications. 4th edn. 543pp. Cambridge: Cambridge University Press. {pound}65 (hardback). *Annals of Botany*, doi:10.1006/anbo.2001.1367 (2001).
266 Fernandez-Moran, H. Low-temperature preparation techniques for electron microscopy of biological specimens based on rapid freezing with liquid helium II. *Ann N Y Acad Sci* **85**, 689-713, doi:10.1111/j.1749-6632.1960.tb49990.x (1960).
267 Adrian, M., Dubochet, J., Lepault, J. & McDowall, A. W. Cryo-electron microscopy of viruses. *Nature* **308**, 32-36, doi:10.1038/308032a0 (1984).
268 Knapek, E. & Dubochet, J. Beam damage to organic material is considerably reduced in cryo-electron microscopy. *J Mol Biol* **141**, 147-161, doi:10.1016/0022-2836(80)90382-4 (1980).
269 van Heel, M. & Frank, J. Use of multivariate statistics in analysing the images of biological macromolecules. *Ultramicroscopy* **6**, 187-194, doi:10.1016/0304-3991(81)90059-0 (1981).
270 Frank, J. & van Heel, M. Correspondence analysis of aligned images of biological particles. *J Mol Biol* **161**, 134-137, doi:10.1016/0022-2836(82)90282-0 (1982).
271 Frank, J., Radermacher, M., Penczek, P., Zhu, J., Li, Y., Ladjadj, M. & Leith, A. SPIDER and WEB: processing and visualization of images in 3D electron microscopy and related fields. *J Struct Biol* **116**, 190-199, doi:10.1006/jsbi.1996.0030 (1996).
272 Penczek, P. A., Grassucci, R. A. & Frank, J. The ribosome at improved resolution: new techniques for merging and orientation refinement in 3D cryo-electron microscopy of biological particles. *Ultramicroscopy* **53**, 251-270, doi:10.1016/0304-3991(94)90038-8 (1994).
273 Loerke, J., Giesebrecht, J. & Spahn, C. M. Multiparticle cryo-EM of ribosomes. *Methods Enzymol* **483**, 161-177, doi:10.1016/S0076-6879(10)83008-3 (2010).
274 Kuhlbrandt, W. Biochemistry. The resolution revolution. *Science* **343**, 1443-1444, doi:10.1126/science.1251652 (2014).
275 Bendory, T., Bartesaghi, A. & Singer, A. Single-particle cryo-electron microscopy: Mathematical theory, computational challenges, and opportunities. *arXiv e-prints* (2019). <https://ui.adsabs.harvard.edu/abs/2019arXiv190800574B>.
276 Oikonomou, C. M. & Jensen, G. J. The development of cryo-EM and how it has advanced microbiology. *Nat Microbiol* **2**, 1577-1579, doi:10.1038/s41564-017-0073-7 (2017).
277 Javed, A. & Orlova, E. V. Unravelling Ribosome Function Through Structural Studies. *Subcell Biochem* **93**, 53-81, doi:10.1007/978-3-030-28151-9_3 (2019).

278 Jordan, M. A. & Pigino, G. In situ cryo-electron tomography and subtomogram averaging of intraflagellar transport trains. *Methods Cell Biol* **152**, 179-195, doi:10.1016/bs.mcb.2019.04.005 (2019).
279 Afonina, Z. A. & Shirokov, V. A. Three-Dimensional Organization of Polyribosomes - A Modern Approach. *Biochemistry (Mosc)* **83**, S48-S55, doi:10.1134/S0006297918140055 (2018).
280 Pfeffer, S., Woellhaf, M. W., Herrmann, J. M. & Forster, F. Organization of the mitochondrial translation machinery studied in situ by cryoelectron tomography. *Nat Commun* **6**, 6019, doi:10.1038/ncomms7019 (2015).
281 Gold, V. A., Chroscicki, P., Bragoszewski, P. & Chacinska, A. Visualization of cytosolic ribosomes on the surface of mitochondria by electron cryo-tomography. *EMBO Rep* **18**, 1786-1800, doi:10.15252/embr.201744261 (2017).
282 Bugl, H., Fauman, E. B., Staker, B. L., Zheng, F., Kushner, S. R., Saper, M. A., . . . Jakob, U. RNA methylation under heat shock control. *Mol Cell* **6**, 349-360, doi:10.1016/s1097-2765(00)00035-6 (2000).
283 Nakashima, N. & Tamura, T. Conditional gene silencing of multiple genes with antisense RNAs and generation of a mutator strain of Escherichia coli. *Nucleic Acids Res* **37**, e103, doi:10.1093/nar/gkp498 (2009).
284 Nakashima, N., Tamura, T. & Good, L. Paired termini stabilize antisense RNAs and enhance conditional gene silencing in Escherichia coli. *Nucleic Acids Res* **34**, e138, doi:10.1093/nar/gkl697 (2006).
285 Verstraeten, N., Knapen, W. J., Kint, C. I., Liebens, V., Van den Bergh, B., Dewachter, L., . . . Michiels, J. Obg and Membrane Depolarization Are Part of a Microbial Bet-Hedging Strategy that Leads to Antibiotic Tolerance. *Mol Cell* **59**, 9-21, doi:10.1016/j.molcel.2015.05.011 (2015).
286 Blattner, F. R., Plunkett, G., 3rd, Bloch, C. A., Perna, N. T., Burland, V., Riley, M., . . . Shao, Y. The complete genome sequence of Escherichia coli K-12. *Science* **277**, 1453-1462, doi:10.1126/science.277.5331.1453 (1997).
287 Bohne, A. V. The nucleoid as a site of rRNA processing and ribosome assembly. *Front Plant Sci* **5**, 257, doi:10.3389/fpls.2014.00257 (2014).
288 Chai, Q., Singh, B., Peisker, K., Metzendorf, N., Ge, X., Dasgupta, S. & Sanyal, S. Organization of ribosomes and nucleoids in Escherichia coli cells during growth and in quiescence. *J Biol Chem* **289**, 11342-11352, doi:10.1074/jbc.M114.557348 (2014).
289 Bakshi, S., Choi, H., Mondal, J. & Weisshaar, J. C. Time-dependent effects of transcription- and translation-halting drugs on the spatial distributions of the Escherichia coli chromosome and ribosomes. *Mol Microbiol* **94**, 871-887, doi:10.1111/mmi.12805 (2014).
290 Nikolay, R., Schmidt, S., Schloemer, R., Deuerling, E. & Nierhaus, K. H. Ribosome Assembly as Antimicrobial Target. *Antibiotics (Basel)* **5**, doi:10.3390/antibiotics5020018 (2016).
291 Maguire, B. A. Inhibition of bacterial ribosome assembly: a suitable drug target? *Microbiol Mol Biol Rev* **73**, 22-35, doi:10.1128/MMBR.00030-08 (2009).
292 Nikolay, R., Schloemer, R., Schmidt, S., Mueller, S., Heubach, A. & Deuerling, E. Validation of a fluorescence-based screening concept to identify ribosome assembly defects in Escherichia coli. *Nucleic Acids Res* **42**, e100, doi:10.1093/nar/gku381 (2014).
293 Nikolay, R., Schloemer, R., Mueller, S. & Deuerling, E. Fluorescence-based monitoring of ribosome assembly landscapes. *BMC Mol Biol* **16**, 3, doi:10.1186/s12867-015-0031-y (2015).

294 Tenson, T. & Mankin, A. Antibiotics and the ribosome. *Mol Microbiol* **59**, 1664-1677, doi:10.1111/j.1365-2958.2006.05063.x (2006).
295 Wilson, D. N. The A-Z of bacterial translation inhibitors. *Crit Rev Biochem Mol Biol* **44**, 393-433, doi:10.3109/10409230903307311 (2009).
296 Stokes, J. M., Davis, J. H., Mangat, C. S., Williamson, J. R. & Brown, E. D. Discovery of a small molecule that inhibits bacterial ribosome biogenesis. *Elife* **3**, e03574, doi:10.7554/eLife.03574 (2014).
297 Stokes, J. M. & Brown, E. D. Chemical modulators of ribosome biogenesis as biological probes. *Nat Chem Biol* **11**, 924-932, doi:10.1038/nchembio.1957 (2015).
298 Schmidt, T. G. & Skerra, A. The Strep-tag system for one-step purification and high-affinity detection or capturing of proteins. *Nat Protoc* **2**, 1528-1535, doi:10.1038/nprot.2007.209 (2007).
299 Li, G. W., Burkhardt, D., Gross, C. & Weissman, J. S. Quantifying absolute protein synthesis rates reveals principles underlying allocation of cellular resources. *Cell* **157**, 624-635, doi:10.1016/j.cell.2014.02.033 (2014).
300 Popova, A. M. & Williamson, J. R. Quantitative analysis of rRNA modifications using stable isotope labeling and mass spectrometry. *J Am Chem Soc* **136**, 2058-2069, doi:10.1021/ja412084b (2014).
301 Hauser, R., Pech, M., Kijek, J., Yamamoto, H., Titz, B., Naeve, F., . . . Uetz, P. RsfA (YbeB) proteins are conserved ribosomal silencing factors. *PLoS Genet* **8**, e1002815, doi:10.1371/journal.pgen.1002815 (2012).
302 Dohme, F. & Nierhaus, K. H. Total reconstitution and assembly of 50 S subunits from Escherichia coli Ribosomes in vitro. *J Mol Biol* **107**, 585-599, doi:10.1016/s0022-2836(76)80085-x (1976).
303 Sieber, G. & Nierhaus, K. H. Kinetic and thermodynamic parameters of the assembly in vitro of the large subunit from Escherichia coli ribosomes. *Biochemistry* **17**, 3505-3511, doi:10.1021/bi00610a013 (1978).
304 Nierhaus, K. H. The assembly of prokaryotic ribosomes. *Biochimie* **73**, 739-755, doi:10.1016/0300-9084(91)90054-5 (1991).
305 Kint, C. I., Verstraeten, N., Wens, I., Liebens, V. R., Hofkens, J., Versees, W., . . . Michiels, J. The Escherichia coli GTPase ObgE modulates hydroxyl radical levels in response to DNA replication fork arrest. *FEBS J* **279**, 3692-3704, doi:10.1111/j.1742-4658.2012.08731.x (2012).
306 Choudhury, P. & Flower, A. M. Efficient assembly of ribosomes is inhibited by deletion of bipA in Escherichia coli. *J Bacteriol* **197**, 1819-1827, doi:10.1128/JB.00023-15 (2015).
307 Lerner, C. G. & Inouye, M. Pleiotropic changes resulting from depletion of Era, an essential GTP-binding protein in Escherichia coli. *Mol Microbiol* **5**, 951-957, doi:10.1111/j.1365-2958.1991.tb00770.x (1991).
308 Goh, S., Hohmeier, A., Stone, T. C., Offord, V., Sarabia, F., Garcia-Ruiz, C. & Good, L. Silencing of Essential Genes within a Highly Coordinated Operon in Escherichia coli. *Appl Environ Microbiol* **81**, 5650-5659, doi:10.1128/AEM.01444-15 (2015).
309 Morgan, C., Rosenkranz, H. S., Carr, H. S. & Rose, H. M. Electron microscopy of chloramphenicol-treated Escherichia coli. *J Bacteriol* **93**, 1987-2002 (1967).
310 Zusman, D. R., Carbonell, A. & Haga, J. Y. Nucleoid condensation and cell division in Escherichia coli MX74T2 ts52 after inhibition of protein synthesis. *J Bacteriol* **115**, 1167-1178 (1973).
311 Hiraga, S., Ogura, T., Niki, H., Ichinose, C. & Mori, H. Positioning of replicated chromosomes in Escherichia coli. *J Bacteriol* **172**, 31-39, doi:10.1128/jb.172.1.31-39.1990 (1990).

312 Donachie, W. D. & Begg, K. J. Chromosome partition in Escherichia coli requires postreplication protein synthesis. *J Bacteriol* **171**, 5405-5409, doi:10.1128/jb.171.10.5405-5409.1989 (1989).
313 Woldringh, C. L., Jensen, P. R. & Westerhoff, H. V. Structure and partitioning of bacterial DNA: determined by a balance of compaction and expansion forces? *FEMS Microbiol Lett* **131**, 235-242, doi:10.1111/j.1574-6968.1995.tb07782.x (1995).
314 Zimmerman, S. B. Shape and compaction of Escherichia coli nucleoids. *J Struct Biol* **156**, 255-261, doi:10.1016/j.jsb.2006.03.022 (2006).
315 Wu, F., Swain, P., Kuijpers, L., Zheng, X., Felter, K., Guurink, M., . . . Dekker, C. Cell Boundary Confinement Sets the Size and Position of the E. coli Chromosome. *Curr Biol* **29**, 2131-2144 e2134, doi:10.1016/j.cub.2019.05.015 (2019).
316 Castellana, M., Hsin-Jung Li, S. & Wingreen, N. S. Spatial organization of bacterial transcription and translation. *Proc Natl Acad Sci U S A* **113**, 9286-9291, doi:10.1073/pnas.1604995113 (2016).
317 Sanamrad, A., Persson, F., Lundius, E. G., Fange, D., Gynna, A. H. & Elf, J. Single-particle tracking reveals that free ribosomal subunits are not excluded from the Escherichia coli nucleoid. *Proc Natl Acad Sci U S A* **111**, 11413-11418, doi:10.1073/pnas.1411558111 (2014).
318 Bakshi, S., Choi, H. & Weisshaar, J. C. The spatial biology of transcription and translation in rapidly growing Escherichia coli. *Front Microbiol* **6**, 636, doi:10.3389/fmicb.2015.00636 (2015).
319 Portier, C., Dondon, L. & Grunberg-Manago, M. Translational autocontrol of the Escherichia coli ribosomal protein S15. *J Mol Biol* **211**, 407-414, doi:10.1016/0022-2836(90)90361-O (1990).
320 Yates, J. L. & Nomura, M. Feedback regulation of ribosomal protein synthesis in E. coli: localization of the mRNA target sites for repressor action of ribosomal protein L1. *Cell* **24**, 243-249, doi:10.1016/0092-8674(81)90520-1 (1981).
321 Kint, C., Verstraeten, N., Hofkens, J., Fauvart, M. & Michiels, J. Bacterial Obg proteins: GTPases at the nexus of protein and DNA synthesis. *Crit Rev Microbiol* **40**, 207-224, doi:10.3109/1040841X.2013.776510 (2014).
322 Watt, R. M., Wang, J., Leong, M., Kung, H. F., Cheah, K. S., Liu, D., . . . Huang, J. D. Visualizing the proteome of Escherichia coli: an efficient and versatile method for labeling chromosomal coding DNA sequences (CDSs) with fluorescent protein genes. *Nucleic Acids Res* **35**, e37, doi:10.1093/nar/gkl1158 (2007).
323 Shcherbakova, D. M., Sengupta, P., Lippincott-Schwartz, J. & Verkhusha, V. V. Photocontrollable fluorescent proteins for superresolution imaging. *Annu Rev Biophys* **43**, 303-329, doi:10.1146/annurev-biophys-051013-022836 (2014).
324 Schnitzbauer, J., Strauss, M. T., Schlichthaerle, T., Schueder, F. & Jungmann, R. Super-resolution microscopy with DNA-PAINT. *Nat Protoc* **12**, 1198-1228, doi:10.1038/nprot.2017.024 (2017).
325 Jungmann, R., Steinhauer, C., Scheible, M., Kuzyk, A., Tinnefeld, P. & Simmel, F. C. Single-molecule kinetics and super-resolution microscopy by fluorescence imaging of transient binding on DNA origami. *Nano Lett* **10**, 4756-4761, doi:10.1021/nl103427w (2010).
326 Sograte-Idrissi, S., Oleksiievets, N., Isbaner, S., Eggert-Martinez, M., Enderlein, J., Tsukanov, R. & Opazo, F. Nanobody Detection of Standard Fluorescent Proteins Enables Multi-Target DNA-PAINT with High Resolution and Minimal Displacement Errors. *Cells* **8**, doi:10.3390/cells8010048 (2019).

327 Schlichthaerle, T., Strauss, M. T., Schueder, F., Auer, A., Nijmeijer, B., Kueblbeck, M., . . . Jungmann, R. Direct Visualization of Single Nuclear Pore Complex Proteins Using Genetically-Encoded Probes for DNA-PAINT. *Angew Chem Int Ed Engl* **58**, 13004-13008, doi:10.1002/anie.201905685 (2019).

328 Cramer, K., Bolender, A. L., Stockmar, I., Jungmann, R., Kasper, R. & Shin, J. Y. Visualization of Bacterial Protein Complexes Labeled with Fluorescent Proteins and Nanobody Binders for STED Microscopy. *Int J Mol Sci* **20**, doi:10.3390/ijms20143376 (2019).

329 Nakashima, N., Goh, S., Good, L. & Tamura, T. Multiple-gene silencing using antisense RNAs in Escherichia coli. *Methods Mol Biol* **815**, 307-319, doi:10.1007/978-1-61779-424-7_23 (2012).

330 Kornprobst, M., Turk, M., Kellner, N., Cheng, J., Flemming, D., Kos-Braun, I., . . . Hurt, E. Architecture of the 90S Pre-ribosome: A Structural View on the Birth of the Eukaryotic Ribosome. *Cell* **166**, 380-393, doi:10.1016/j.cell.2016.06.014 (2016).

331 Kater, L., Thoms, M., Barrio-Garcia, C., Cheng, J., Ismail, S., Ahmed, Y. L., . . . Beckmann, R. Visualizing the Assembly Pathway of Nucleolar Pre-60S Ribosomes. *Cell* **171**, 1599-1610 e1514, doi:10.1016/j.cell.2017.11.039 (2017).

332 Yu, D., Ellis, H. M., Lee, E. C., Jenkins, N. A., Copeland, N. G. & Court, D. L. An efficient recombination system for chromosome engineering in Escherichia coli. *Proc Natl Acad Sci U S A* **97**, 5978-5983, doi:10.1073/pnas.100127597 (2000).

333 Casadaban, M. J. Transposition and fusion of the lac genes to selected promoters in Escherichia coli using bacteriophage lambda and Mu. *J Mol Biol* **104**, 541-555, doi:10.1016/0022-2836(76)90119-4 (1976).

334 Cherepanov, P. P. & Wackernagel, W. Gene disruption in Escherichia coli: TcR and KmR cassettes with the option of Flp-catalyzed excision of the antibiotic-resistance determinant. *Gene* **158**, 9-14, doi:10.1016/0378-1119(95)00193-a (1995).

335 Datsenko, K. A. & Wanner, B. L. One-step inactivation of chromosomal genes in Escherichia coli K-12 using PCR products. *Proc Natl Acad Sci U S A* **97**, 6640-6645, doi:10.1073/pnas.120163297 (2000).

336 Sawitzke, J. A., Thomason, L. C., Costantino, N., Bubunenko, M., Datta, S. & Court, D. L. Recombineering: in vivo genetic engineering in E. coli, S. enterica, and beyond. *Methods Enzymol* **421**, 171-199, doi:10.1016/S0076-6879(06)21015-2 (2007).

337 Sharan, S. K., Thomason, L. C., Kuznetsov, S. G. & Court, D. L. Recombineering: a homologous recombination-based method of genetic engineering. *Nat Protoc* **4**, 206-223, doi:10.1038/nprot.2008.227 (2009).

338 Szczepanska, A. K. Bacteriophage-encoded functions engaged in initiation of homologous recombination events. *Crit Rev Microbiol* **35**, 197-220, doi:10.1080/10408410902983129 (2009).

339 Mosberg, J. A., Lajoie, M. J. & Church, G. M. Lambda red recombineering in Escherichia coli occurs through a fully single-stranded intermediate. *Genetics* **186**, 791-799, doi:10.1534/genetics.110.120782 (2010).

340 Jacob, F., Sussman, R. & Monod, J. [On the nature of the repressor ensuring the immunity of lysogenic bacteria]. *C R Hebd Seances Acad Sci* **254**, 4214-4216 (1962).

341 Zheng, S. Q., Palovcak, E., Armache, J. P., Verba, K. A., Cheng, Y. & Agard, D. A. MotionCor2: anisotropic correction of beam-induced motion for improved cryo-electron microscopy. *Nat Methods* **14**, 331-332, doi:10.1038/nmeth.4193 (2017).

342 Zhang, K. Gctf: Real-time CTF determination and correction. *J Struct Biol* **193**, 1-12, doi:10.1016/j.jsb.2015.11.003 (2016).

343 Kimanius, D., Forsberg, B. O., Scheres, S. H. & Lindahl, E. Accelerated cryo-EM structure determination with parallelisation using GPUs in RELION-2. *Elife* **5**, doi:10.7554/eLife.18722 (2016).
344 Punjani, A., Rubinstein, J. L., Fleet, D. J. & Brubaker, M. A. cryoSPARC: algorithms for rapid unsupervised cryo-EM structure determination. *Nat Methods* **14**, 290-296, doi:10.1038/nmeth.4169 (2017).
345 Grant, T., Rohou, A. & Grigorieff, N. cisTEM, user-friendly software for single-particle image processing. *Elife* **7**, doi:10.7554/eLife.35383 (2018).
346 Zeng, X., Stahlberg, H. & Grigorieff, N. A maximum likelihood approach to two-dimensional crystals. *J Struct Biol* **160**, 362-374, doi:10.1016/j.jsb.2007.09.013 (2007).
347 Dunkle, J. A., Wang, L., Feldman, M. B., Pulk, A., Chen, V. B., Kapral, G. J., . . . Cate, J. H. Structures of the bacterial ribosome in classical and hybrid states of tRNA binding. *Science* **332**, 981-984, doi:10.1126/science.1202692 (2011).
348 Pettersen, E. F., Goddard, T. D., Huang, C. C., Couch, G. S., Greenblatt, D. M., Meng, E. C. & Ferrin, T. E. UCSF Chimera--a visualization system for exploratory research and analysis. *J Comput Chem* **25**, 1605-1612, doi:10.1002/jcc.20084 (2004).
349 Whitford, P. C., Ahmed, A., Yu, Y., Hennelly, S. P., Tama, F., Spahn, C. M., . . . Sanbonmatsu, K. Y. Excited states of ribosome translocation revealed through integrative molecular modeling. *Proc Natl Acad Sci U S A* **108**, 18943-18948, doi:10.1073/pnas.1108363108 (2011).
350 Emsley, P. & Cowtan, K. Coot: model-building tools for molecular graphics. *Acta Crystallogr D Biol Crystallogr* **60**, 2126-2132, doi:10.1107/S0907444904019158 (2004).
351 Gutgsell, N. S. & Jain, C. Gateway role for rRNA precursors in ribosome assembly. *J Bacteriol* **194**, 6875-6882, doi:10.1128/JB.01467-12 (2012).
352 Li, X., Sun, Q., Jiang, C., Yang, K., Hung, L. W., Zhang, J. & Sacchettini, J. C. Structure of Ribosomal Silencing Factor Bound to Mycobacterium tuberculosis Ribosome. *Structure* **23**, 2387, doi:10.1016/j.str.2015.11.002 (2015).
353 Adams, P. D., Afonine, P. V., Bunkoczi, G., Chen, V. B., Davis, I. W., Echols, N., . . . Zwart, P. H. PHENIX: a comprehensive Python-based system for macromolecular structure solution. *Acta Crystallogr D Biol Crystallogr* **66**, 213-221, doi:10.1107/S0907444909052925 (2010).
354 Hager, J., Staker, B. L., Bugl, H. & Jakob, U. Active site in RrmJ, a heat shock-induced methyltransferase. *J Biol Chem* **277**, 41978-41986, doi:10.1074/jbc.M205423200 (2002).
355 Dewachter, L., Verstraeten, N., Jennes, M., Verbeelen, T., Biboy, J., Monteyne, D., . . . Michiels, J. A Mutant Isoform of ObgE Causes Cell Death by Interfering with Cell Division. *Front Microbiol* **8**, 1193, doi:10.3389/fmicb.2017.01193 (2017).

9. Appendix

Table A1: Overview of precursor particles accumulating in assembly factor mutant or depletion strains

Factor	Organism	Mutation/Depletion	Precursors	Ref
DbpA	*E. coli*	overexpression of active site mutant R331A	• **45S** particles of heterogenous composition • reduced levels of uL16, bL25, bL27, bL28, bL33, bL34 and bL35	164
EngA	*E. coli*	conditional depletion	• **50S** particles • reduced levels of bL9 and uL18 • dissociates into **40S** particle under low Mg^{2+} conditions	226
EngB	*B. subtilis*	conditional depletion	• **44.5S**, lacking proteins uL16, bL27 and bL36	162
ObgE	*E. coli*	G80E D85N	• accumulation of **50S** particles • reduced levels of uL16, bL33 and bL34 • dissociates into **40S** particle under low Mg^{2+} conditions	207
		temperature-sensitive mutant (S314P point mutation in G5 motif)	• accumulation of **50S** particles at 42 °C • reduced levels of S1, S14, S21 and L10	208
RlmE		knockout (Δ*rlmE*::$Cm^{r)}$	• accumulation of **50S** particles • dissociates into **45S** particle under low Mg^{2+} conditions • reduced levels of uL5,u L6, uL16, bL18, bL19, bL25, uL2, bL35 and bL36 • reduced levels of uL5, uL16, uL18, bL25, bL27, bL28, uL30, bL33, and bL35	157,354 157 354

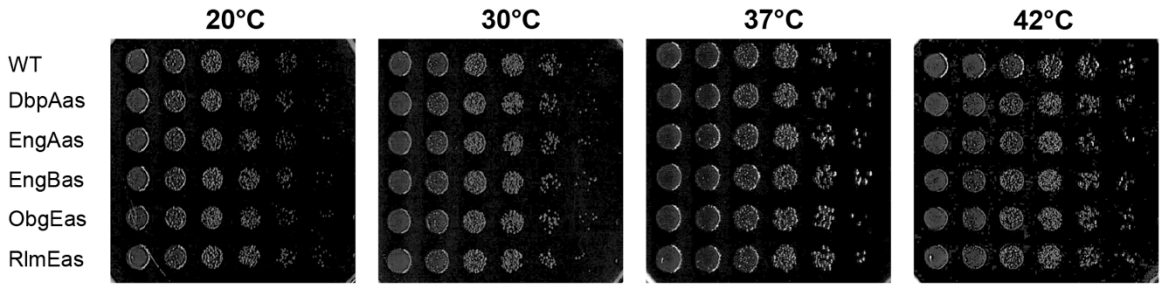

Figure A1: Growth comparison on solid medium. Cells of the wild-type strain MG1655 and the strains harboring the respective assembly factor-specific PTasRNA encoding plasmid (backbone pHN1009) were spotted onto LB agar plates in the absence of IPTG in a serial dilution and incubated at the given temperatures.

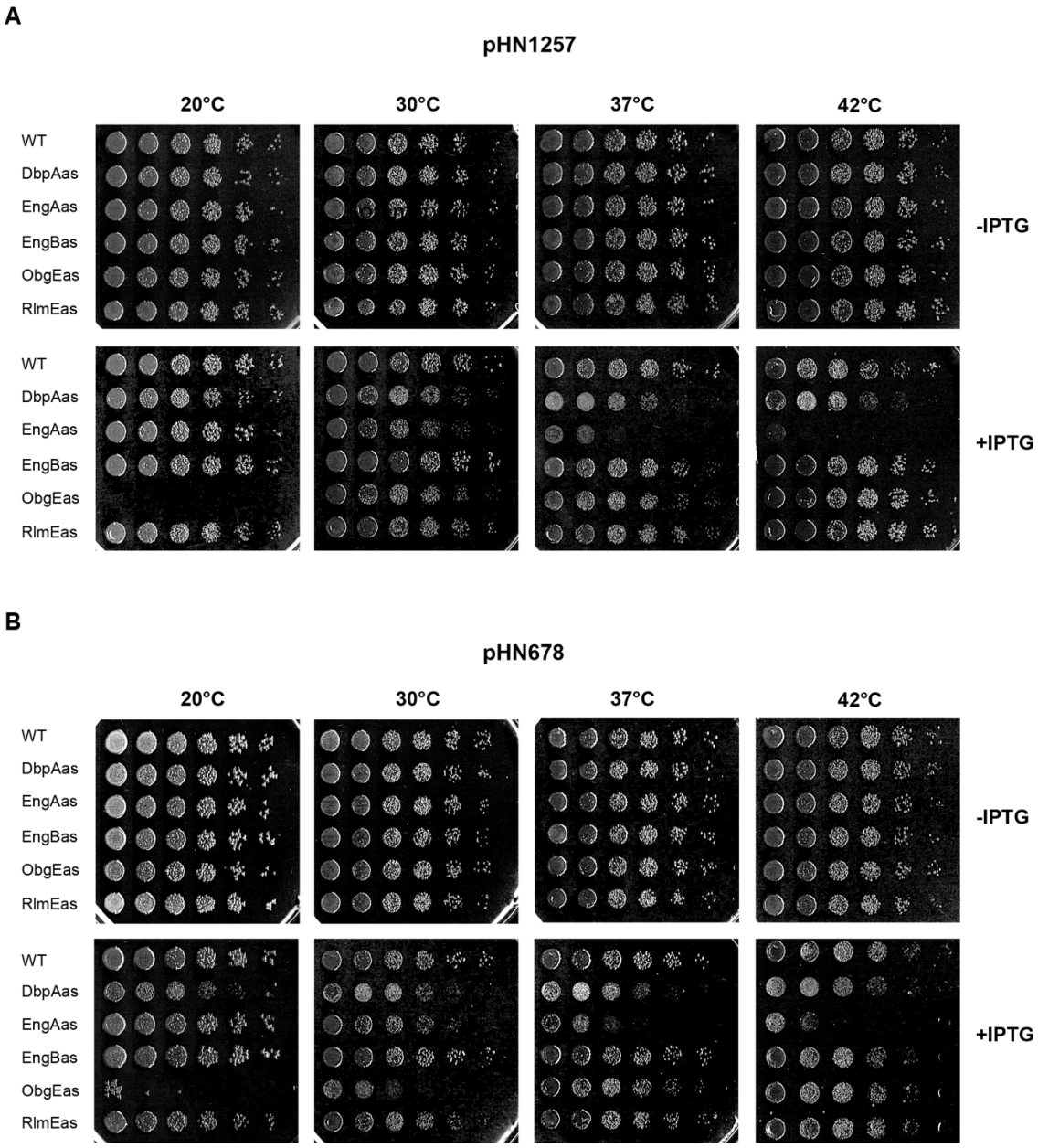

Figure A2: Growth comparison on solid medium. Cells of the wild-type strain MG1655 and the strains harboring the respective assembly factor-specific PTasRNA encoding plasmid backbones **A)** pHN1257 or **B)** pHN678 were spotted onto LB agar plates in the absence or presence of IPTG in a serial dilution and incubated at the given temperatures.

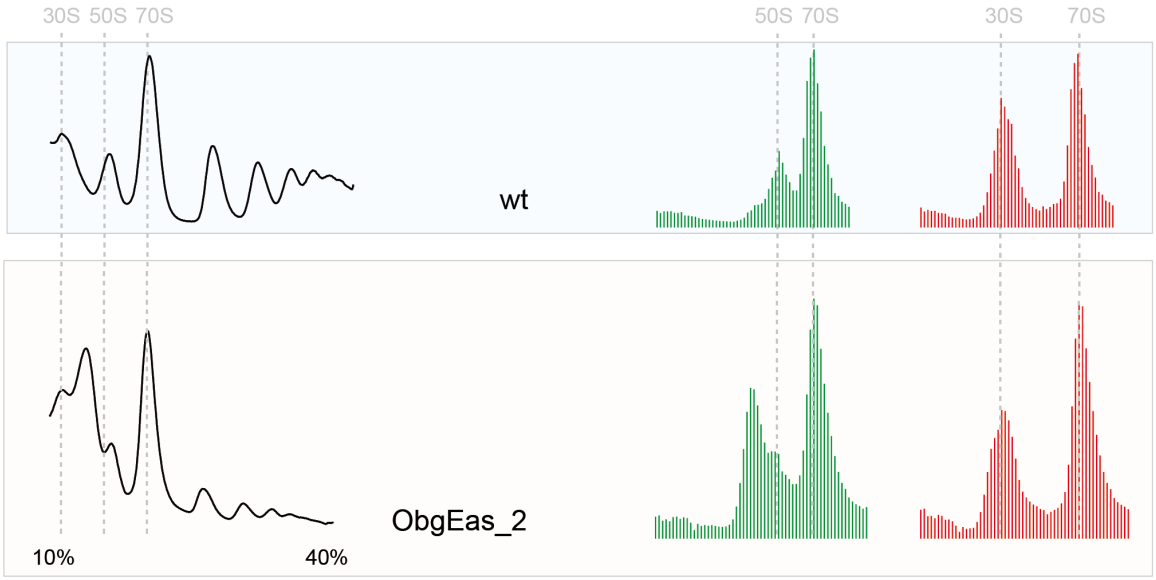

Figure A3: Sucrose density gradient (10-40 %) centrifugation profiles from cells derived from MGrg* or MGrg* depleted for ObgE. ObgE-specific PTasRNA as described by Verstraeten et al.[285,355] was used (ObgEas_2). Cells were cultured in LB medium at 25 °C in the presence or absence of IPTG until they reached an OD~ 0.5. Cleared lysates were subjected to sucrose gradient centrifugation and analyzed via A_{254} detection and fractionated. Sucrose gradient fractions were analyzed for mAzami- and mCherry-specific fluorescence. The fluorescence intensities were normalized to the 70S peak and are depicted in bar charts. Red bars represent mCherry-specific fluorescence; green bars represent mAzami-specific fluorescence. Dashed lines indicate the sedimentation behavior of mature 30S and 50S subunits and 70S ribosomes.

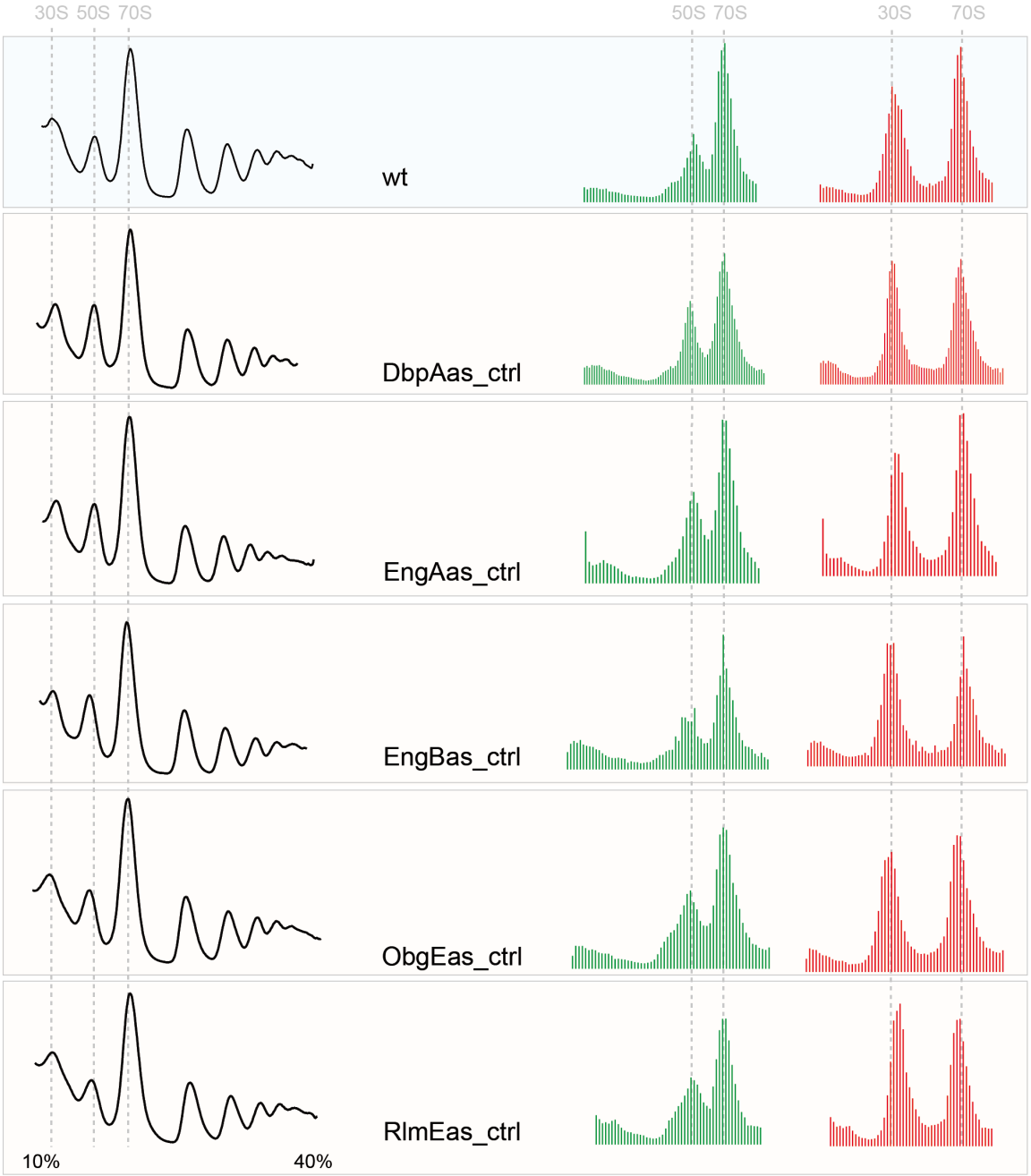

Figure A4: Sucrose density gradient (10-40 %) centrifugation profiles from cells derived from MGrg* or MGrg* harboring PTasRNA against the assembly factors indicated. Cells were cultured in LB medium at 25 °C in the absence of IPTG until they reached an OD~ 0.5. Cleared lysates were subjected to sucrose gradient centrifugation and analyzed via A_{254} detection and fractionated. Sucrose gradient fractions were analyzed for mAzami- and mCherry-specific fluorescence. The fluorescence intensities were normalized to the 70S peak and are depicted in bar charts. Red bars represent mCherry-specific fluorescence;

green bars represent mAzami-specific fluorescence. Dashed lines indicate the sedimentation behavior of mature 30S and 50S subunits and 70S ribosomes. Ctrl = control.

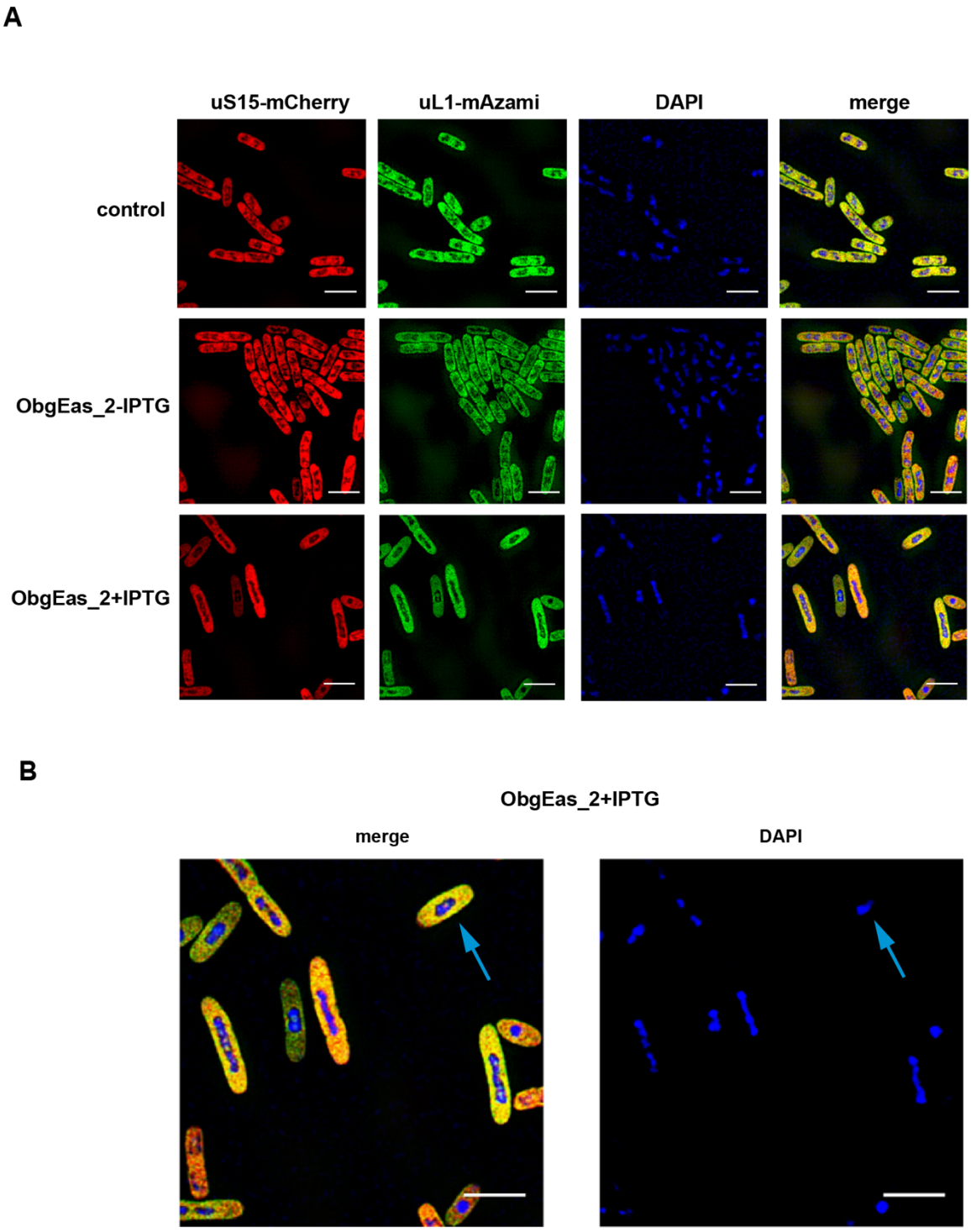

Figure A5: Figure 23: ObgE depletion upon expression of ObgE-specific PTasRNA construct ObgEas_2. A) Fluorescence microscopic images of *E. coli* strain MGrg* harboring

ObgE-specific PTasRNA expressing plasmids were cultured in the presence or absence of IPTG and were compared to the unperturbed strain MGrg*. Cells were grown at 37 °C in LB medium and PTasRNA expression against ObgE was induced at OD_{600} = 0.15 with 1mM IPTG. Cells were harvested at OD_{600} = 0.5, fixed and DNA was stained with DAPI for subsequent microscopic analysis by 3D-SIM. Distribution of ribosomal subunits (green: uL1-mAzami-specific fluorescence; red: uS15-mCherry-specific fluorescence) and chromosomal DNA (blue: DAPI staining) is depicted. An overlay was created (merge). Representative images are shown. **B)** Magnification of ObgE depleted cells. Merge and DAPI stain are shown. Arrows highlight foci formation. Scale bar = 3µm.

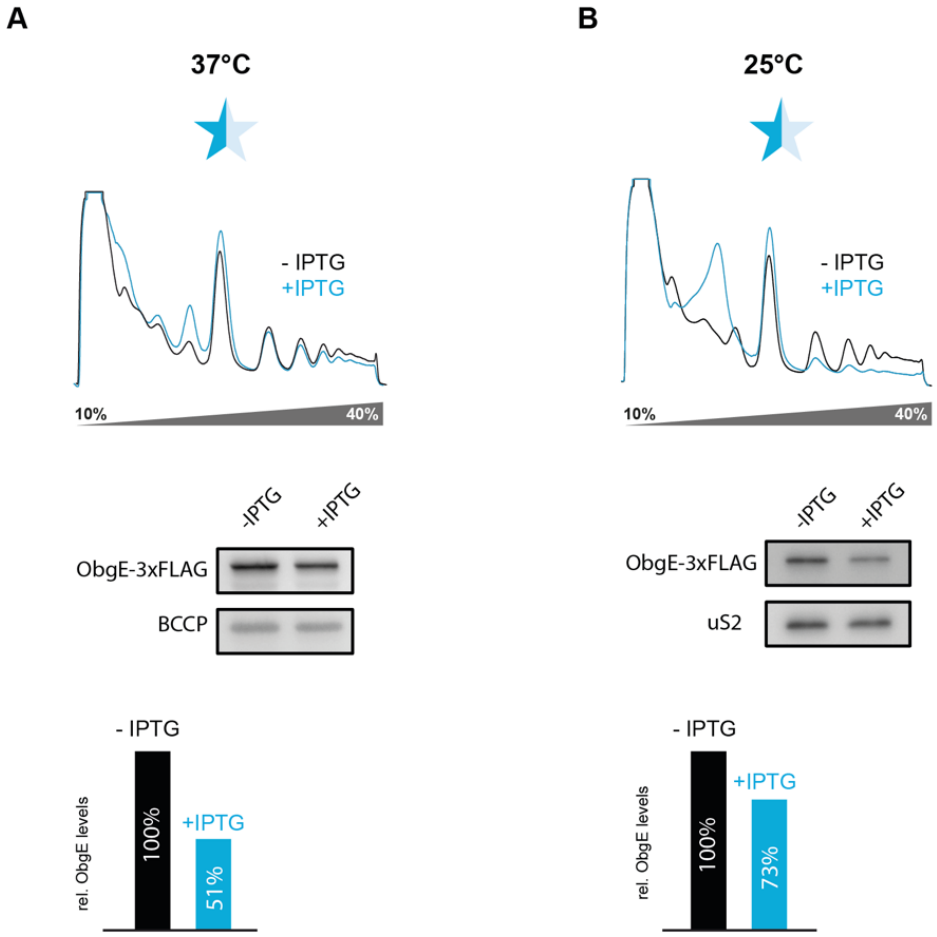

Figure A6: Comparison of knock-down efficacy in ObgE depleted cells at 25 °C and 37 °C. Cells were cultured in LB medium at 25 °C or 37 °C in the presence or absence of IPTG until they reached an OD~ 0.5. IPTG expression was induces at OD_{600}=0.1 for cells cultivated at 25 °C. Cells cultivated at 37 °C were repeatedly diluted in the presence of

IPTG (3x) to the initial OD_{600} to achieve growth perturbation similar to cells cultivated at 25 °C. Cleared lysates were subjected to sucrose gradient centrifugation and analyzed via A_{254} detection. 20 µg of total protein content of lysates were analyzed by immunoblotting and probed with anti-FLAG, anti-uS2 antibody or Strep-Tactin HRP-conjugate. Appropriate loading controls (BCCP or uS2) were used to determine relative ObgE levels.

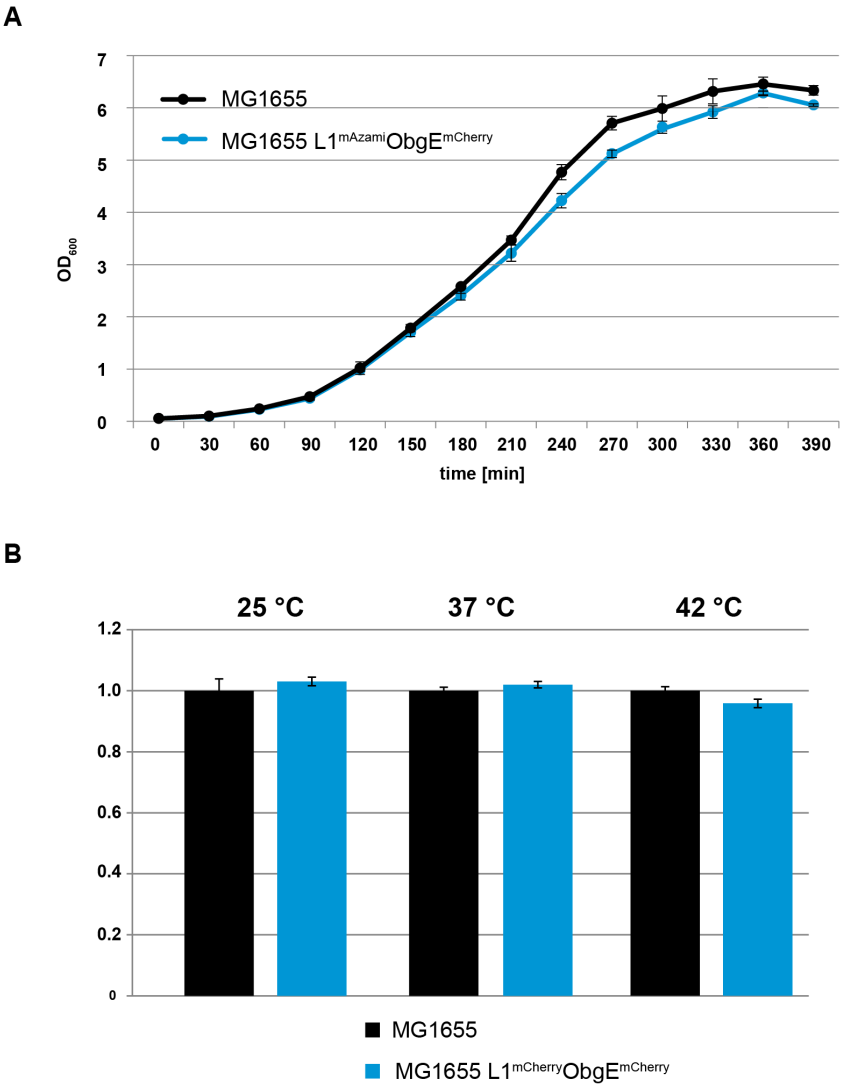

Figure A7: Phenotypic characterization of reporter strain MG1655 uL1^{mAzami}ObgE^{mCherry} expressing fluorescently labeled uL1-mAzami and ObgE-mCherry. (A) Growth curve of MG1655 and MG1655 ObgE^{red}L1^{green}: strains were grown in LB medium at 37 °C and 200 rpm, OD_{600} was determined every 30min, error bars show s.d. (n=3); (B) Growth rate of

strain MG1655 ObgE^{red}L1^{green} was calculated and normalized to wild-type strain MG1655 at 25 °C, 37 °C and 42 °C, error bars show s.d. (n=3);

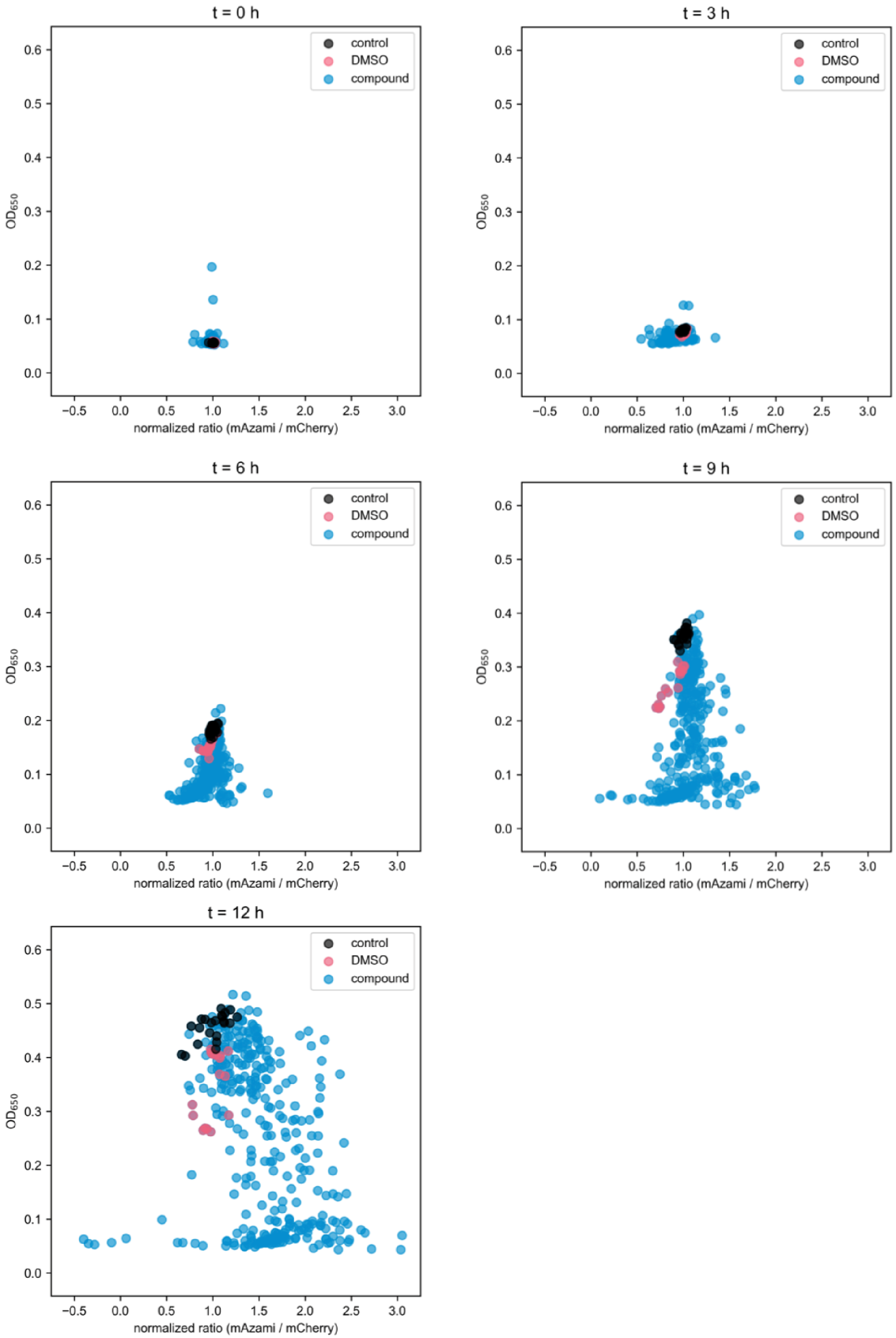

Figure A8: Scatter plots depicting the OD_{600} and normalized ratio mAzami/mCherry of

reporter strain MGrg* in the absence or presence of 10 µM compounds or DMSO at timepoints t=2, 3, 6, 9 and 12. Cells of the reporter strain MGrg* or MG1655 were cultured in 384-multiwell plates at 30 °C in the absence or presence of 10 µM compounds or DMSO for 12 hours. Hourly, A_{650} and mCherry- and mAzami-specific fluorescence intensities were determined. Ratios cells were normalized to the mean value of the untreated reporter cells.

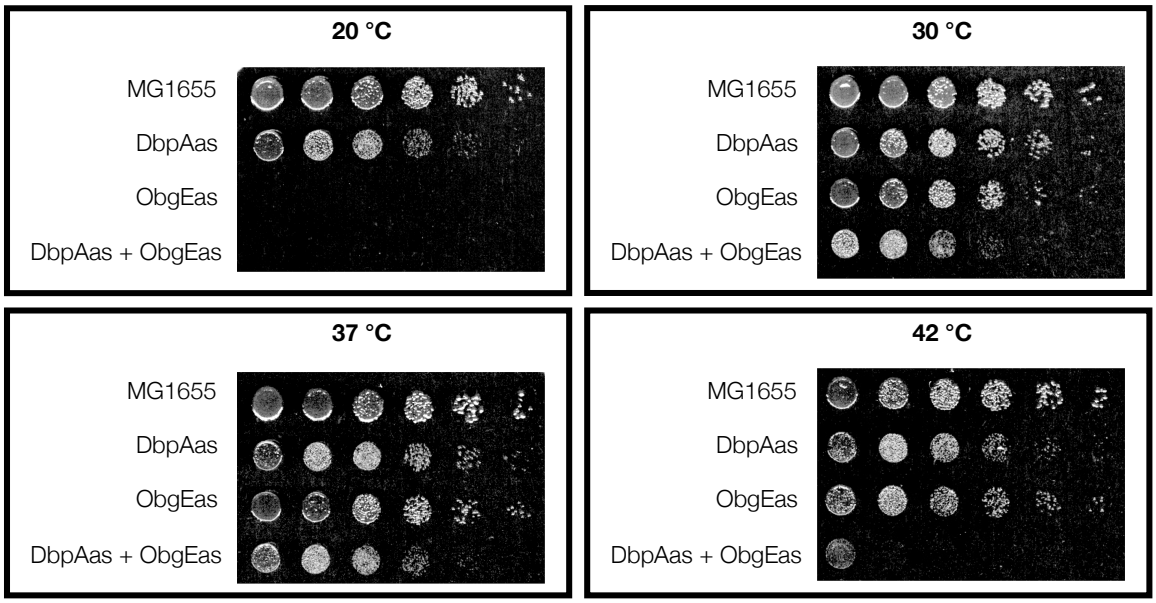

Figure A9: Growth comparison on solid medium. Cells of the wild-type strain MG1655 and the strains harboring the respective assembly factor-specific PTasRNA-expressing plasmids (pHN1257-ObgEas and/or pHN1009-DbpAas) were spotted onto LB agar plates in the absence of IPTG in a serial dilution and incubated at the given temperature.

10. Acknowledgements

Hiermit möchte ich mich herzlichst bei Prof. Dr. Elke Deuerling bedanken. Ich danke Dir für die lehrreiche Vorlesung während des Studiums, die mich auf das spannende Feld der Mikrobiologie aufmerksam machte. Vielen Dank für die Zuteilung eines solch vielfältigen, umfassenden und interessanten Forschungsprojektes, das ich seit meiner Bachelorarbeit begleiten und mitgestalten durfte.

Vor allem die Zeit während der Promotion hat mich sehr geprägt und mir geholfen, mich weiterzuentwickeln. Ich bin dankbar für die Möglichkeit, meine Arbeit auf internationalen Konferenzen vorstellen und diskutieren zu dürfen. So hatte ich die beste Grundlage, dieses Projekt mit neuen Anreizen weiterzuführen. Vielen Dank für die kontinuierliche Unterstützung, die zahlreichen Diskussionen und das Vertrauen.

Ein besonderer Dank gilt auch Dr. Rainer Nikolay für seine Unterstützung über all die Jahre. Ich danke Dir für die ausgezeichnete Betreuung, sowohl vor Ort als auch über die Distanz Konstanz-Berlin. Einen besseren Betreuer hätte ich mir ehrlich nicht vorstellen können. Vielen Dank, dass Du mir das komplexe Feld der Ribosomenbiogenese nähergebracht und mich in meiner Arbeit und der Wissenschaft immer unterstützt hast. Durch die zahlreichen Gespräche und Diskussionen habe ich viel von Dir gelernt und ich bin sehr dankbar, dass Du Deine Erfahrung auf diese Weise weitergibst.

Liebe Pari, ich danke Dir sehr für die Unterstützung. Egal worum es ging, Deine Tür war immer offen.

Weiterhin bedanke ich mich bei meinen jetzigen und ehemaligen Laborkollegen und -kolleginnen Nadine, Sina, Anne, Sandra, Karina, Annalena, Karthik, Stefan und Christina. Vielen Dank für die gegenseitige Hilfe und die tolle Zeit in der Arbeitsgruppe. Sina, Du warst seit Beginn der Bachelorarbeit eine große Unterstützung und ich konnte mit jedweder Frage und jedem Problem immer zu Dir kommen. Ohne Dich wäre die Zeit im Labor und fernab nicht halb so schön gewesen. Nadine, Karina und Lena, auch Euch danke ich

von Herzen für die mentale Unterstützung, die gemeinsamen Kaffeepausen und dafür, dass Ihr immer ein offenes Ohr hattet. Christina, mit Dir war die Zeit auf der Ribosomenkonferenz in Mexiko und anschließend in Havanna unvergesslich. Karthik, thank you for challenging my English and the numerous discussions (especially about the newest shows and movies).

Vielen Dank an alle Studenten, die ich über die Jahre betreuen durfte und die mein Projekt vorangebracht haben. Vor allem möchte ich mich bei Dana, Klara und Carla bedanken.

Liebe Renate, ich danke Dir für die Unterstützung im Labor, vom Anfang bis heute. Danke für die zahlreichen Ratschläge, Protokolle, Rezepte und dein Engagement. Auch Uli und Gundula möchte ich dafür danken, dass Ihr die Ordnung im „Doktoranden-Chaos" wahrt. Ina, lieben Dank für die Zeit mit Dir am Mikroskop und beim Mittagessen, die tollen Kuchen und Deine Unterstützung.

Vielen Dank an alle Mitglieder der Arbeitsgruppe.

Ein großer Dank gilt weiterhin allen Kooperationspartnern, die bei diesem und anderen Projekten mitgewirkt haben. Besonders möchte ich mich bei Silke Müller (Screening Center), Dr. Martin Stöckl (Bioimaging Center), Prof. Dr. Knud Nierhaus und Prof. Dr. Christian Spahn bedanken.

Des Weiteren bedanke ich mich bei allen Gutachtern und dem Prüfungsvorsitz meiner Arbeit für die Mühe: Prof. Dr. Elke Deuerling, Prof. Dr. Jörg Hartig und Prof. Dr. Aswin Mangerich.

Bei der Universität Konstanz und der Konstanz Research School Chemical Biology (KoRS-CB) bedanke ich mich für das Weiterbildungsangebot.

Allen meinen Freunden danke ich für Ihre Unterstützung und für die unvergessliche Zeit in Konstanz. Es war nicht immer einfach, aber einfach wäre wohl auch langweilig. Danke besonders an Moritz, Leonie, Flo, Sunny, Björn und Sophie. Flo, deine Programmier-Kenntnisse waren wirklich Rettung in letzter Sekunde!

Acknowledgements

Von ganzem Herzen danke ich meiner Familie. Danke Mami, Tata, Omi, Herbert, Boby, Schlawina und Paulchen (und den ~200 etwas anderen Mitgliedern). Ich danke Euch für Eure Unterstützung auf allen Ebenen. Ihr habt mich immer bestärkt und an mich geglaubt. Ohne Euch wäre Vieles nicht möglich gewesen. Herzlichen Dank!